Summer 2015

Passive mass transport for direct and quantitative SERS detection using purified silica encapsulated metal nanoparticles

Binaya Kumar Shrestha
University of Iowa

PASSIVE MASS TRANSPORT FOR DIRECT AND QUANTITATIVE SERS DETECTION USING PURIFIED SILICA ENCAPSULATED METAL NANOPARTICLES

by

Binaya Kumar Shrestha

A thesis submitted in partial fulfillment
of the requirements for the Doctor of
Philosophy degree in Chemistry
in the Graduate College of
The University of Iowa

August 2015

Thesis Supervisor: Associate Professor Amanda J. Haes

Graduate College
The University of Iowa
Iowa City, Iowa

CERTIFICATE OF APPROVAL

PH.D. THESIS

This is to certify that the Ph.D. thesis of

Binaya Kumar Shrestha

has been approved by the Examining Committee for the thesis requirement for the Doctor of Philosophy degree in Chemistry at the August 2015 graduation.

Thesis Committee:

Amanda J. Haes, Thesis Supervisor

Ned Bowden

Edward Gillan

Vicki Grassian

Aliasger Salem

To my family, friends, and colleagues who supported and helped me throughout my life and career.

ACKNOWLEDGMENTS

First, I would like to sincerely thank my advisor, Professor Amanda J. Haes, for all her support and dedication provided to me all these years during my graduate carrier. You are an excellent mentor and educator; and I have learned so much about nanoscience under your supervision.

Next, I would like to thank my family members, my parents, and friends for believing in me and motivating me to achieve this degree. You have always supported me in various aspect of my life and I would not be here without you. I would also like to thank all of Haes group members, both former and present for all their support.

Finally, I would like to express my sincere gratitude to my loving wife, Irshu Shrestha, who has always been there for me at every corner of my life. Without you and your motivation, I would not have been successful realizing my goals towards this degree.

Thank you all for being part of this journey that I would always cherish in my life.

ABSTRACT

This thesis focuses on understanding implications of nanomaterial quality control and mass transport through internally etched silica coated nanoparticles for direct and quantitative molecular detection using surface enhanced Raman scattering (SERS). Prior to use, bare nanoparticles (partially or uncoated with silica) are removal using column chromatography to improve the quality of these nanomaterials and their SERS reproducibility. Separation of silica coated nanoparticles with two different diameters is achieved using Surfactant-free size exclusion chromatography with modest fractionation. Next, selective molecular transport is modeled and monitored using SERS and evaluated as a function of solution ionic strength, pH, and polarity. Molecular detection is achieved when the analytes first partition through the silica membrane then interact with the metal surface at short distances (i.e., less than 2 nm). The SERS intensities of unique molecular vibrational modes for a given molecule increases as the number of molecules that bind to the metal surface increases and are enhanced via both chemical and electromagnetic enhancement mechanisms as long as the vibrational mode has a component of polarizability tensor along the surface normal. SERS signals increase linearly with molecular concentration until the three-dimensional SERS-active volume is saturated with molecules. Implications of molecular orientation as well as surface selection rules on SERS intensities of molecular vibrational modes are studied to improve quantitative and reproducible SERS detection using internally etched $Ag@Au@SiO_2$ nanoparticles. Using the unique vibrational modes, SERS intensities for p-aminothiophenol as a function of metal core compositions and plasmonics are studied. By understanding molecular transport mechanisms through internally etched silica

matrices coated on metal nanoparticles, important experimental and materials design parameters are learned, which can be subsequently applied to the direct and quantifiable detection of small molecules in real samples without the need for lengthy separations and assays.

PUBLIC ABSTRACT

This thesis focuses on understanding implications of nanomaterial properties and molecular transport through internally etched silica coated nanoparticles for direct and quantitative molecular detection using surface enhanced Raman scattering (SERS). Noble metal nanoparticles (gold, silver, and copper) exhibit unique size-dependent chemical and physical properties that warrant their application in molecular detection, biological imaging, sensors, and optical filters. Because small changes in nanoparticle size, shape, or environment have huge effect on their properties; prior to use, removal of defect nanoparticles through fractionation using column chromatography is important to improve the reproducibility of their function. Purified silica coated nanoparticles are internally etched to increase silica pore size so that molecules in the solution can diffuse to the metal surface for detection. Molecular transport though porous silica is studied using SERS and evaluated as a function of solution ionic strength, pH, and polarity. SERS detection is shown to depend on silica morphology, molecule concentration, nanoparticle concentration, and molecular orientation on nanoparticle surfaces. Understanding their implication on SERS is important to obtain experimental and material design parameters necessary for direct, quantifiable, reproducible detection of small molecules in environmental or biological samples without the need of state-of-the art instrumentation.

TABLE OF CONTENTS

LIST OF TABLES x

LIST OF FIGURES xi

CHAPTER 1 AN OVERVIEW OF EXISTING SERS SUBSTRATES, APPLICATIONS, LIMITATIONS, AND CURRENT APPROACHES FOR OVERCOMING CHALLENGES ASSOCIATED WITH SOLUTION-PHASE SERS SUBSTRATES 1
1.1 Introduction 1
1.2 Raman Spectroscopy 3
1.3 SERS and Molecular Detection 4
1.4 SERS Substrates and Applications 6
1.5 Advantages and Limitations of Solution-Phase SERS Substrates 10
1.6 Thesis Overview 13

CHAPTER 2 IMPROVING QUALITY CONTROL OF SILICA COATED GOLD NANOSPHERES USING POST-SYNTHETIC COLUMN PURIFICATION 22
2.1 Introduction 22
2.2 Experimental Materials and Methods 24
2.2.1 Chemical Reagents 24
2.2.2 Gold Nanoparticle and Silica Coated Au Nanoparticle Synthesis 25
2.2.3 Silica-Coated Au Nanoparticles Fractionation Using Size Exclusion Chromatography 25
2.2.4 Extinction Spectroscopy 26
2.2.5 Transmission Electron Microscopy (TEM) 26
2.3 Results and Discussion 27
2.3.1 Silica Coated Au Nanoparticle Size Heterogeneity 27
2.3.2 SEC Maintains Nanoparticle Optical and Morphological Stability 30
2.3.3 LSPR Wavelength Maximum as a Function of Silica Thickness and Plasmon Coupling 31
2.3.4 SEC Separation of Silica Coated Nanoparticles 35
2.3.5 Conclusion 41

CHAPTER 3 IMPLICATIONS OF SOLUTION IONIC STRENGTH, PH, AND POLARITY IN THE PASSIVE TRANSPORT OF SMALL ANALYTES THROUGH SILICA MEMBRANE STABILIZED GOLD COATED SILVER NANOPARTICLES 45
3.1 Introduction 45
3.2 Experimental Materials and Methods 47
3.2.1 Chemical Reagents 47
3.2.2 Silver@Gold Nanoparticle Synthesis 48
3.2.3 Microporous Silica-Coated Ag@Au Nanoparticles Synthesis 49
3.2.4 Internally Etched Silica-Coated Silver@Gold Nanoparticle Synthesis 49

3.2.5 Extinction and SERS Spectroscopies 50
3.2.6 Transmission Electron Microscopy (TEM) 50
3.2.7 SERS Sample Preparation 50
3.3 Results and Discussion..... 51
3.3.1 Determination of SERS rate constants as a function of ionic strength..... 55
3.3.2 Determination of SERS rate constants as a function of pH..... 61
3.3.3 Determination of SERS rate constants as a function of polarity ... 66
3.3.5 Conclusion 70

CHAPTER 4 QUANTITATIVE AND REPRODUCIBLE SERS DETECTION USING SILICA MEMBRANE DENSITY CONTROL ON GOLD COATED SILVER NANOPARTICLES..... 74
4.1 Introduction..... 74
4.2 Experimental Materials and Methods 76
4.2.1 Chemical Reagents 76
4.2.2 Silver@Gold Nanoparticle Synthesis 77
4.2.3 Microporous Silica-Coated Ag@Au Nanoparticles Synthesis 77
4.2.4 Internally Etched Silica-Coated Silver@Gold Nanoparticle Synthesis 78
4.2.5 Extinction and SERS Spectroscopies 78
4.2.6 Transmission Electron Microscopy (TEM) 79
4.3 Results and Discussion..... 80
4.3.1 Evaluating the Optical and Dielectric Properties of Ag@Au and Ag@Au@SiO_2 Nanoparticles..... 80
4.3.2 SERS Signals as a Function of Effective Refractive Index 87
4.3.3 SERS Signal Dependencies on Molecular Concentrations..... 89
4.3.4 SERS Signal Dependencies on Nanoparticle Concentrations 92
4.3.5 Conclusion 93

CHAPTER 5 ADSORPTION OF THIOLATED MOLECULES ON INTERNALLY ETCHED AG@AU NANOPARTICLES USING LSPR AND SERS..... 98
5.1 Introduction..... 98
5.2 Materials and Methods..... 100
5.2.1 Chemical Reagents. 100
5.2.2 Nanoparticle Synthesis. 101
5.2.3 Transmission Electron Microscopy. 102
5.2.4 Extinction and SERS Spectroscopies. 103
5.3 Results and Discussion..... 104
5.3.1 Layer Thickness and Molecular Orientation. 104
5.3.2 Molecular Adsorbate, Concentration, and Vibrational Mode Dependence..... 108
5.3.3 Adsorption Isotherm Analysis. 117
5.4 Conclusion 120

CHAPTER 6 IMPLICATIONS OF NANOPARTICLE CONCENTRATION, MORPHOLOGY, AND PLASMONIC PROPERTIES ON SERS INTENSITIES USING SILICA MEMBRANE STABILIZED COMPOSITE NANOPARTICLES 126
6.1 Introduction..... 126
6.2 Experimental Materials and Methods 127
6.2.1 Chemical Reagents 127
6.2.2 Gold and Silver@Gold Nanoparticle Synthesis 128

6.2.3 Microporous Silica-Coated Au and Ag@Au Nanoparticles Synthesis 129
6.2.4 Internally Etched Silica-Coated Nanoparticle Synthesis 130
6.2.5 Extinction and SERS Spectroscopies 131
6.2.6 Transmission Electron Microscopy (TEM) 131
6.3 Results and Discussion 132
6.3.1 LSPR Tuning of Silica Coated Nanoparticles 132
6.3.2 Implication of Nanoparticle Core Composition on SERS 134
6.3.3 Nanoparticle Concentration and Extinction at Raman Excitation Wavelength Implication on SERS 138
6.3.4 Charge Transfer Resonance Implication on p-Aminothiophenol SERS 145
6.3.5 Conclusion 149

CHAPTER 7 CONCLUSION AND FUTURE DIRECTIONS 155
7.1 Conclusion 155
7.2 Future Directions 157

LIST OF TABLES

Table 2.1. Elution volumes and peak tailing factors for a mixture of $Au@SiO_2$ nanoparticle samples through SEC. 39

Table 3.1. SERS rate constants (min^{-1}) for various solution conditions. 69

Table 5.1. Summary of SAM thicknesses and molecular tilt angles from LSPR analysis. 106

Table 5.2. Vibrational frequency assignments for possible species present in these samples. 111

Table 5.3. Langmuir adsorption isotherm results for CS stretching mode from the SERS data. 117

Table 5.4. Langmuir adsorption isotherm results from the SERS data. 119

Table 6.1. Concentration, extinction @ Raman λ_{ex}, and SERS intensities for CS stretching mode of p-aminothiophenol on IE $Ag@Au@SiO_2$ nanoparticles with 3 different Ag@Au core diameters. 143

Table 6.2. Frequencies (cm^{-1}) and relative SERS intensities of b_2 vibrational modes for p-aminothiophenol on IE $Ag@Au@SiO_2$ nanoparticles. 148

LIST OF FIGURES

Figure 1.1. Scheme of common SERS enhancement mechanisms. (A) Ground state chemical enhancement as a result of chemical interactions between molecule and nanoparticle, (B) resonance Raman resulting from excitation energy resonance with molecular transition, (C) charge-transfer resonance Raman effect as a result of excitation energy in resonance with nanoparticle-molecule charge transfer transitions, and (D) plasmon resonance enhancement that arises from the strong local electromagnetic field when the excitation energy is in resonance with the nanoparticle plasmon. 5

Figure 1.2. Representative TEM images of bottom-up synthesized nanoparticles with different compositions, shapes and sizes. (A) Au nanospheres (diameter (d) = 12.3 ± 1.1 nm), (B) 33.4 nm Au nanospheres (d = 33.4 ± 3.0 nm), (C) Ag@Au core-shell nanospheres (d = 14.5 ± 2.9 nm), and (D) Au nanorods (length = 45.4 ± 7.7 nm, width = 16.2 ± 3.2 nm). 9

Figure 1.3. Time dependent LSPR (black) and SERS (red) signals for 4 nM gold nanospheres incubated with 10 µM 4-aminothiophenol. Both the extinction monitored at 785 nm and SERS intensity at 1079 cm^{-1} show that the spectroscopic signals initially increase then decrease over time as a result of variations in nanoparticle plasmonics. 12

Figure 2.1. TEM images of gold (A) and silica coated gold nanoparticles synthesized using 0.60 mM (B) and 0.90 mM (C) sodium silicate during silica growth. The mean diameter of synthesized nanoparticles are (A) 12.7 ± 1.3 nm (10% RSD, N = 355), (B) 20.1 ± 2.1 nm (10% RSD, N = 118, and (C) 39.7 ± 3.9 nm (10% RSD, N = 430). Diameter distribution of (D) Au nanoparticles and (E) 39.7 nm Au@SiO_2 nanoparticles show broad distribution curves. 99.7% of Au and Au@SiO_2 nanoparticles range from 10 – 15 nm (± 3σ) and 30 – 50 nm (± 3σ) and confirm the hypothesis that bottom-up synthesis of solution-phase nanoparticles generates heterogeneous nanoparticle distribution. 28

Figure 2.2. Extinction and TEM analysis of Au@SiO_2 nanoparticles during SEC purification. (A) LSPR of Au@SiO_2 nanoparticles before and after purification. λ_{max} and Γ of sample before SEC are 525.0 nm and 0.38 eV. Similarly, λ_{max} and Γ of sample collected after SEC are 524.8 nm and 0.38 eV respectively indicating that no significant changes in optical property occurs during SEC. Representative TEM analysis of Au@SiO_2 nanoparticles before (B) and after (C) indicate no change is shape and size morphologies. Mean diameter calculated from TEM images are (B) 39.7 ± 3.9 nm and (C) 40.6 ± 4.4 nm. No statistical difference between mean diameters is verified using t-test at 95% confidence level. Au@SiO_2 nanoparticle fractions are pooled together to collect LSPR and TEM images. 30

Figure 2.3. (A) Theoretical plot of $\lambda_{max,silica}$ *vs.* silica thickness during SEC using 10% isopropanol as bulk (RI 1.34). $\lambda_{max,silica}$ red shifts as silica shell

thickness increases. For silica thickness <8 nm, significant decrease in $\lambda_{max,silica}$ as a function of decreasing silica thickness is observed. Beyond 8 nm silica thickness, $\lambda_{max,silica}$ values saturate at 525.9 nm. (B) Theoretical plot of LSPR wavelength shift as a function of nanoparticle plasmon coupling for ~12 nm Au nanoparticles. As gap distances between two 12 nm Au nanoparticles decreases below 9 nm, LSPR red shift of >1 nm is expected which increases sharply for gap distances <5 nm. (C) Expected $\lambda_{max, Coupled}$ as a function of silica shell thickness plotting for two Au@SiO_2 nanoparticles touching edge-edge through silica. Plot shows that as silica thickness increases, LSPR shift of coupled nanoparticle decreases exponentially and stabilizes above 6 nm. Inset shows TEM image of 23.4 ± 2.6 nm (11% RSD) Au@SiO2 nanoparticles with silica defects (partially or uncoated) shown with black arrows. 34

Figure 2.4. SEC separation of two Au@SiO_2 nanoparticle samples that differ in particle diameter. As Au@SiO_2 nanoparticles mixture pass though Sephacryl S-1000 column, nanoparticle separate based on size. Using in-line LSPR detection, Au@SiO_2 nanoparticle elution through SEC column is monitored. 36

Figure 2.5. (A) SEC chromatogram of a mixture of Au@SiO_2 nanoparticles with average diameters (1) 54.4 ± 5.8 (10 %RSD) and (2) 27.0 ± 4.6 (11 %RSD). Nanoparticle samples elute at 8.9 and 10.6 mL elution volume. (B) LSPR λ_{max} analysis of eluted Au@SiO_2 nanoparticle mixture. λ_{max} remain stable at ~526.8 nm for 54.4 nm Au@SiO_2 nanoparticles. As smaller nanoparticles elute, λ_{max} increases to 528.5 nm and decreases as higher elution volumes. (C and D) LSPR spectra and TEM images of fractions collected at (1) 8.6, (2) 10.3, (3) 10.7, and (4)11.6 mL. TEM images shows the two samples are separated through SEC column. Au@SiO_2 nanoparticle sample eluted 8.6 mL does not contain smaller particles. Samples eluted at 10.3 mL show presence of both Au@SiO_2 nanoparticles. 38

Figure 3.1. (A) TEM image of IE Ag@Au@SiO_2 nanoparticles. Ag@Au core and IE Ag@Au@SiO_2 nanoparticle average diameters are 26.0 ± 5.4 nm and 76.9 ± 7.7 nm. (B) LSPR analysis of IE Ag@Au@SiO_2 nanoparticles before and after addition of 4-aminothiophenol. After addition of 4-aminothiophenol molecules, LSPR λ_{max} red shifts from (1) 538.9 nm to (2) 543.8 nm as the local refractive index around nanoparticle core increases from molecules occupying SERS-active volume near metal core. (C) SERS spectra of 10 µM (1) 2-naphthalenethiol, (2) benzenethiol, (3) 4-mercaptobenzoic acid, and (4) p-aminothiophenol in 100 mM ionic strength and pH 6.5 phosphate buffer after 15 minutes of incubation time. Spectra show ring stretching mode at 1622, 1575, 1585, and 1594 cm^{-1}; and CS stretch contributions at 1067, 1074, 1078, and 1079 cm^{-1}; respectively for 2-naphthalenethiol, benzenethiol, 4-mercaptobenzoic acid, and p-aminothiophenol. In addition, 2-naphthalenethiol show strong ring stretching mode at 1380 cm^{-1} whereas benzenethiol shows additional intense peaks at 1021 and 997 cm^{-1} associated with CH bending and out of plane ring deformation. (D) Temporal SERS (1) and normal Raman (2) profile of p-aminothiophenol in 100 mM ionic strength

and pH 6.5 phosphate buffer collected every 10s collected. The fitted curve represents first-order time dependent Langmuir isotherm. 53

Figure 3.2. Saturated SERS spectra plotted for (A) 2-naphthalenethiol, (B) benzenethiol, (C) 4-mercaptobenzoic acid, and (D) p-aminothiophenol at (1) 0, (2) 50, and (3) 100 mM ionic strength and pH 6.5 phosphate buffer after 15 minutes of incubation time. Spectra show ring stretching mode at 1622, 1575, 1585, and 1594 cm^{-1}; and CS stretch contributions at 1067, 1074, 1078, and 1079 cm^{-1}; respectively for 2-naphthalenethiol, benzenethiol, 4-mercaptobenzoic acid, and p-aminothiophenol molecules. SERS parameters: λ_{ex} = 632.8 nm, t_{int} = 10 s, and P = 2 mW. 56

Figure 3.3. Time dependent SERS signals for 10 µM molecular concentration on IE Ag@Au@SiO_2 nanoparticles. Temporal profile of (A) 1067 cm^{-1} (CH bend/CS stretch) mode for 2-naphthalenethiol, (B) 1074 cm^{-1} (CS and CC symmetric stretch) mode for benzenethiol, (C) 1078 cm^{-1} (CC ring/CS stretch) for 4-mercaptobenzoic acid, and (D) 1079 cm^{-1} (CS stretch) for p-aminothiophenol. The curves are: black = 0, red = 10, green = 25, blue = 50, magenta = 75, and dark yellow = 100 mM ionic strength. The ionic strength of the solution is adjusted using 100 mM KCl solution. SERS parameters as in Figure 3.2. 57

Figure 3.4. Rate constants determined for time dependent SERS signals as a function of solution ionic strength. Data points are: black = 2-naphthalenethiol, red = benzenethiol, green = 4-mercaptobenzoic acid, and blue = p-aminothiophenol. Rate constant increases with increasing solution ionic strength for 2-napthalenethiol, benzenethiol, and 4-mercaptobenzoic acid (except for 100 mM) molecules. Benzenethiol shows increase in rate constant up to 75 mM. 59

Figure 3.5. Time dependent SERS signals for 10 µM molecular concentration on IE Ag@Au@SiO_2 nanoparticles. Temporal profile of (A) 1067 cm^{-1} (CH bend/CS stretch) mode for 2-naphthalenethiol, (B) 1074 cm^{-1} (CS and CC symmetric stretch) mode for benzenethiol, (C) 1078 cm^{-1} (CC ring/CS stretch) for 4-mercaptobenzoic acid, and (D) 1079 cm^{-1} (CS stretch) for p-aminothiophenol molecules. The curves are: black = 4.0, red = 5.5, green = 6.6, blue = 7.5, and magenta = 9.0 pH solutions. SERS parameters as in Figure 3.2. 61

Figure 3.6. Rate constants determined for time dependent SERS signals as a function of solution pH. Data points are: black = 2-naphthalenethiol, red = benzenethiol, green = 4-mercaptobenzoic acid, and blue = p-aminothiophenol. Maximum rate constants are observed at pH 7.6, 6.6, 5.5, and 4.0 for 2-naphthalenethiol, benzenethiol, 4-mercaptobenzoic acid, and p-aminothiophenol, respectively. 64

Figure 3.7. Time dependent SERS signals for 10 µM molecular concentration on IE Ag@Au@SiO_2 nanoparticles. Temporal profile of (A) 1067 cm^{-1} (CH bend/CS stretch) mode for 2-naphthalenethiol, (B) 1074 cm^{-1} (CS and CC symmetric stretch) mode for benzenethiol, (C) 1078 cm^{-1} (CC ring/CS stretch) for 4-mercaptobenzoic acid, and (D) 1079 cm^{-1} (CS stretch) for p-aminothiophenol molecules. The curves are: black = 0, red = 5, green = 10, blue = 15, magenta = 20, and dark yellow =

25% MeOH in samples. The polarity of the solution is adjusted using dehydrated MeOH. SERS temporal curve indicate that maximum saturated SERS signals are observed at between 0 – 10% MeOH. SERS parameters as in Figure 3.2. 66

Figure 3.8. Rate constants determined for time dependent SERS signals as a function of solution polarity. Data points are: black = 2-naphthalenethiol, red = benzenethiol, green = 4-mercaptobenzoic acid, and blue = p-aminothiophenol. Rate constant increases up to 5% MeOH for 2-napthalenethiol and thiophenol. Maximum rate constant value is observed at 10% MeOH for charged molecules such as 4-mercaptobenzoic acid and p- aminothiophenol. 68

Figure 4.1. Ag@Au nanoparticles stabilized by (1) citrate, (2) silica shells, and (3) silica membranes. (A) Representative TEM images, (B) SERS spectra with the largest signal for 30 μM 2-aminothiophenol incubated with 6 nM nanoparticles, and (C) time-dependent SERS intensities. SERS parameters: λ_{ex} = 785 nm, t_{int} = 30 s, and P = 64 mW. Vibrational assignments: CC and CS stretch: 1587 cm^{-1}, CC stretch and CH bend: 1485 cm^{-1}, CC stretch and CH bend: 1173 cm^{-1}, CC and CS stretch: 1079 cm^{-1}, ring deformation: 1003 cm^{-1}, and ethanol: 876 cm^{-1}. 81

Figure 4.2. Evaluation of the dielectric properties of silica shells on Ag@Au nanoparticles. (A) LSPR spectra of (1) Ag@Au (λ_{max} = 539 nm) and (2) Ag@Au@SiO_2 (λ_{max} = 553 nm, silica shell thickness = 15.1 ± 6.8 nm) nanoparticles in water. (B) Shifts in the maximum LSPR wavelength as a function of bulk refractive index. Bulk refractive index was varied using 0-80% (w/v) sucrose solutions. Linear and non-linear refractive index sensitivities are 170 and 360 nm/RIU for the Ag@Au nanoparticles. The intersection point of the two curves represents the effective refractive– index on Ag@Au@SiO_2 nanoparticles. Furthermore, the LSPR decay length (l_d) is calculated to be ~11 nm according to the model. Error bars represent standard deviations from a minimum of three measurements..... 84

Figure 4.3. Determination of local effective refractive index for membrane stabilized Ag@Au@SiO_2 nanoparticles. (A) TEM images and (B) LSPR spectra of Ag@Au@SiO_2 nanoparticles after (1) 10 (λ_{max} = 551.9 nm, $\Delta\lambda_{max}$ = -1.1 nm), (2) 30 (λ_{max} = 547.9 nm, $\Delta\lambda_{max}$ = -5.1 nm), and (3) 40 (λ_{max} = 541.9 nm, $\Delta\lambda_{max}$ = -11.1 nm) minutes. (C) LSPR wavelength maximum shifts as a function of effective refractive index of silica membrane stabilized nanoparticles. The effective refractive index is estimated using the previously determined dielectric properties of the materials..... 86

Figure 4.4. SERS signals for 6 nM silica membrane stabilized Ag@Au nanoparticles incubated with 30 μM 4-aminothiophenol for at least 1 hour. Effective refractive index was varied from 1.36_6 to 1.45_8 and SERS intensity was plotted using the 1079 cm^{-1} CS/CC stretching frequency. At lower effective refractive indices, SERS intensities are limited by saturation of the metal surface area and volume near the metal surface whereas at high effective refractive indices, the volume near the metal surface is blocked by silica thereby reducing the

overall SERS intensity. Averages and standard deviations are reported using at least 3 measurements. Same SERS parameters as in Figure 4.1. 88

Figure 4.5. SERS data for 6 nM IE Ag@Au@SiO_2 nanoparticles with effective silica refractive index of 1.38 as a function of molecular concentration. (A) Maximum SERS spectra for (1) 1, (2) 2, (3) 5, (4) 20, and (5) 30 μM 4-aminothiophenol and (B) SERS intensity for the vibrational modes centered at (1) 1079 cm^{-1} (CC and CS stretches), (2) 393 cm^{-1} (CS bend), and (3) 1173 cm^{-1} (CC stretch and CH bend) as a function of 4-aminothiophenol concentration. Averages and standard deviations are reported using at least 3 measurements. Same SERS parameters as in Figure 4.1. 90

Figure 4.6. Nanoparticle concentration dependent (A) SERS spectra and (B) intensities for 30 μM 4-aminothiophenol. Nanoparticle concentration was varied from (1) 2, (2) 4, (3) 6, (4) 8, and (5) 10 nM 4-aminothiophenol. The samples were spiked with 1% ethanol, and the ethanol signal at 876 cm^{-1} was used to account for sample to sample focus variations. Vibrational assignments: CC and CS stretch: 1587 cm^{-1}, CC stretch and CH bending: 1173 cm^{-1}, CC and CS stretches: 1079 cm^{-1}, ethanol: 876 cm^{-1}, and CS bending: 393 cm^{-1}. Averages and standard deviations are reported using at least 3 measurements. Same SERS parameters as in Figure 4.1. 92

Figure 5.1. (A) Chemical structures of (1) 2-naphthalenethiol, (2) benzenethiol, (3) 4-mercaptobenzoic acid, and (4) p-aminothiophenol. (B) TEM image of internally etched Ag@Au@SiO_2 nanoparticles with nanoparticle diameter of 81.4 ± 15.7 nm and an effective refractive index of 1.38. (C) Representative LSPR spectra of internally etched Ag@Au@SiO_2 nanoparticles (1) before (black) and (2) after (red) incubation with the thiolated molecules. (D) Shifts in the λ_{max} of 6 nM IE Ag@Au@SiO_2 nanoparticles incubated for 1 hour in (1) 2-naphthalenethiol, (2) benzenethiol, (3) 4-mercaptobenzoic acid, and (4) p-aminothiophenol. Error bars represent the standard deviation of the $\Delta\lambda_{max}$ changes from at least three replicate measurements. Lines represent analysis using the Langmuir adsorption model. 105

Figure 5.2. SERS spectra as a function of molecular concentration using 6 μM IE Ag@Au@SiO_2 nanoparticles with effective refractive index of 1.38. (A) SERS spectra for (1) 2, (2) 5, (3) 15, (4) 30, and (5) 40 μM 2-naphthalenethiol. (B) SERS spectra for (1) 2, (2) 5, (3) 10, (4) 20, and (5) 32 μM benzenethiol. (C) SERS spectra for (1) 4, (2) 8, (3) 12, (4) 20, and (5) 32 μM 4-mercaptobenzoic acid. (D) SERS spectra for (1) 1, (2) 2, (3) 5, (4) 20, and (5) 30 μM p-aminothiophenol. (E) Representative orientation of 2-naphthalenethiol, benzenethiol, 4-mercaptobenzoic acid, and p-aminothiophenol on Ag@Au surface. All vibrational mode assignments are found in Table 1. SERS parameters: λ_{ex} = 785 nm, t_{int} = 30 s, and P = 64 mW. 109

Figure 5.3. SERS signals as a function of molecular concentration and vibrational mode. (A) SERS intensity for (1) 1067 cm^{-1} (CH bend/CS stretch), (2) 368 cm^{-1} (CS bend), and (3) 1380 cm^{-1} (ring stretch) as a function of 2-naphthalenethiol concentration. (B) SERS intensity for (1) 1074

cm^{-1} (CS/CC symmetric stretch), (2) 420 cm^{-1} (CS stretch and CCC in plane bend), and (3) 1573 cm^{-1} (ring stretch) as a function of benzenethiol concentration. (C) SERS intensity for (1) 1078 cm^{-1} (CS/CC ring stretch), (2) 713 cm^{-1} (CCC out of plane bend), and (3) 1585 cm^{-1} (ring stretch) as a function of 4-mercaptobenzoic acid concentration. (D) SERS intensity for (1) 1079 cm^{-1} (CS stretch), (2) 393 cm^{-1} (CS bend), and (3) 1173 cm^{-1} (CH bend) as a function of p-aminothiophenol concentration. Averages and standard deviations represent those of 3 measurements. Same experimental conditions as in Figure 2. 114

Figure 5.4. Langmuir adsorption isotherm analysis for CS stretching mode. (A) Linear transformations of the Langmuir adsorption isotherm fitted to SERS data and (B) equilibrium parameter calculations for (1) 2-naphthalenethiol, (2) benzenethiol, (3) 4-mercaptobenzoic acid, and (4) p-aminothiophenol. 116

Figure 5.5. Langmuir adsorption isotherm model analysis. (A) Linear transformation of Langmuir model fitted to CC ring stretching mode at 1380, 1575, and 1587 cm^{-1} for (1) 2-naphthalenethiol, (2) benzenethiol, and (3) 4-mercaptobenzoic acid; and CH bending mode at 1176 cm^{-1} for (4) p-aminothiophenol. (B) Linear transformation of Langmuir model fitted to CS bending mode at 368 and 393 cm^{-1} for (1) 2-naphthalenethiol and (4) p-aminothiophenol; CCC in plane bend/CS stretching at 420 cm^{-1} for (2) benzenethiol; and CCC out of plane bending at 713 cm^{-1} for (3) 4-mercaptobenzoic acid. Correlation coefficient R^2 for Langmuir isotherms are at least 0.96. Calculated Langmuir isotherm parameters are listed in Table 5.4. 118

Figure 6.1. Characterization of silica coated Au nanospheres (1), Ag@Au nanospheres (2), and Au nanorods (3) using (A) TEM and (B) LSPR. TEM analysis show that silica is uniformly coated on the surface of nanoparticles. Dimensions of nanoparticles are (1) 45.3 ± 2.7 nm, (2) 87.1. ± 4.7 nm, and (3) 89.2 nm × 64.8 nm. LSPR analysis show tuneable extinction maximum wavelengths (λ_{max}) from Au nanospheres to Au nanorods. Extinction maximum wavelengths (λ_{max}) for silica coated nanoparticles are (1) 525.2 nm; (B) 560.1 nm; and (C) 673.4 nm. 132

Figure 6.2. (A) TEM images of IE (1) Au@SiO_2 and (2) Ag@Au@SiO_2 nanoparticles. TEM analysis reveal that the average nanoparticle diameters are: (1) 44.6 ± 3.5 nm and (2) 69.6 ± 3.4 nm, with core diameters of (1) 12.6 ± 1.4 nm and (2) 17.7 ± 4.1 nm for IE Au@SiO_2 and Ag@Au@SiO_2 nanoparticles; respectively. LSPR (A) and SERS (B) analysis of (1) 2.5, (2) 4.9, and (3) 10.0 nM IE Au@SiO_2 nanoparticles; and (4) 2.5 nM IE Ag@Au@SiO_2 nanoparticles incubated with p-aminothiophenol monolayer for 1 hour. LSPR shows λ_{max} of (1 – 3) 522.6 and (4) 558.2 nm for IE Au@SiO_2 and IE Ag@Au@SiO_2 nanoparticles. Extinction at 632.8 nm are: (1) 0.076, (2) 0.15, (3) 0.29, and (4) 0.65 AU. The extinction at 632.8 nm for IE Ag@Au@SiO_2 nanoparticles is greater than IE Au@SiO_2 nanoparticles in all cases. SERS spectra show CS stretching mode of 4-aminothiophenol at 1079 cm^{-1} indicative of molecule binding to the metal surface through sulfur. IE Ag@Au@SiO_2 nanoparticle exhibit

higher SERS S/N compared to IE Au@SiO_2 nanoparticles for a fixed (1) nanoparticle concentration, (2) total nanoparticle surface area, or (3) extinction at λ_{max}. SERS parameters: λ_{ex} = 632.8 nm, t_{int} = 10 s, and P = 2 mW. 135

Figure 6.3. LSPR and TEM analysis of IE Au@SiO_2 nanoparticles. (A) Extinction spectrum of Ag nanoparticles used in synthesis of IE Ag@Au@SiO_2 nanoparticles. Ag nanoparticles show λ_{max} of 394.6 nm with Γ of 46.5 nm. Inset shows TEM image of Ag nanoparticles with average diameter = 13.1 ± 5.2 nm. (B) LSPR spectra of Ag@Au nanoparticles with various shell thicknesses synthesized from same Ag core. λ_{max} values are: (1) 554.1, (2) 549.0, and (3) 535.7 nm. (C) LSPR spectra of IE Ag@Au@SiO_2 nanoparticles etched for effective silica refractive index of ~1.38. λ_{max} of IE Ag@Au@SiO_2 nanoparticles are: (1) 560.8, (2) 555.8 , and (3) 538.9 nm. Insets in (B) and (C) clearly show differences in λ_{max} values for samples 1 – 3. TEM images of IE Ag@Au@SiO_2 nanoparticles with various Au shell thickness. (D) TEM analysis show that the average nanoparticle core diameters are: (1) 17.7 ± 4.1 nm, (2) 21.6 ± 6.7 nm, and (3) 26.0 ± 5.4 nm with total diameters of (1) 69.6 ± 13.4 nm, (2) 67.0 ± 8.3 nm, and (3) 76.9 ± 7.7 nm; respectively. 140

Figure 6.4. LSPR spectra of IE Ag@Au@SiO_2 nanoparticles for a fixed (A) nanoparticle concentration (= 2.5 nM) and (B) nanoparticle extinction (=1.5) at LSPR λ_{max}. λ_{max} values for IE Ag@Au@SiO_2 nanoparticles are: (1) 560.8, (2) 555.8 , and (3) 538.9 nm. Correlated SERS spectra collected by addition of monolayer p-aminothiophenol in IE Ag@Au@SiO_2 nanoparticles with a fixed (C) nanoparticle concentration and (D) nanoparticle extinction at LSPR λ_{max}. SERS parameters: λ_{ex} = 632.8 nm, t_{int} = 10 s, and P = 2 mW. 141

Figure 6.5. (A) LSPR of IE Ag@Au@SiO_2 nanoparticles incubated in 10 µM 4-aminothiophenol for 96 hours. LSPR λ_{max} of the sample is 544.1 nm. Dotted lines represent Raman excitation wavelengths at 532, 632.8, and 785 nm used to generate SERS signals. (B) SERS spectra collected with (1) 532, (2) 632.8, and (3) 785 nm Raman excitation systems. SERS spectra shown are normalized with 1049 cm^{-1} ethanol peak in order to account for differences in detector response. It is observed that 633 nm Raman excitation system provides highest SERS; whereas, 1079 cm^{-1} peak signal is smallest with 785 nm Raman excitation system. SERS parameters: λ_{ex} = 532 nm (LP = 9.1 mW), 632.8 nm (LP = 2 mW), 785 nm (LP = 60 mW), and t_{int} = 10 s. 145

Figure 6.6. Diagram of charge transfer resonance mechanism in SERS. The charge transfer occurs from metal energy state closer to the Fermi level to LUMO of p-aminothiophenol. 147

CHAPTER 1 AN OVERVIEW OF EXISTING SERS SUBSTRATES, APPLICATIONS, LIMITATIONS, AND CURRENT APPROACHES FOR OVERCOMING CHALLENGES ASSOCIATED WITH SOLUTION-PHASE SERS SUBSTRATES

1.1 Introduction

Nanoparticles are small structures that have at least one dimension ranging from 1 – 100 nm.[1-4] Nanoparticles possess many unique chemical and physical properties that are different from bulk materials.[5-7] For example, bulk gold does not exhibit catalytic properties; however, gold nanoparticles with diameters less than 4 nm revealed catalytic activity.[1, 5] Nanoscale-based properties depend on chemical composition, local dielectric environment, shape, size, and surface chemistry.[6, 9-11] Controlling these parameters is vital for achieving predictable nanoparticle properties for successful integration in applications such as biological sensors,[12-16] catalysis,[5] drug delivery,[17-18] plasmonic devices,[19-21] and optical filters.[20, 22]

Notably, the optical properties of noble metal nanoparticles such as copper, gold, and silver are widely exploited for molecular detection using surface enhanced Raman scattering (SERS).[23-29] SERS partially relies on the optical properties of noble metal nanoparticles that arise when the free conduction electrons in the nanoparticles interact with incident electromagnetic waves. For instance, noble metal nanoparticles with diameters much smaller than the wavelength of light can exhibit a surface plasmon resonance, which is a collective in-phase oscillation of the free electrons within the conduction band of the metal nanoparticle induced by the incident electric field.[1, 29-31] If the nanoparticles are small such that the collective oscillation occurs only on a particle

surface, the phenomenon is called the localized surface plasmon resonance (LSPR).[29, 31] The energy and the width of LSPR spectral features depend on the free electron density, dielectric medium, and characteristic electron scattering time.[1, 31]

Gustav Mie first described the LSPR by solving Maxwell's equation for light interacting with small metallic spheres.[1] Mie theory assumes that spherical particles are immersed in a uniform medium so that an electrostatic dipole approximation can be used. As a result, the optical property of nanoparticles can be described in terms of wavelength dependent extinction (sum of both absorbance and scattering).[1, 31] Equation 1.1 describes nanoparticle extinction as follows[9]

$$\mathrm{E}(\lambda) = \frac{24\pi^2 \mathrm{Na}^3 \varepsilon_{\mathrm{m}}^{3/2}}{\lambda \ln(10)} \left[\frac{\varepsilon_{\mathrm{i}}}{\left(\varepsilon_{\mathrm{r}} + \chi \varepsilon_{\mathrm{m}}\right)^2 + \varepsilon_{\mathrm{i}}^2} \right] \tag{1.1}$$

where E(λ) is the extinction at a particular wavelength; N is the number density of nanoparticles; a is the nanoparticle radius; ε_m is the surrounding medium dielectric constant; ε_r and ε_i are the real and imaginary metal dielectric functions, respectively; λ is the wavelength of light; and χ is the nanoparticle aspect ratio (2 for a sphere). Equation 1.1 clearly indicates that nanoparticle optical properties depend on shape, size, metal dielectric functions, and the external dielectric environment. In addition to the large extinction spectrum, a second consequence of the LSPR is the formation of large electric fields on the nanoparticle surface. As such, nanoparticles that exhibit LSPR properties also serve as excellent substrates for surface enhanced spectroscopies including SERS thereby allowing for trace and direct detection of molecules.[32-34]

1.2 Raman Spectroscopy

Raman scattering is a form of rotational and vibrational spectroscopy that is complementary to infrared absorption spectroscopy and provides unique molecular fingerprint information.[35] Raman scattering is a process in which a monochromatic light of energy $h\nu_0$ excites an electron in a molecule to a virtual state. The virtual state energy is not a true molecular quantum state but a very short-lived distortion state of the electron cloud caused by the oscillating incident electromagnetic radiation.[36] The excited electrons relax to the ground energy state via elastic or Rayleigh scattering (i.e., at the same energy as the incident light ($h\nu_0$)).[36] Some of the energy is transferred to vibrational energy such that some scattered photons exhibit a lower energy ($h\nu_0 - h\nu_1$) relative to the incident light in a process called Stokes Raman scattering. The energy difference $\Delta h\nu_{01}$, between the incident and scattered photon energy is equal to the molecular vibrational energy.[36-38] Electrons in a molecule can also be in an excited vibrational state when the incident photon interacts with a molecule. When this occurs, energy can be transferred to the photon from the vibration resulting in an energy gain via an anti-Stokes Raman scattering process.[36, 38]

Vibrational energies detected using Raman scattering depends on the quantized energy states associated with the vibrational and rotational motions of molecular bonds. If a molecule exhibits a unique structure, mass, and bond strength; unique energies will appear as vibrational energies shifted from the Rayleigh line in a Raman spectrum. Small changes in the quantized energies can be related to small changes in polarizability that occurs in response to electromagnetic radiation, changes in the local environment, and/or surface adsorption (for SERS). In addition to unique vibrational energies, Raman

vibrational modes are narrower than complementary infrared spectral features thereby allowing direct identification of similar molecules in a complex sample matrix.[39-40] For example, Raman peak widths are usually 10-100 times narrower than most fluorescence bands and up to 10 times narrower than most infrared absorption bands.[41-42] In addition, Raman is a label-free, non-destructive, and direct detection technique with minimal to no sample preparation required. These advantages of Raman spectroscopy encourage the development of applications in the qualitative and quantitative analysis of matter.[39, 41, 43-45]

1.3 SERS and Molecular Detection

While Raman spectroscopy offers many advantages for molecular detection, this approach is limited by low signal to noise because only 1 photon out of 10^9 incident photons undergoes Raman scattering.[35-36] Additionally, Raman scattering cross sections are small ($10^{-29} – 10^{-31}$ cm^2/sr) compared to typical fluorescence cross sections (10^{-16} cm^2/sr) or infrared cross sections (10^{-21} cm^2).[39, 44-47] To overcome this difference in cross section and deem Raman scattering an effective detection method, enhancement processes such as resonance Raman or SERS are used.[15, 27, 48-50] SERS,[29, 33, 51] in particular, is a surface sensitive technique that utilizes nanoparticles to increase molecular signals by 2 – 9 orders of magnitude,[33-34, 52] which allows pico molar to single molecule detection limits.[51-53] Fleischmann observed SERS for the first time from a monolayer of adsorbed pyridine on an electrochemically roughened silver electrode surface but attributed this signal increase to an increase in surface area.[54] Later, Van Duyne hypothesized that the million fold signal enhancement arose from electromagnetic effects from the roughened silver surface.[33]

Since this time, various experimental and theoretical studies were done to understand the mechanism of SERS and include both chemical and electromagnetic mechanisms resulting from adsorbate and nanoparticle interactions.[8, 35] Figure 1.1 illustrates four different mechanistic contributions to SERS enhancements and include (A) ground state chemical enhancement that arises from chemical interactions between a

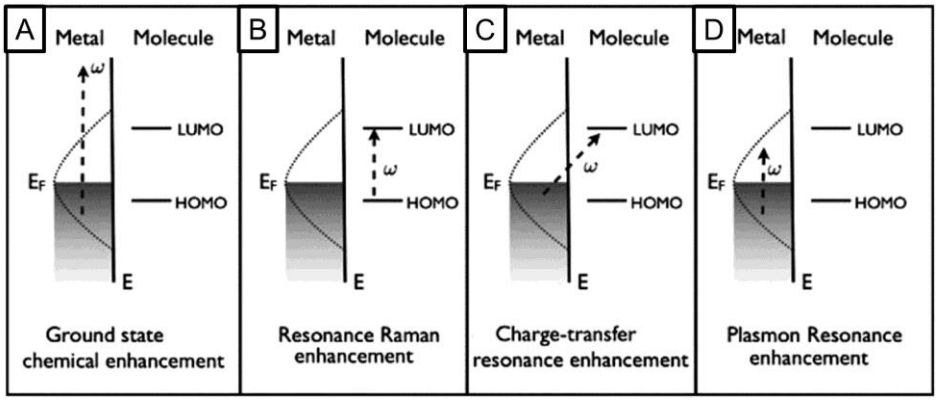

Figure 1.1. Scheme of common SERS enhancement mechanisms. (A) Ground state chemical enhancement as a result of chemical interactions between molecule and nanoparticle, (B) resonance Raman resulting from excitation energy resonance with molecular transition, (C) charge-transfer resonance Raman effect as a result of excitation energy in resonance with nanoparticle-molecule charge transfer transitions, and (D) plasmon resonance enhancement that arises from the strong local electromagnetic field when the excitation energy is in resonance with the nanoparticle plasmon.[8]

molecule and nanoparticle, (B) resonance Raman enhancement that results when the excitation energy is in resonance with the molecular HOMO to LUMO transitions and selectively increases some vibrational modes of dye molecules, (C) charge-transfer resonance effects resulting from excitation energy in resonance to the molecule-nanoparticle charge transfer transitions observed in molecules with π-systems, and (4) plasmon enhancement resulting from strong nanoparticle electromagnetic field when the excitation energy is in resonance with the LSPR.[8, 55] The first three processes (A to C) are

often grouped under chemical enhancement mechanisms, which contribute up to 2 orders of magnitude in signal enhancement[33, 56-58] and is a short-range (< 2 nm)[56, 59-60] effect.[61-63] As a consequence, the nanoparticle interface plays a key role in the magnitude of chemical enhancement obtained. In comparison, electromagnetic enhancements can exceed 9 orders of magnitude[56, 60, 64] and depend on the large electric fields that form on the surface of material when a plasmon resonance is induced. In comparison to chemical enhancement effects, higher electromagnetic SERS enhancements are possible because both the incident electric field ($E(\omega)_{laser}$) of the laser light and the scattered Raman ($E(\omega)_{Raman}$) are impacted upon interaction with the LSPR. As such, the total SERS electromagnetic enhancement factor is $|E_{laser}|^2 \cdot |E_{Raman}|^2$. For a small Raman shifts, E_{laser} and E_{Raman} are assumed to be ~equal; therefore, the SERS enhancement scales as a factor of $|E(\omega)|^4$.[63, 65-66]

One motivator in using SERS is the large signal enhancement achieved thus allowing for trace biological[67-68] and environmental[69-70] species detection. Although SERS is a powerful technique and can be used for single molecular detection,[51-53] trace chemical analysis is limited by poor reproducibility and small dynamic ranges. An important need to improve the analytical and general performance capabilities of SERS-active substrates is being addressed through rational substrate design[70] as well as by controlling the composition, shape, size, and surface chemistry of nanoparticles.[35]

1.4 SERS Substrates and Applications

SERS substrates are routinely fabricated and synthesized using noble metals including copper, gold, and silver. Several key goals of SERS substrates include:[1, 35] (1) high SERS activity (enhancements approaching 10^9 vs. normal Raman scattering);[71] (2)

uniform SERS enhancement (deviations < 20%); (3) substrate stability and reproducibility; and (4) either cheap or reusable. Various approaches to prepare SERS substrates are summarized below and include electrochemical roughened substrates, nano-assembled substrates, substrates fabricated from nanosphere lithography, nanolithography substrates, and colloidal nanoparticles.

SERS enhancement was first reported for electrochemically roughened silver electrodes; however, these substrates are easy to prepare and low cost but are not wisely used because of the shape and size heterogeneity.[54, 72] Nanoscale roughness features are generated using oxidation-reduction cycles[72-73] and used to perform potential dependent studies, molecular detection,[33, 54, 74-75] or for transition metal adsorption investigations.[35, 54, 76] SERS enhancements ranging from $10^4 – 10^6$ were reported for Ag, Au, and Cu substrates and variations in these are attributed to non-uniform surface roughness.[33, 35, 54, 77]

In comparison to electrochemically roughened silver electrodes, SERS substrates prepared using nanoassembly contain more ordered nanostructures.[78] One of the simplest fabrication nanoassembly based substrates are self-assembled gold nanoparticles on a substrate directly from solution. To improve ordering and attachment, aminated or thiolated silanes can be used to attach metal nanoparticles onto a glass substrate. The advantage of substrates prepared using self-assembly is the ability to fine tune the LSPR by controlling inter-particle spacing. These substrates were used for the detection of various biomolecules such as antibodies, DNA, proteins, and neurotransmitters[79-82] with enhancements of up ~10^8.[83] In all cases, nanoparticle surface density and uniformity depend on the concentration, size, surface charge of/on the nanoparticles.[35, 84] To improve

assembly and improve inter-particle spacing uniformity, capping agents such as CTAB can be used;[83] however, SERS signals vary from spot to spot on the substrate, which leads to difficulties in reproducibility.[35, 85-86]

To improve on spot to spot reproducibility, nanosphere lithography can be used. The fabrication approach utilizes a self-assembled polystyrene/silica nanosphere mask that can be for patterning Ag or Au nanostructures. Metal depositions occur via physical vapor or electrochemical deposition techniques. Physical vapor deposition without template removal leads to the formation of a metal film over nanosphere substrate.[59, 87] The removal of nanosphere mask by sonication results in formation of metal nanotriangles.[88] Additionally, electrochemical deposition of metals followed by removal of mask template generates thin hexagonal arrays of metal nanoislands, nanobowls, or nanovoids. The size and distance between the nanotriangles are tuned by changing the size of polystyrene nanospheres used. SERS substrates fabricated using nanosphere lithography can be performed using large scale production methods; and the size, shape, and spacing of nanostructures generated can easily be tuned by controlling the size of the nanospheres used or thickness of the deposited metal.[28] Using these substrates, detection of molecules[89] as well as the distance and LSPR wavelength maximum dependencies on SERS were thoroughly evaluated.[90-91] In general, electrochemically deposited metal film over nanosphere substrates exhibit high ($> 10^8$) SERS enhancements [83] whereas nanotriangles are excellent LSPR based sensors.[16, 92-93]

One of the drawbacks to nanosphere lithography is that interparticle spacing and in-plane nanoparticle dimensions are not independently controlled. To achieve independent control over these parameters, micro- and nano-fabrication techniques such

as electron beam lithography, chemical vapor deposition, and/or reactive ion etching can be used.[1, 94-95] In comparison to other fabrication methods, nanolithography provides flexibility in fabricating SERS substrate with diverse shapes, sizes, and spacings (>10 nm)[35] that are highly uniform and reproducible.[96-98] SERS enhancements ranging from 10^5 - 10^9 were reported.[95-96]

While nanolithography substrates contain well-defined characteristics, the products are time-consuming to make, labor extensive, and costly. In contrast, colloidal solution-phase nanoparticles are often use for the easier to make for less money.[1, 27, 35, 48, 72] These bottom-up synthesized materials are formed by reducing metal salts with

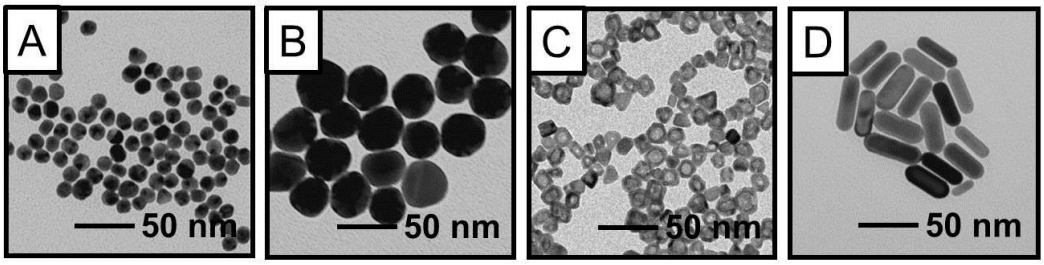

Figure 1.2. Representative TEM images of bottom-up synthesized nanoparticles with different compositions, shapes and sizes. (A) Au nanospheres (diameter (d) = 12.3 ± 1.1 nm), (B) 33.4 nm Au nanospheres (d = 33.4 ± 3.0 nm), (C) Ag@Au core-shell nanospheres (d = 14.5 ± 2.9 nm), and (D) Au nanorods (length = 45.4 ± 7.7 nm, width = 16.2 ± 3.2 nm).

reducing agents such as sodium borohyride, sodium citrate, or alcohols.[84, 99-101] Surfactants such as cetryl trimethylammonium bromide (CTAB), poly vinyl pyrrolidone (PVP), or sodium dodecyl sulfate (SDS) can be used as capping agents to prevent aggregation or oxidation of nanoparticles as well as to control growth rates and growth direction. Depending on the solution parameters used and how well nucleation and growth conditions are controlled, various shapes and sizes can be realized.[1, 102-103]

Transmission electron microscopy (TEM) images of some of these solution-phase nanoparticles are shown in Figure 1.2. Often, nanoparticles synthesized using these processes are amorphous/poly-crystalline/facetted. As a result, broad particle distributions are often observed.[104-105] Improvements in nanoparticle size and shape have yielded tunable structures ranging from spheres, cubes, rods, rings, core-shell, to wires.[106-113] These nanoparticles can be either patterned on substrates or directly used in solution for SERS. SERS enhancements can be controlled by varying the LSPR properties of these nanoparticles and through aggregation so that intense electromagnetic fields are generated (when inter-particle distances < 2 nm).[114-115] Utilizing these hotspots is ideal if molecular identification is the objective; however, quantification using these is limited.[27, 35]

1.5 Advantages and Limitations of Solution-Phase SERS Substrates

Solution-phase nanoparticles are widely used in SERS because of their low cost, straight-forward syntheses, and electromagnetic tunability. For these bottom-up synthesized solution-phase nanoparticles, agglomeration and aggregation occur as molecules adsorb onto the nanoparticle surfaces. This can lead to coupling of the LSPR of these substrates and limits quantitative and reproducible SERS measurements.[27, 116] Furthermore, the aggregation and sedimentation kinetics depend on the molecules, nanoparticles, and assay times all of which influence both nanoparticle plasmonics and SERS measurements.[27, 117-119]

For example, Figure 1.3 shows time-dependent LSPR and SERS signals collected using gold nanospheres (diameter = 12.3 ± 1.1 nm) incubated with 10 μM 4-

aminothiophenol. Upon addition of the molecule, both the LSPR signal at 785 nm and the SERS signal at a unique vibrational frequency increase initially and are followed by decaying signals. The LSPR data reveal a less sensitive time dependent signal change vs. the SERS data, which show a much greater signal intensity change as a function of time. This is reasonable given that SERS signals scale as $|E|^4$ while LSPR scales as $|E|^2$; therefore, we expect that SERS signals would be more sensitive to spectral variations vs. LSPR signals. Clearly, these processes are complex and depend on many factors. As such, time-dependent SERS signals are often difficult to predict.

Some progress in experimental expectations has been made. The effects of sonication time, mixing time, and storage conditions were evaluated for SERS measurements.[116] Although optimized mixing times were shown to result in more reproducible metal cluster formation, many parameters including solution conditions, nanoparticle morphology and concentration, and molecular parameters required optimization to achieve reproducible SERS data.

In addition to evaluating these standard experimental parameters, nanoparticles are routinely functionalized with biomolecules,[120] surfactants,[121-122] and polymers[123] to improve their predictable use in SERS assays. Often easily displaced surface ligands are used to prevent aggregation initially for subsequent displacement by target molecules. These weakly bound ligands, however, are prone to degradation or desorption in solution during SERS assays.[124] To overcome this limitation and to improve the robustness of solution-phase nanoparticles as SERS substrates in harsh solution conditions (pH, ionic strength, temperature, etc.), sol-gel chemistry can be used to stabilize the nanostructures.[99, 125-129] These silica layers, however, occupy the volume near the surface

where the electromagnetic fields are largest thus reducing the SERS effect.[48] To overcome this limitation, molecules must overcome this distance dependence requirement.[49, 130] Consequently, molecular size and diffusion through the microporous

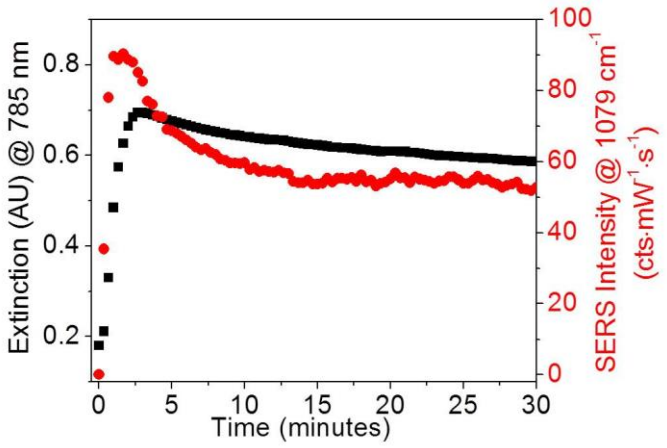

Figure 1.3. Time dependent LSPR (black) and SERS (red) signals for 4 nM gold nanospheres incubated with 10 µM 4-aminothiophenol. Both the extinction monitored at 785 nm and SERS intensity at 1079 cm^{-1} show that the spectroscopic signals initially increase then decrease over time as a result of variations in nanoparticle plasmonics.

silica also plays an important role in SERS.[99, 131-133]

To overcome the challenge of maintaining solution-phase nanoparticle stability as well as using these nanostructures as SERS substrates, several research groups have utilized selective etching of silica shells to form silica membranes.[99, 133-134] These silica membranes are etched using salt, temperature, or basic conditions to increase the porosity of the silica membrane thus freeing the metal surface for SERS and other applications. Because electromagnetic coupling between the metal cores is prevented by the silica membrane, average SERS enhancements of only ~10^2 with ~10% SERS signal variation was reported for etched silica coated gold nanospheres.[99] Agglomeration and aggregation

of these structures still occurred; however, consistent and reproducible SERS measurements were reported because the LSPR properties of the materials were maintained (i.e., minimal to no electromagnetic coupling between nanoparticles occurs upon aggregation). To improve the overall SERS enhancements, other structures such as gold coated silver (Ag@Au) nanoparticles or gold nanorods could be used to provide larger SERS enhancements for both the quantitative and reproducible SERS detection of small molecules.

1.6 Thesis Overview

This thesis focuses on understanding implications of nanomaterial quality control and mass transport through internally etched silica coated nanoparticles for direct and quantitative molecular detection using SERS. Chapter 2 demonstrates the application of surfactant-free size exclusion chromatography for separating silica coated nanoparticles as a function of diameter with modest fractionation. Purification of nanoparticles through fractionation using column chromatography improves the quality of these nanomaterials and reproducibility of their function in subsequent use. Chapter 3 focuses on studying selective molecular transport through internally etched nanoparticles by monitoring SERS. SERS signals associated with transport and adsorption of 2-naphthalenethiol, benzenethiol, 4-mercaptobenzoic acid, and p-aminothiophenol on metal core are modeled and evaluated using first-order time dependent Langmuir isotherm as a function of solution ionic strength, pH, and polarity. Molecular detection is achieved when the molecules first partition through the silica membrane then interact with the metal surface at short distances (i.e., less than 2 nm). Chapter 4 focuses on understanding the implication of silica effective refractive index on SERS signals. Refractive index

sensitivity modeling is applied to generate refractive index sensitivities and decay lengths for Ag@Au nanoparticles. Furthermore, for a fixed 3D SERS-active volume, the SERS intensities of unique molecular vibrational modes for a given molecule are shown to increase as the number of molecules that occupy SERS-active volume increases. SERS signals are achieved via both chemical and electromagnetic enhancement mechanisms as long as the vibrational modes are oriented perpendicular to the metal surface (i.e., parallel to the local electric field). SERS signals increase with molecular concentration until the three-dimensional SERS volume is saturated. SERS signal is also shown to increase with nanoparticle concentration for at least a monolayer molecular concentration. Chapter 5 studies implication of molecular orientation and surface selection rules on SERS. Langmuir adsorption isotherm models for 2-naphthalenethiol, benzenethiol, 4-mercaptothiophenol, and p-aminothiophenol adsorption on Ag@Au surface indicate favorable binding for charged molecules such as 4-mercaptobenzoic acid and p-aminothiophenol compared to neutral 2-naphthalenethiol and benzenethiol. Using unique molecular vibrational mode of p-aminothiophenol, SERS intensities using various nanoparticle core compositions, optical properties, and Raman excitation wavelengths are studied and compared in Chapter 6. In addition charge transfer resonance implication in SERS spectral changes are also studies for internally etched nanoparticles using 3 different Raman excitation wavelengths. Finally, Chapter 7 presents the conclusions and future directions. By incorporating careful quality control and nanostructure surface chemistry design, an understanding of molecular transport through internally etched silica matrices coated on metal nanoparticles is studied. Furthermore, important experimental and materials design parameters are learned that can subsequently be applied to the direct

and quantifiable detection of small molecules in real samples without the need for lengthy separations and assay times.

1. Cao, G., *Nanostructures and Nanomaterials: Synthesis, Properties and Applications*; Imperial College Press: London, 2004.
2. Boo, D. W.; Oh, W. S.; Kim, M. S.; Kim, K.; Lee, H.-C., Surface-Enhanced Raman Scattering (Sers) on Chemically Prepared Silver Film. *Chem. Phys. Lett.* **1985**, *120*, 301-306.
3. Zeng, S.; Yong, K.-T.; Roy, I.; Dinh, X.-Q.; Yu, X.; Luan, F., A Review on Functionalized Gold Nanoparticles for Biosensing Applications. *Plasmonics* **2011**, *6*, 491-506.
4. Buzea, C.; Pacheco, I.; Robbie, K., Nanomaterials and Nanoparticles: Sources and Toxicity. *Biointerphases* **2007**, *2*, MR17-MR71.
5. Zhou, X.; Xu, W.; Liu, G.; Panda, D.; Chen, P., Size-Dependent Single Au-Nanoparticle Catalysis. *J. Am. Chem. Soc.* **2010**, *132*, 138-146.
6. Claridge, S. A. L., H.W.; Basu,S.R.; Fr?het,J.M.J.; Alivisatos,A.P, Isolation of Discrete Nanoparticle-DNA Conjugates for Plasmonic Applications. *Nano Lett.* **2008**, *8*, 1202-1206.
7. Burda, C.; Chen, X.; Narayanan, R.; El-Sayed, M. A., Chemistry and Properties of Nanocrystals of Different Shapes. *Chemical Reviews* **2005**, *105*, 1025-1102.
8. Jensen, L.; Aikens, C. M.; Schatz, G. C., Electronic Structure Methods for Studying Surface-Enhanced Raman Scattering. *Chem. Soc. Rev.* **2008**, *37*, 1061-1073.
9. Kreibig, U.; Vollmer, M., *Cluster Materials*; Springer-Verlag: Heidelberg, Germany, 1995; Vol. 25, p 532.
10. Haes, A. J.; Van Duyne, R. P., A Unified View of Propagating and Localized Surface Plasmon Resonance Biosensors. *Anal. Bioanal. Chem.* **2004**, *379*, 920-930.
11. Hutter, E.; Fendler, J. H., Exploitation of Localized Surface Plasmon Resonance. *Adv. Mater.* **2004**, *16*, 1685-1706.
12. Bauer, G.; Pittner, F.; Schalkhammer, T., Metal Nano-Cluster Biosensors. *Mikrochim. Acta* **1999**, *131*, 107-114.
13. Aizpurua, J.; Hanarp, P.; Sutherland, D. S.; Kall, M.; Bryant, G. W.; Garcia de Abajo, F. J., Optical Properties of Gold Nanorings. *Phys. Rev. Lett.* **2003**, *90*, 057401/1-057401/4.
14. Elghanian, R.; Storhoff, J. J.; Mucic, R. C.; Letsinger, R. L.; Mirkin, C. A., Selective Colorimetric Detection of Polynucleotides Based on the Distance-Dependent Optical Properties of Gold Nanoparticles. *Science* **1997**, *227*, 1078-1080.
15. Haes, A. J.; Van Duyne, R. P., Nanoscale Optical Biosensors Based on Localized Surface Plasmon Resonance Spectroscopy. *Proc. SPIE* **2003**, *5221*, 47-58.
16. Riboh, J. C.; Haes, A. J.; McFarland, A. D.; Yonzon, C. R.; Van Duyne, R. P., A Nanoscale Optical Biosensor: Real-Time Immunoassay in Physiological Buffer Enabled by Improved Nanoparticle Adhesion. *J. Phys. Chem. B* **2003**, *107*, 1772-1780.
17. Yin Win, K.; Feng, S.-S., Effects of Particle Size and Surface Coating on Cellular Uptake of Polymeric Nanoparticles for Oral Delivery of Anticancer Drugs. *Biomaterials* **2005**, *26*, 2713-2722.
18. McClean, S.; Prosser, E.; Meehan, E.; O'Malley, D.; Clarke, N.; Ramtoola, Z.; Brayden, D., Binding and Uptake of Biodegradable Poly-Dl-Lactide Micro- and Nanoparticles in Intestinal Epithelia. *European Journal of Pharmaceutical Sciences* **1998**, *6*, 153-163.
19. Andersen, P. C.; Rowlen, K. L., Brilliant Optical Properties of Nanometric Noble Metal Spheres, Rods, and Aperture Arrays. *Applied Spect.* **2002**, *56*, 124A-135A.

20. Dirix, Y.; Bastiaansen, C.; Caseri, W.; Smith, P., Oriented Pearl-Necklace Arrays of Metallic Nanoparticles in Polymers: A New Route toward Polarization-Dependent Color Filters. *Adv. Mat.* **1999**, *11*, 223-227.
21. Maier, S. A.; Brongersma, M. L.; Kik, P. G.; Meltzer, S.; Requicha, A. A. G.; Atwater, H. A., Plasmonics-a Route to Nanoscale Optical Devices. *Adv. Mat.* **2001**, *13*, 1501-1505.
22. Haynes, C. L.; Van Duyne, R. P., Dichroic Optical Properties of Extended Nanostructures Fabricated Using Angle-Resolved Nanosphere Lithography. *Nano Lett.* **2003**, *3*, 939-943.
23. Xia, Y.; Campbell, D. J., Plasmons: Why Should We Care? *J. Chem. Edu.* **2007**, *84*, 91.
24. Haes, A. J.; Zou, S.; Zhao, J.; Schatz, G. C.; Van Duyne, R. P., Localized Surface Plasmon Resonance Spectroscopy near Molecular Resonances. *J. Am. Chem. Soc.* **2006**, *128*, 10905-10914.
25. He, X.; Zhao, X.; Chen, Y.; Feng, J., The Evidence for Synthesis of Truncated Triangular Silver Nanoplates in the Presence of Ctab. *Mater. Charact.* **2008**, *59*, 380-384.
26. Sun, L.; Song, Y.; Wang, L.; Guo, C.; Sun, Y.; Liu, Z.; Li, Z., Ethanol-Induced Formation of Silver Nanoparticle Aggregates for Highly Active Sers Substrates and Application in DNA Detection. *J. Phys. Chem. C* **2008**, *112*, 1415-1422.
27. Pierre, M. C. S.; Mackie, P. M.; Roca, M.; Haes, A. J., Correlating Molecular Surface Coverage and Solution-Phase Nanoparticle Concentration to Surface-Enhanced Raman Scattering Intensities. *The Journal of Physical Chemistry C* **2011**, *115*, 18511–18517.
28. Haynes, C. L.; Van Duyne, R. P., Plasmon-Sampled Surface-Enhanced Raman Excitation Spectroscopy. *J. Phys. Chem. B* **2003**, *107*, 7426-7433.
29. Haes, A. J.; Haynes, C. L.; McFarland, A. D.; Schatz, G. C.; Van Duyne, R. P.; Zou, S., Plasmonic Materials for Surface-Enhanced Sensing and Spectroscopy. *MRS Bulletin* **2005**, *30*, 368-375.
30. Stuart, D. A.; Haes, A. J.; Yonzon, C. R.; Hicks, E. M.; Van Duyne, R. P., Biological Applications of Localised Surface Plasmonic Phenomenae. *IEE Proc: Nanobiotech.* **2005**, *152*, 13-32.
31. Kreibig, U.; Vollmer, M., *Optical Properties of Metal Clusters*; Springer: Berlin, 1995.
32. Emory, S. R.; Nie, S., Near-Field Surface-Enhanced Raman Spectroscopy on Single Silver Nanoparticles. *Anal. Chem.* **1997**, *69*, 2631-2635.
33. Jeanmaire, D. L.; Van Duyne, R. P., Surface Raman Spectroelectrochemistry. Part I. Heterocyclic, Aromatic, and Aliphatic Amines Adsorbed on the Anodized Silver Electrode. *J. Electroanal. Chem. & Interfac. Electrochem.* **1977**, *84*, 1-20.
34. Fang, P.; Li, J. F.; Yang, Z.; Li, L. M.; Ren, B.; Tian, Z., Optimization of Sers Activities of Gold Nanoparticles and Gold-Core–Palladium-Shell Nanoparticles by Controlling Size and Shell Thickness. *J. Raman Spect.* **2008**, *39*, 1679-1687.
35. Lin, X.-M.; Cui, Y.; Xu, Y.-H.; Ren, B.; Tian, Z.-Q., Surface-Enhanced Raman Spectroscopy: Substrate-Related Issues. *Anal. Bioanal. Chem.* **2009**, *394*, 1729-1745.
36. McCreery, R. L., *Raman Spectroscopy for Chemical Analysis*, 1 ed.; John Wiley & Sons, Inc.: New York, 2000; Vol. 157, p 420.
37. King, F. W.; Van Duyne, R. P.; Schatz, G. C., Theory of Raman Scattering by Molecules Adsorbed on Electrode Surfaces. *J. Chem. Phys.* **1978**, *69*, 4472-81.
38. Long, D. A., *Raman Spectroscopy*; McGraw-Hill Inc.: New York, 1977.
39. Biggs, K. B.; Camden, J. P.; Anker, J. N.; Duyne, R. P. V., Surface-Enhanced Raman Spectroscopy of Benzenethiol Adsorbed from the Gas Phase onto Silver Film over Nanosphere Surfaces: Determination of the Sticking Probability and Detection Limit Time†. *The Journal of Physical Chemistry A* **2009**, *113*, 4581-4586.

40. Dinish, U. S.; Balasundaram, G.; Chang, Y.-T.; Olivo, M., Actively Targeted in Vivo Multiplex Detection of Intrinsic Cancer Biomarkers Using Biocompatible Sers Nanotags. *Sci. Rep.* **2014**, *4*.
41. Cui, Y.; Ren, B.; Yao, J.-L.; Gu, R.-A.; Tian, Z.-Q., Multianalyte Immunoassay Based on Surface-Enhanced Raman Spectroscopy. *J. Raman Spect.* **2007**, *38*, 896-902.
42. Smith, B. C., *Infrared Spectral Interpretation: A Systematic Approach*; CRC Press: New York, 1999.
43. Pienpinijtham, P.; Han, X. X.; Ekgasit, S.; Ozaki, Y., Highly Sensitive and Selective Determination of Iodide and Thiocyanate Concentrations Using Surface-Enhanced Raman Scattering of Starch-Reduced Gold Nanoparticles. *Anal. Chem.* **2011**, *83*, 3655-3662.
44. Kudelski, A., Characterization of Thiolate-Based Mono- and Bilayers by Vibrational Spectroscopy: A Review. *Vib. Spect.* **2005**, *39*, 200-213.
45. Christesen, S. D., Raman Cross Sections of Chemical Agents and Simulants. *Applied Spect.* **1988**, *42*, 318-321.
46. Meyer, S. A.; Ru, E. C. L.; Etchegoin, P. G., Quantifying Resonant Raman Cross Sections with Sers. *J. Phys. Chem. A* **2010**, *114*, 5515-5519.
47. Aroca, R., *Surface-Enhanced Vibrational Spectroscopy*, 1st ed.; John Wiley & Sons. Ltd.: West Sussex, 2006.
48. Pierre, M. C. S.; Haes Amanda, J., Purification Implications on Sers Activity of Silica Coated Gold Nanospheres. *Anal Chem* **2012**, *84*, 7906-7911.
49. Roca, M.; Haes, A. J., Silica-Void-Gold Nanoparticles: Temporally Stable Surf Ace-Enhanced Raman Scattering Substrates. *J. Am. Chem. Soc.* **2008**, *130*, 14273-14279.
50. Moore, B. D.; Stevenson, L.; Watt, A.; Flitsch, S.; Turner, N. J.; Cassidy, C.; Graham, D., Rapid and Ultra-Sensitive Determination of Enzyme Activities Using Surface-Enhanced Resonance Raman Scattering. *Nat Biotech* **2004**, *22*, 1133-1138.
51. Kneipp, K.; Wang, Y.; Kneipp, H.; Perelman, L. T.; Itzkan, I.; Dasari, R. R.; Feld, M. S., Single Molecule Detection Using Surface-Enhanced Raman Scattering (Sers). *Phys. Rev. Lett.* **1997**, *78*, 1667-1670.
52. Nie, S.; Emory, S. R., Probing Single Molecules and Single Nanoparticles by Surface-Enhanced Raman Scattering. *Science* **1997**, *275*, 1102-1106.
53. Doering, W. E.; Nie, S., Single-Molecule and Single-Nanoparticle Sers: Examining the Roles of Surface Active Sites and Chemical Enhancement. *J. Phys. Chem. B* **2002**, *106*, 311-317.
54. Fleischmann, M.; Hendra, P. J.; McQuillan, A. J., Raman Spectra of Pyridine Adsorbed at a Silver Electrode. *Chem. Phys. Lett.* **1974**, *26*, 163-166.
55. Centeno, S. P.; López-Tocón, I.; Roman-Perez, J.; Arenas, J. F.; Soto, J.; Otero, J. C., Franck–Condon Dominates the Surface-Enhanced Raman Scattering of 3-Methylpyridine: Propensity Rules of the Charge-Transfer Mechanism under Reduced Symmetry. *The Journal of Physical Chemistry C* **2012**, *116*, 23639-23645.
56. Caldwell, W. B.; Chen, K.; Herr, B. R.; Mirkin, C. A.; Hulteen, J. C.; Van Duyne, R. P., Self-Assembled Monolayers of Ferrocenylazobenzenes on Au(111)/Mica Films: Surface-Enhanced Raman Scattering Response Vs Surface Morphology. *Langmuir* **1994**, *10*, 4109-15.
57. Dick, L. A.; McFarland, A. D.; Haynes, C. L.; Van Duyne, R. P., Metal Film over Nanosphere (Mfon) Electrodes for Surface-Enhanced Raman Spectroscopy (Sers): Improvements in Surface Nanostructure Stability and Suppression of Irreversible Loss. *J. Phys. Chem. B* **2002**, *106*, 853-860.
58. Wang, D. S.; Kerker, M., Enhanced Raman Scattering by Molecules Adsorbed at the Surface of Colloidal Spheroids. *Physical Review B* **1981**, *24*, 1777-1790.
59. Dick, L. A.; McFarland, A. D.; Haynes, C. L.; Van Duyne, R. P., Metal Film over Nanosphere (Mfon) Electrodes for Surface-Enhanced Raman Spectroscopy (Sers): Improvements in Surface Nanostructure Stability and Suppression of Irreversible Loss. *J. Phys. Chem. B* **2002**, *106*, 853-860.

60. Harpster, M. H., et al., Sers Detection of Indirect Viral DNA Capture Using Colloidal Gold and Methylene Blue as a Raman Label. *Biosens. Bioelectron.* **2009**, *25*, 674-681.
61. Schatz, G. C.; Young, M. A.; Van Duyne, R. P., Electromagnetic Mechanism of Sers. *Topics Ap. Phys.* **2006**, *103*, 19-46.
62. Schatz, G. C.; Van Duyne, R. P., *Electromagnetic Mechanism of Surface-Enhanced Spectroscopy*; Wiley: New York, 2002; Vol. 1, p 759-774.
63. Campion, A.; Kambhampati, P., Surface-Enhanced Raman Scattering. *Chem. Soc. Rev.* **1998**, *27*, 241-250.
64. McMahon, J. A.; Wang, Y. M.; Sherry, L. J.; Van Duyne, R. P.; Marks, L. D.; Gray, S. K.; Schatz, G. C., Correlating the Structure, Optical Spectra, and Electrodynamics of Single Silver Nanocubes. *J. Phys. Chem. C* **2009**, *113*, 2731-2735.
65. Kleinman, S. L.; Sharma, B.; Blaber, M. G.; Henry, A.-I.; Valley, N.; Freeman, R. G.; Natan, M. J.; Schatz, G. C.; Van Duyne, R. P., Structure Enhancement Factor Relationships in Single Gold Nanoantennas by Surface-Enhanced Raman Excitation Spectroscopy. *J. Am. Chem. Soc.* **2012**, *135*, 301-308.
66. Hao, E.; Schatz, G. C., Electromagnetic Fields around Silver Nanoparticles and Dimers. *The Journal of Chemical Physics* **2004**, *120*, 357-366.
67. Porter, M. D.; Lipert, R. J.; Siperko, L. M.; Wang, G.; Narayanan, R., Sers as a Bioassay Platform: Fundamentals, Design, and Applications. *Chem. Soc. Rev.* **2008**, *37*, 1001-1011.
68. Hudson, S.; Chumanov, G., Bioanalytical Applications of Sers (Surface-Enhanced Raman Spectroscopy). *Anal. Bioanal. Chem.* **2009**, *394*, 679-686.
69. Lee, D.; Lee, S.; Seong, G. H.; Choo, J.; Lee, E. K.; Gweon, D. G., Quantitative Analysis of Methyl Parathion Pesticides in a Polydimethylsiloxane Microfluidic Channel Using Confocal Surface-Enhanced Raman Spectroscopy. *Applied Spect.* **2006**, *60*, 373-377.
70. De Jesús, M. A.; Giesfeldt, K. S.; Sepaniak, M. J., Improving the Analytical Figures of Merit of Sers for the Analysis of Model Environmental Pollutants. *J. Raman Spect.* **2004**, *35*, 895-904.
71. Sharma, B.; Fernanda Cardinal, M.; Kleinman, S. L.; Greeneltch, N. G.; Frontiera, R. R.; Blaber, M. G.; Schatz, G. C.; Van Duyne, R. P., High-Performance Sers Substrates: Advances and Challenges. *MRS Bulletin* **2013**, *38*, 615-624.
72. Betz, J. F.; Yu, W. W.; Cheng, Y.; White, I. M.; Rubloff, G. W., Simple Sers Substrates: Powerful, Portable, and Full of Potential. *Phys. Chem. Chem. Phys.* **2014**, *16*, 2224-2239.
73. Zhang, X.; Yonzon, C. R.; Van Duyne, R. P., An Electrochemical Surface-Enhanced Raman Spectroscopy Approach to Anthrax Detection. *Proc. SPIE* **2003**, *5221*, 82-91.
74. Cai, W. B.; Ren, B.; Li, X. Q.; She, C. X.; Liu, F. M.; Cai, X. W.; Tian, Z. Q., Investigation of Surface-Enhanced Raman Scattering from Platinum Electrodes Using a Confocal Raman Microscope: Dependence of Surface Roughening Pretreatment. *Surf. Sci.* **1998**, *406*, 9-22.
75. Abdelsalam, M. E.; Bartlett, P. N.; Baumberg, J. J.; Cintra, S.; Kelf, T. A.; Russell, A. E., Electrochemical Sers at a Structured Gold Surface. *Electrochemistry Communications* **2005**, *7*, 740-744.
76. Leung, L. W. H.; Weaver, M. J., Extending Surface-Enhanced Raman Spectroscopy to Transition-Metal Surfaces: Carbon Monoxide Adsorption and Electrooxidation on Platinum- and Palladium-Coated Gold Electrodes. *J. Am. Chem. Soc.* **1987**, *109*, 5113-5119.
77. Tian, Z.-Q.; Ren, B.; Wu, D.-Y., Surface-Enhanced Raman Scattering: From Noble to Transition Metals and from Rough Surfaces to Ordered Nanostructures. *The Journal of Physical Chemistry B* **2002**, *106*, 9463-9483.

78. Natan, M. J., Concluding Remarks Surface Enhanced Raman Scattering. *Farad. Disc.* **2006**, *132*, 321-328.
79. Fujiwara, K.; Watarai, H.; Itoh, H.; Nakahama, E.; Ogawa, N., Measurement of Antibody Binding to Protein Immobilized on Gold Nanoparticles by Localized Surface Plasmon Spectroscopy. *Anal. Bioanal. Chem.* **2006**, *386*, 639-644.
80. An, J.-H.; El-Said, W. A.; Yea, C.-H.; Kim, T.-H.; Choi, J.-W., Surface-Enhanced Raman Scattering of Dopamine on Self-Assembled Gold Nanoparticles. *J. Nanosci. Nanotech.* **2011**, *11*, 4424-4429.
81. Farcau, C.; Sangeetha, N. M.; Decorde, N.; Astilean, S.; Ressier, L., Microarrays of Gold Nanoparticle Clusters Fabricated by Stop&Go Convective Self-Assembly for Sers-Based Sensor Chips. *Nanoscale* **2012**, *4*, 7870-7877.
82. Thacker, V. V.; Herrmann, L. O.; Sigle, D. O.; Zhang, T.; Liedl, T.; Baumberg, J. J.; Keyser, U. F., DNA Origami Based Assembly of Gold Nanoparticle Dimers for Surface-Enhanced Raman Scattering. *Nat Commun* **2014**, *5*.
83. Wang, H.; Levin, C. S.; Halas, N. J., Nanosphere Arrays with Controlled Sub-10-Nm Gaps as Surface-Enhanced Raman Spectroscopy Substrates. *J. Am. Chem. Soc.* **2005**, *127*, 14992-14993.
84. Grabar, K. C.; Freeman, R. G.; Hommer, M. B.; Natan, M. J., Preparation and Characterization of Au Colloid Monolayers. *Anal. Chem.* **1995**, *67*, 735-43.
85. Freeman, R. G., et al., Self-Assembled Metal Colloid Monolayers: An Approach to Sers Substrates. *Science* **1995**, *267*, 1629-1632.
86. Grabar, K. C.; Smith, P. C.; Musick, M. D.; Davis, J. A.; Walter, D. G.; Jackson, M. A.; Guthrie, A. P.; Natan, M. J., Kinetic Control of Interparticle Spacing in Au Colloid-Based Surfaces: Rational Nanometer-Scale Architecture. *J. Am. Chem. Soc.* **1996**, *118*, 1148-1153.
87. Yonzon, C. R.; Stuart, D. A.; Zhang, X.; McFarland, A. D.; Haynes, C. L.; Van Duyne, R. P., Towards Advanced Chemical and Biological Nanosensors - an Overview. *Talanta* **2005**, *67*, 438-448.
88. Hulteen, J. C.; Van Duyne, R. P., Nanosphere Lithography: A Materials General Fabrication Process for Periodic Particle Array Surfaces. *J. Vac. Sci. Tech. A* **1995**, *13*, 1553-1558.
89. Haynes, C. L.; Haes, A. J.; Van Duyne, R. P., Nanosphere Lithography: Synthesis and Application of Nanoparticles with Inherently Anisotropic Structures and Surface Chemistry. *Mat. Res. Soc. Symp. Proc.* **2001**, *635*, C6.3/1-C6.3/6.
90. Dieringer, J. A.; McFarland, A. D.; Shah, N. C.; Stuart, D. A.; Whitney, A. V.; Yonzon, C. R.; Young, M. A.; Zhang, X.; Van Duyne, R. P., Surface Enhanced Raman Spectroscopy: New Materials, Concepts, Characterization Tools, and Applications. *Farad. Disc.* **2006**, *132*, 9-26.
91. McFarland, A. D.; Young, M. A.; Dieringer, J. A.; VanDuyne, R. P., Wavelength-Scanned Surface-Enhanced Raman Excitation Spectroscopy. *J. Phys. Chem. B* **2005**, *109*, 11279-11285.
92. Haes, A. J.; Van Duyne, R. P., A Nanoscale Optical Biosensor: Sensitivity and Selectivity of an Approach Based on the Localized Surface Plasmon Resonance Spectroscopy of Triangular Silver Nanoparticles. *J. Am. Chem. Soc.* **2002**, *124*, 10596 - 10604.
93. Haes, A. J.; Van Duyne, R. P., A Highly Sensitive and Selective Surface-Enhanced Nanobiosensor. *Mat. Res. Soc. Symp. Proc.* **2002**, *723*, O3.1.1-O3.1.6.
94. Gunnarsson, L.; Bjerneld, E. J.; Xu, H.; Petronis, S.; Kasemo, B.; Kall, M., Interparticle Coupling Effects in Nanofabricated Substrates for Surface-Enhanced Raman Scattering. *Appl. Phys. Lett.* **2001**, *78*, 802-804.
95. Marquestaut, N.; Martin, A.; Talaga, D.; Servant, L.; Ravaine, S.; Reculusa, S.; Bassani, D. M.; Gillies, E.; Lagugné-Labarthet, F., Raman Enhancement of Azobenzene Monolayers on Substrates Prepared by Langmuir−Blodgett Deposition and Electron-Beam Lithography Techniques. *Langmuir* **2008**, *24*, 11313-11321.

96. Im, H.; Bantz, K. C.; Lindquist, N. C.; Haynes, C. L.; Oh, S.-H., Vertically Oriented Sub-10-Nm Plasmonic Nanogap Arrays. *Nano Lett.* **2010**, *10*, 2231-2236.
97. Abu Hatab, N. A.; Oran, J. M.; Sepaniak, M. J., Surface-Enhanced Raman Spectroscopy Substrates Created Via Electron Beam Lithography and Nanotransfer Printing. *ACS Nano* **2008**, *2*, 377-385.
98. Kahl, M.; Voges, E.; Kostrewa, S.; Viets, C.; Hill, W., Periodically Structured Metallic Substrates for Sers. *Sens. Actuators, B* **1998**, *51*, 285-291.
99. Roca, M.; Haes, A. J., Silica-Void-Gold Nanoparticles: Temporally Stable Surface-Enhanced Raman Scattering Substrates. *J. Am. Chem. Soc.* **2008**, *130*, 14273-14279.
100. Sun, Y. G.; Xia, Y. N., Shape-Controlled Synthesis of Gold and Silver Nanoparticles. *Science* **2002**, *298*, 2176-2179.
101. Ahmadi, T. S.; Wang, Z. L.; Green, T. C.; Henglein, A.; El-Sayed, M. A., Shape-Controlled Synthesis of Colloidal Platinum Nanoparticles. *Science* **1996**, *272*, 1924-1925.
102. Murphy, C. J.; Jana, N. R., Controlling the Aspect Ratio of Inorganic Nanorods and Nanowires. *Adv. Mat.* **2002**, *14*, 80-82.
103. Smith, D. K.; Miller, N. R.; Korgel, B. A., Iodine in Ctab Prevents Gold Nanorod Formation. *Langmuir* **2009**, *2009*, 9518-9524.
104. Mulvihill, M. J.; Ling, X. Y.; Henzie, J.; Yang, P., Anisotropic Etching of Silver Nanoparticles for Plasmonic Structures Capable of Single-Particle Sers. *J. Am. Chem. Soc.* **2009**, *132*, 268-274.
105. Moran, C. H.; Rycenga, M.; Zhang, Q.; Xia, Y., Replacement of Poly(Vinyl Pyrrolidone) by Thiols: A Systematic Study of Ag Nanocube Functionalization by Surface-Enhanced Raman Scattering. *The Journal of Physical Chemistry C* **2011**, *115*, 21852-21857.
106. Lal, S.; Grady, N. K.; Kundu, J.; Levin, C. S.; Lassiter, J. B.; Halas, N. J., Tailoring Plasmonic Substrates for Surface Enhanced Spectroscopies. *Chem. Soc. Rev.* **2008**, *37*, 898-911.
107. Lee, K.-S.; El-Sayed, M. A., Gold and Silver Nanoparticles in Sensing and Imaging: Sensitivity of Plasmon Response to Size, Shape, and Metal Composition. *The Journal of Physical Chemistry B* **2006**, *110*, 19220-19225.
108. Huang, X.; Neretina, S.; El-Sayed, M. A., Gold Nanorods: From Synthesis and Properties to Biological and Biomedical Applications. *Adv. Mat.* **2009**, *21*, 4880-4910.
109. Mahmoud, M. A.; El-Sayed, M. A., Different Plasmon Sensing Behavior of Silver and Gold Nanorods. *The Journal of Physical Chemistry Letters* **2013**, *4*, 1541-1545.
110. Murphy, C. J.; Thompson, L. B.; Alkilany, A. M.; Sisco, P. N.; Boulos, S. P.; Sivapalan, S. T.; Yang, J. A.; Chernak, D. J.; Huang, J., The Many Faces of Gold Nanorods. *The Journal of Physical Chemistry Letters* **2010**, *1*, 2867-2875.
111. Lohse, S. E.; Murphy, C. J., The Quest for Shape Control: A History of Gold Nanorod Synthesis. *Chem. Mater.* **2013**, *25*, 1250-1261.
112. Murphy, C. J.; Gole, A. M.; Hunyadi, S. E.; Stone, J. W.; Sisco, P. N.; Alkilany, A.; Kinard, B. E.; Hankins, P., Chemical Sensing and Imaging with Metallic Nanorods. *Chemical Communications* **2008**, 544-557.
113. Heck, K. N.; Janesko, B. G.; Scuseria, G. E.; Halas, N. J.; Wong, M. S., Observing Metal-Catalyzed Chemical Reactions in Situ Using Surface-Enhanced Raman Spectroscopy on Pd−Au Nanoshells. *J. Am. Chem. Soc.* **2008**, *130*, 16592-16600.
114. Li, W.; Camargo, P. H. C.; Lu, X.; Xia, Y., Dimers of Silver Nanospheres: Facile Synthesis and Their Use as Hot Spots for Surface-Enhanced Raman Scattering Doi:10.1021/Nl803621x. *Nano Lett.* **2009**, *9*, 485-490.
115. Kleinman, S. L.; Frontiera, R. R.; Henry, A.-I.; Dieringer, J. A.; Van Duyne, R. P., Creating, Characterizing, and Controlling Chemistry with Sers Hot Spots. *Phys. Chem. Chem. Phys.* **2013**, *15*, 21-36.
116. Tantra, R.; Brown, R. J. C.; Milton, M. J. T., Strategy to Improve the Reproducibility of Colloidal Sers. *J. Raman Spect.* **2007**, *38*, 1469-1479.

117. Bell, S. E. J.; Sirimuthu, N. M. S., Rapid, Quantitative Analysis of Ppm/Ppb Nicotine Using Surface-Enhanced Raman Scattering from Polymer-Encapsulated Ag Nanoparticles (Gel-Colls). *Analyst* **2004**, *129*, 1032-1036.
118. Faulds, K.; Smith, W. E.; Graham, D.; Lacey, R. J., Assessment of Silver and Gold Substrates for the Detection of Amphetamine Sulfate by Surface Enhanced Raman Scattering (Sers). *Analyst* **2002**, *127*, 282-286.
119. Kneipp, K.; Kneipp, H.; Itzkan, I.; Dasari, R. R.; Feld, M. S., Ultrasensitive Chemical Analysis by Raman Spectroscopy. *Chemical Reviews* **1999**, *99*, 2957-2976.
120. DeLong, R. K.; Reynolds, C. M.; Malcolm, Y.; Schaeffer, A.; Severs, T.; Wanekaya, A., Functionalized Gold Nanoparticles for the Binding, Stabilization, and Delivery of Therapeutic DNA, Rna, and Other Biological Macromolecules. *Nanotechnology, Science and Applications* **2010**, *3*, 53-63.
121. Lee, S.; Anderson, L. J. E.; Payne, C. M.; Hafner, J. H., Structural Transition in the Surfactant Layer That Surrounds Gold Nanorods as Observed by Analytical Surface-Enhanced Raman Spectroscopy. *Langmuir* **2011**, *27*, 14748-14756.
122. Jana, N. R.; Gearheart, L.; Murphy, C. J., Wet Chemical Synthesis of High Aspect Ratio Cylindrical Gold Nanorods. *J. Phys. Chem. B* **2001**, *105*, 4065-4067.
123. Niidome, T.; Yamagata, M.; Okamoto, Y.; Akiyama, Y.; Takahashi, H.; Kawano, T.; Katayama, Y.; Niidome, Y., Peg-Modified Gold Nanorods with a Stealth Character for in Vivo Applications. *Journal of Controlled Release* **2006**, *114*, 343-347.
124. Neouze, M.-A.; Schubert, U., Surface Modification and Functionalization of Metal and Metal Oxide Nanoparticles by Organic Ligands. *Monatsh Chem* **2008**, *139*, 183-195.
125. Liz-Marzan, L. M.; Mulvaney, P., The Assembly of Coated Nanocrystal. *J. Phys. Chem. B* **2003**, *107*, 7312-7326.
126. Liz-Marzan, L. M.; Giersig, M.; Mulvaney, P., Synthesis of Nanosized Gold-Silica Core-Shell Particles. *Langmuir* **1996**, *12*, 4329-4335.
127. Radloff, C.; Halas, N. J., Enhanced Thermal Stability of Silica-Encapsulated Metal Nanoshells. *Appl. Phys. Lett.* **2001**, *79*, 674-676.
128. Chen, Y.-S.; Frey, W.; Kim, S.; Homan, K.; Kruizinga, P.; Sokolov, K.; Emelianov, S., Enhanced Thermal Stability of Silica-Coated  Gold Nanorods for Photoacoustic Imaging and Image-Guided Therapy. *Opt. Express* **2010**, *18*, 8867-8878.
129. Zhan, Q. Q., J.; Li, Xin.; He, S., A Study of Mesoporous Silica-Encapsulated Gold Nanorods as Enhanced Light Scattering
Probes for Cancer Cell Imaging. *Nanotech.* **2010**, *21*, 12pp.
130. Marie Carmelle S. Pierre; Haes, A. J., Purification Implications on Sers Activity of Silica Coated Gold Nanospheres. *Anal. Chem.* **2012**, *84*, 7906-7911.
131. Mulvaney, S. P.; Musick, M. D.; Keating, C. D.; Natan, M. J., Glass-Coated, Analyte-Tagged Nanoparticles: A New Tagging System Based on Detection with Surface-Enhanced Raman Scattering. *Langmuir* **2003**, *19*, 4784-4790.
132. Doering, W. E.; Nie, S., Spectroscopic Tags Using Dye-Embedded Nanoparticles and Surface-Enhanced Raman Scattering. *Anal. Chem.* **2003**, *75*, 6171-6176.
133. Hu, Y.; Zhang, Q.; Goebl, J.; Zhang, T.; Yin, Y., Control over the Permeation of Silica Nanoshells by Surface-Protected Etching with Water. *Phys. Chem. Chem. Phys.* **2010**, *12*, 11836-11842.
134. Zhang, Q.; Zhang, T.; Ge, J.; Yin, Y., Permeable Silica Shell through Surface-Protected Etching. *Nano Lett.* **2008**, *8*, 2867-2871.

CHAPTER 2 IMPROVING QUALITY CONTROL OF SILICA COATED GOLD NANOSPHERES USING POST-SYNTHETIC COLUMN PURIFICATION

2.1 Introduction

Noble metal nanostructures exhibit novel size dependent chemical and physical properties that warrant their use in many applications such as catalysis,[1] drug delivary,[2] optical sensing,[3] and surface-enhanced Raman spectroscopy.[4-6] In many of the above applications, the optical properties of metal nanostructures are of the utmost importance. The optical properties of gold nanostructures exhibit unique extinction (absorption and scattering) spectra which arise from their localized surface plasmon resonance (LSPR). For instance, the LSPR allows for SERS signal enhancement of adsorbed molecules by 2-9 orders of magnitude, thereby facilitating molecular detection at biologically relevant concentrations.[7] Improvements over size homogeneity of gold nanoparticles is important for LSPR and therefore its application in various scientific studies systematic study of nanoparticle structure-function relationships.[8]

Specifically, the extinction coefficient of gold nanoparticles is a size dependent property. Haiss and coworkers both theoretically and experimentally determined the extinction coefficients of gold nanoparticles with diameters ranging from 3 to 120 nm. The extinction coefficient for a 12 nm diameter gold nanoparticle at $\lambda = 450$ nm is reported as 1.1×10^{8} $M^{-1}\bullet cm^{-1}$.[9] Assuming a 10% standard deviation in gold nanoparticle diameter (i.e. ± 1 nm), the extinction coefficients at $\lambda = 450$ nm for a 13 nm gold nanoparticles increases to 1.4×10^{8} $M^{-1}\bullet cm^{-1}$, whereas the extinction coefficient for a 11

nm particle decreases to 0.8×10^{8} $M^{-1}\bullet cm^{-1}$.[9] Therefore, the extinction coefficient for a 12 ± 1 nm (10% RSD) gold nanoparticle sample is $1.1 \pm 0.3\times10^{8}$ $M^{-1}\bullet cm^{-1}$ (27% RSD). This indicates that a 10% relative standard deviation in gold nanoparticle size distribution corresponds to a 27% relative standard deviation in extinction coefficient and therefore, small variation in gold nanoparticle size can have huge impact in nanoparticle optical properties. It is calculated that a 10% RSD in extinction coefficient corresponds to a 3.4% RSD in gold nanoparticle size.

Bottom-up synthetic procedures are commonly varied to improve nanoparticle monodispersity,[10-11] yet most of these methods still result in heterogeneous nanoparticles with higher than 10% RSD in diameter. Size heterogeneity leads to variations in chemical and physical properties of solution-phase nanoparticles, thereby, limiting application reproducibility.[12] As a result, post-synthetic purification approaches such as centrifugation,[13-15] diafiltration,[16] ion exchange,[12] or size exclusion chromatography (SEC)[17-20] are implemented to improve nanoparticle shape and size homogeneity. For example Fu-Ken Liu used SEC to successfully separate gold nanoparticles ranging from 12.1 to 79.1 nm using sodium dodecyl sulfate as a mobile phase additive in SEC; however, sodium dodecyl sulfate (or other surfactants like CTAB) bind irreversibly on gold nanoparticle surface,[21-22] thereby, influencing most surface-chemistry sensitive techniques such as SERS[23] and CE.

Another example relating gold nanoparticle size-function relationship is reported by Wu and coworkers.[24] The authors found that the optimal pH required for functionalizing 16 nm gold nanoparticles with hepatitis B specific mouse antibody was 7.36 vs. 8.71 for a 14 nm particle. Hence, a decrease in gold nanoparticle size by 12.5%

relates to pH increase by 1.35 for optimal antibody functionalization process. These examples warrant that gold nanoparticle size and/or shape morphologies are important for nanoparticle related applications; therefore, require post-synthetic purification technique for nanoparticle shape/size morphology.

Herein, silica coated gold nanospheres are fractionated based on size using surfactant-free SEC. Silica encapsulation of gold nanoparticles not only stabilizes the gold cores [12] but also minimizes any non-specific interactions that is vital for SEC fractionation. [25] The SEC column packed with a super-fine Sephacryl S1000 stationary phase has size exclusion limit of 11 - 400 nm and can fractionate gold nanoparticles based on thermodynamic partitioning between the stationary pores and the bulk mobile phase. Non-specific interactions (hydrophobic and electrostatic) are minimized to allow entropy controlled SEC fractionation of gold nanoparticles.[26]

2.2 Experimental Materials and Methods

2.2.1 Chemical Reagents

Gold(III) chloride trihydrate, sodium citrate dihydrate, Amberlite MB-150 mixed bed exchange resin, (3-aminopropyl) trimethoxysilane (APTMS), sodium chloride (NaCl), sodium trisilicate (27%), tetraethyl orthosilicate (TEOS), silver perchlorate, sodium borohydride, and hydroxylamine hydrochloride were purchased from Sigma. Ethanol, ammonium hydroxide (NH_4OH), hydrochloric acid (HCl), and nitric acid (HNO_3) were purchased from Fisher Scientific (Pittsburgh, PA). Ultrapure water (18.2 $M\Omega\ cm^{-1}$) was obtained from a Barnstead Nanopure System and used for all experiments. All glassware items were cleaned with aqua regia (3:1 HCl/ HNO_3) and rinsed thoroughly with water,

and oven (glass) or air (plastic) dried overnight before use.

2.2.2 Gold Nanoparticle and Silica Coated Au Nanoparticle Synthesis

Gold nanoparticles (d = ~12 nm) were synthesized using a well-established citrate reduction techniques. [10] Gold nanoparticles with three different silica shell thicknesses were synthesized by modifying the sodium silicate concentration during silica growth. [12, 27] Synthesized silica coated gold ($Au@SiO_2$) nanoparticle samples were washed in ethanol and water using centrifugation at 12,280 ×g for 45 minutes. $Au@SiO_2$ nanoparticles were further purified using Sephadex G50 anion exchange chromatography to remove uncoated nanoparticles. [12] The concentration of all nanoparticle samples was calculated [9] at λ_{max} using an extinction coefficient of 2×10^8 $M^{-1} \bullet cm^{-1}$ for ~12 nm gold nanoparticles.

2.2.3 Silica-Coated Au Nanoparticles Fractionation Using Size Exclusion Chromatography

$Au@SiO_2$ nanoparticle samples were fractionated with a 30 cm × 0.9 cm SEC column packed with Sephacryl S-1000 resin. 10 mM Tris buffer (pH 9.0) with isopropanol as organic additive was used as an eluent buffer. First the required packing volume was calculated and 130% packing volume of Sephacryl S-1000 was allocated for the column packing process. The stationary matrix was re-suspended in SEC buffer such that the matrix was 70% of the slurry. The slurry was then poured down the column and allowed to pack under gravity. After the packing matrix settled, buffer inlet line was connected to the top of the column matrix was washed with 3 column volumes of eluent buffer using ultra flow meter at 0.5 mL/min. GE frac-950 fraction collector was

programed and connected at the end of the sephacryl column to collect eluted nanoparticles automatically throughout the fractionation process. Au@SiO_2 nanoparticles were concentrated and re-suspended in elution buffer before column loading. 50 µL of 100 nM Au@SiO_2 nanoparticle samples were loaded and once the sample entered the column bed, 1 mL of elution buffer was then added to prevent column bed drying. SEC column was sealed immediately with eluent buffer inlet and nanoparticles were fractionated at 0.3 mL/min flow rate. Eluted samples were collected at 0.2 mL/fraction with an auto fraction collector. The pH of the collected fractions was adjusted to ~7.0 by adding 15 µL of 0.1 M HCl to prevent silica dissolution at pH 9.0.

2.2.4 Extinction Spectroscopy

Localized surface plasmon resonance (LSPR) spectra were collected using a 1.0 cm path length disposable methacrylate cuvette and an ultraviolet-visible (UV-vis) spectrometer (Ocean Optics USB4000). For SEC experiment, inline UV-vis detection using 1 cm z-flow cell was used. LSPR spectra were collected every 20 second intervals for 1 hour. The following parameters were used during data collections: integration time = 60 msec, average = 25 scans, and boxcar = 10. Extinction maximum wavelengths (λ_{max}) were determined from the zero-point crossing of the first derivative of each spectrum using MatLab (MathWorks).

2.2.5 Transmission Electron Microscopy (TEM)

TEM was performed using a JEOL JEM-1230 microscope equipped with a Gatan CCD camera. Samples were prepared on 400 mesh copper grids that were coated with a thin film of Formvar and carbon (Ted Pella). The nanoparticle solution was diluted in a 50% water−ethanol mixture. The solution (~10 µL) was pipetted onto a grid and dried.

Over 200 nanoparticles were analyzed using Image Pro Analyzer to estimate the average diameter of the nanoparticle.

2.3 Results and Discussion

Sol gel chemistry, a simple and cost effective method for encapsulating gold nanoparticles in silica,[28] occurs in three steps: nucleation of silica on the surface of gold, followed by growth via hydrolysis, and condensation reactions.[28-29] Reaction temperature, silica precursor concentration[30] and solubility[31], solution pH[28, 31] and ionic strength, and time[30] influence the resulting silica morphology on gold nanoparticle surfaces. While controlling solution parameters improve Au@SiO_2 nanoparticle diameter homogeneity by promoting silica nucleation followed by diffusion-limited growth;[32] typical sol-gel reactions yield heterogeneously condensed silica on gold nanoparticle surfaces (i.e. greater than 10% RSD in diameter).[12, 29-30, 33] Structural differences in the dielectric material on Au@SiO_2 nanoparticle surfaces lead to variations in the chemical and physical properties[29, 34] and consequently, limits application reproducibility.[12, 35]

2.3.1 Silica Coated Au Nanoparticle Size Heterogeneity

To evaluate how silica shell uniformity (or lack of uniformity) is influenced by silica shell thickness, solution-phase Au@SiO_2 nanoparticle samples with the same gold core but varying silica shell thicknesses are synthesized in two steps. First, gold cores are synthesized using standard citrate reduction methods[36] and characterized using TEM (Figure 2.1A). The spherical gold nanoparticles exhibit an average core diameter of 12.7 ± 1.3 nm (10% RSD, number of particles (N) = 355). Gold nanoparticles synthesized for silica coating itself are heterogeneous as shown in Figure 2.1D (i.e. 99.7% of gold nanoparticle diameters range from 10 to 15 nm (±3σ)) and at least some heterogeneity is

expected for solution-phase nanoparticles synthesized using homogeneous nucleation and growth techniques.[37-39] Small heterogeneity in gold nanoparticle will influence the

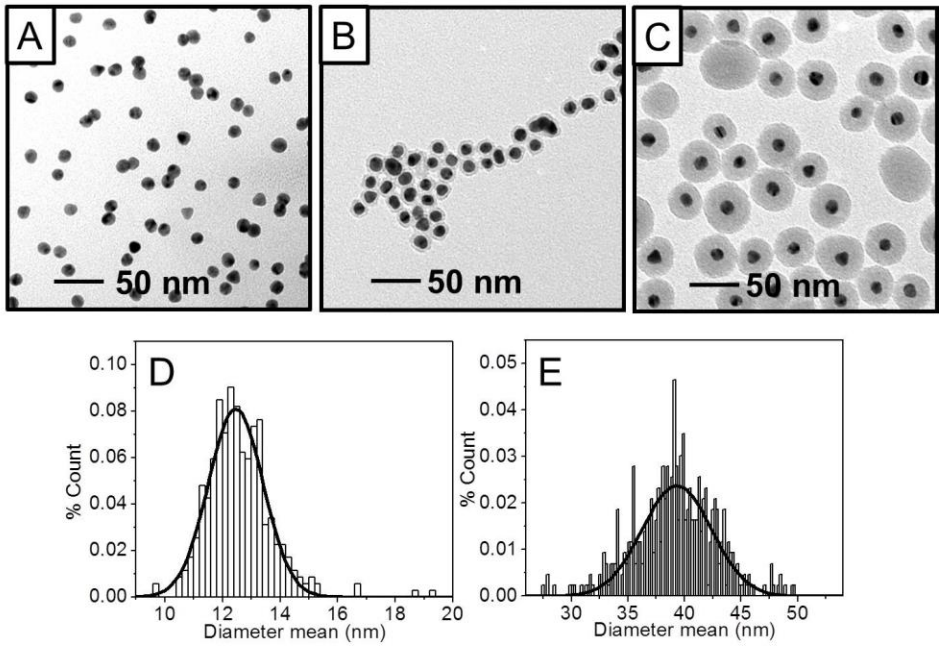

Figure 2.1. TEM images of gold (A) and silica coated gold nanoparticles synthesized using 0.60 mM (B) and 0.90 mM (C) sodium silicate during silica growth. The mean diameter of synthesized nanoparticles are (A) 12.7 ± 1.3 nm (10% RSD, N = 355), (B) 20.1 ± 2.1 nm (10% RSD, N = 118, and (C) 39.7 ± 3.9 nm (10% RSD, N = 430). Diameter distribution of (D) Au nanoparticles and (E) 39.7 nm Au@SiO_2 nanoparticles show broad distribution curves. 99.7% of Au and Au@SiO_2 nanoparticles range from 10 – 15 nm (± 3σ) and 30 – 50 nm (± 3σ) and confirm the hypothesis that bottom-up synthesis of solution-phase nanoparticles generates heterogeneous nanoparticle distribution.

resulting nanoparticle plasmonic properties. For example, the LSPR maximum wavelength of gold nanoparticles with diameters ranging from 10 – 20 nm is centered at ~520 nm and largely insensitive to small variations in nanoparticle diameter (±10% RSD).[40-43] A 10% increase (i.e. 10.0 to 11.0 nm) in nanoparticle diameter, however, causes the extinction coefficient of the nanostructures to increase by ~22%.[9]

Consequently, slight variations in gold nanoparticle diameters can reduce the ability of estimating nanoparticle concentration correctly from extinction measurements using the nanoparticle extinction coefficient for a fixed size.

The size heterogeneity of a nanoparticle sample further increases upon silica condensation. Silica condensation on gold nanoparticle cores using a modified Stöber method,[29-30] utilizes base catalyzed reaction of two silica monomers (APTMS and TEOS) and sodium silicate at room temperature. During silica condensation process, any error in calculating gold nanoparticle size and/or concentration can lead to additional nanoparticle heterogeneity. Resulting TEM image of $Au@SiO_2$ nanoparticles synthesized using various concentrations of sodium silicate are shown in Figure 2.1B – C. These synthesized $Au@SiO_2$ nanoparticles exhibit average diameters of 20.1 ± 2.1 nm (10% RSD, N = 118) and 39.7 ± 3.9 nm (10% RSD, N = 430), respectively. As the sodium silicate concentration during silica synthesis increases (0.60 to 0.90 mM), the resulting silica thickness also increases which is consistent with reported literature.[12] Gaussian curves used to evaluate $Au@SiO_2$ nanoparticle diameter distribution (d = 39.7 nm) indicate that 99.7% of Au and $Au@SiO_2$ nanoparticles range from 30 – 50 nm (± 3σ) as shown in Figure 2.1E. Clearly, the diameter distribution of $Au@SiO_2$ nanoparticles increases after silica coating. This is expected given the diameter variations in gold core and also from the inherent inconsistencies in silica hydrolysis and condensation as previously reported.[29-30, 33, 37-38]

2.3.2 SEC Maintains Nanoparticle Optical and Morphological Stability

To evaluate optical and morphological stability of $Au@SiO_2$ nanoparticles, 39.7 nm diameter $Au@SiO_2$ nanoparticles is passed through SEC column. LSPR and TEM images of $Au@SiO_2$ nanoparticles before SEC are obtained. Fractionated $Au@SiO_2$

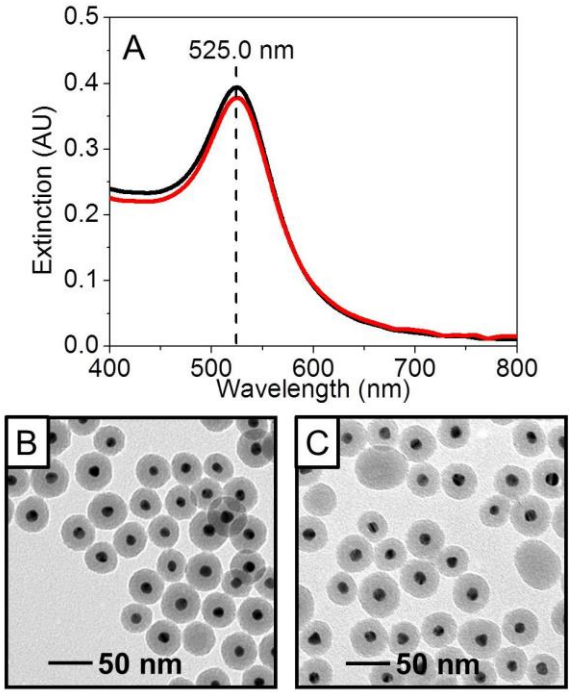

Figure 2.2. Extinction and TEM analysis of $Au@SiO_2$ nanoparticles during SEC purification. (A) LSPR of $Au@SiO_2$ nanoparticles before and after purification. λ_{max} and Γ of sample before SEC are 525.0 nm and 0.38 eV. Similarly, λ_{max} and Γ of sample collected after SEC are 524.8 nm and 0.38 eV respectively indicating that no significant changes in optical property occurs during SEC. Representative TEM analysis of $Au@SiO_2$ nanoparticles before (B) and after (C) indicate no change is shape and size morphologies. Mean diameter calculated from TEM images are (B) 39.7 ± 3.9 nm and (C) 40.6 ± 4.4 nm. No statistical difference between mean diameters is verified using t-test at 95% confidence level. $Au@SiO_2$ nanoparticle fractions are pooled together to collect LSPR and TEM images.

nanoparticles are pooled together and analyzed using LSPR and TEM. Figure 2.2 confirms that the optical property and shape/size morphologies of $Au@SiO_2$ nanoparticles are maintained during the SEC purification. The LSPR spectra indicate that the λ_{max} and Γ values of $Au@SiO_2$ nanoparticles are 525.0 nm and 0.38 eV before SEC; and 524.8 nm and 0.38 eV, after SEC; respectively. No significant variation in optical property of $Au@SiO_2$ nanoparticles is observed. Furthermore, TEM images of $Au@SiO_2$ nanoparticles before and after SEC purifications show that silica shape and size morphologies are maintained throughout the whole process. The mean diameters of $Au@SiO_2$ nanoparticles before passing through SEC column is 39.7 ± 3.9 nm whereas the calculated diameter of $Au@SiO_2$ nanoparticles after passing through SEC is 40.6 ± 4.4 nm. Small difference observed in nanoparticle diameter from TEM analysis is within the standard error as verified using t-test. The t-test at 95% confidence interval showed no statistical difference between $Au@SiO_2$ nanoparticle diameter before and after SEC. Both LSPR and TEM provide encouraging results that SEC purification of $Au@SiO_2$ nanoparticles without any surfactant additive is achievable.

2.3.3 LSPR Wavelength Maximum as a Function of Silica Thickness and Plasmon Coupling

The extinction maximum wavelength ($\lambda_{max, Silica}$) of $Au@SiO_2$ nanoparticles depends on the refractive index and thickness of the silica surrounding the gold core (n_s) as well as the refractive index of the bulk environment and can be described using a one layer refractive index (RI) model.[44-46] The $\lambda_{max, Silica}$ depends on the silica thickness (t_s) as follows:

$$\lambda_{max,\,Silica} = m_1(n_s - n_b)\left(1 - e^{\left(\frac{-2a}{l_d}\right)}\right) - m_2\left[(n_s - n_b)\left(1 - e^{\left(\frac{-2a}{l_d}\right)}\right)\right]^2 + \lambda_{max,\,bulk} \qquad (2.1)$$

where m_1 and m_2 are linear and non-linear RI sensitivities (80 and 160 nm/RIU for ~12 nm Au nanoparticles)[47], n_s is the RI of silica (1.47 RIU)[47], (n_b) is the bulk RI of the SEC buffer (10% isopropanol in water = 1.34 RIU)[48-49], l_d is the characteristic electromagnetic field decay length (5.0 nm)[47], and $\lambda_{max,bulk}$ is the experimentally measured maximum wavelength of 12.7 nm gold nanoparticles in the SEC buffer (521.1 nm). This model assumes: (1) electromagnetic isolation between each gold cores; (2) identical nanoparticles (shape, size, etc.); and (3) the electromagnetic field (E(z)) decays exponentially as the distance from the gold surface (z) increases ($E(z) = \exp(-z/l_d)^2$).[46] While the electric field decay will deviate from this model, the electromagnetic field will decay sharply as the distance from the gold core increases. This suggests that the $\lambda_{max,\,Silica}$ will exhibit non-linear responses as observed in Figure 2.3A for silica coated gold nanoparticles. Initially, the $\lambda_{max,Silica}$ increases as silica shell thickness increases (t_{silica} <8 nm). This response is consistent with an increase in local refractive index near the metal surface within the strong electromagnetic fields. As the silica shell thickness increases beyond 8 nm, $\lambda_{max,Silica}$ value saturates (i.e. $\lambda_{max,Silica}$ red shift <0.1 nm per 1 nm increase in silica thickness). Established RI modeling applied for silica coated Au nanoparticles imply that observed LSPR during in-line detection will show no change in LSPR maxima as long as silica shell thickness is greater than ~ 8nm. Below silica thickness of 8 nm, systematic blue shift in LSPR is expected as Au@SiO_2 nanoparticles diameter decreases at longer elution volumes.

In addition, the optical properties of gold nanoparticle also depend on interparticle electromagnetic coupling dictated by the separation.[50-52] Decreasing the separation distance between the metal cores facilitates LSPR coupling which red-shifts the observed λ_{max}. Previous studies on gold nanoparticle plasmon coupling indicate that the observed λ_{max} shift ($\Delta\lambda_{max}$) decays exponentially as the separation distance increases and is independent of nanoparticle diameter.[51, 53] Jain et. al. used DDA to related the scaled plasmon shift ($\Delta\lambda/\lambda_{max}$) for gold nanoparticles to a ratio of separation distance between nanoparticles and gold nanoparticle diameter (s/d) as follow:[51]

$$\frac{\Delta\lambda}{\lambda_{max}} = A \times e^{\left(\frac{-s/d}{\tau}\right)} \tag{2.2}$$

where A is the pre-exponential factor (0.08) and τ is the exponential decay constant (0.21) of $\Delta\lambda/\lambda_{max}$ as a function of s/d. This exponential equation can be used to estimate electromagnetic coupling between two gold nanoparticles encapsulated in silica shells.[50-51] Theoretical plot of LSPR wavelength shift as a function of separation distance between two Au nanoparticles using equation 2.2 is represented in Figure 2.3B. The plot shows that electromagnetic coupling causes LSPR red shift >1 nm as separation distance decreases below 12 nm. It is also observed that the LSPR red shift increases sharply below separation distances of 5 nm. Finally, modified equation 2.3 allows estimation of $\lambda_{max,\ Coupled}$ values of electromagnetically coupled Au@SiO_2 nanoparticles assuming that silica shells are touching edge to edge:

$$\lambda_{max,\ Coupled} = \lambda_{max,\ Silica}\left(1 + A \times e^{\left(\frac{-s/d}{\tau}\right)}\right) \tag{2.3}$$

where $\lambda_{max,\ Silica}$ is the wavelength maximum of uncoupled Au@SiO_2 nanoparticles in SEC solvent (10% isopropanol in water), s is the edge to edge separation distance

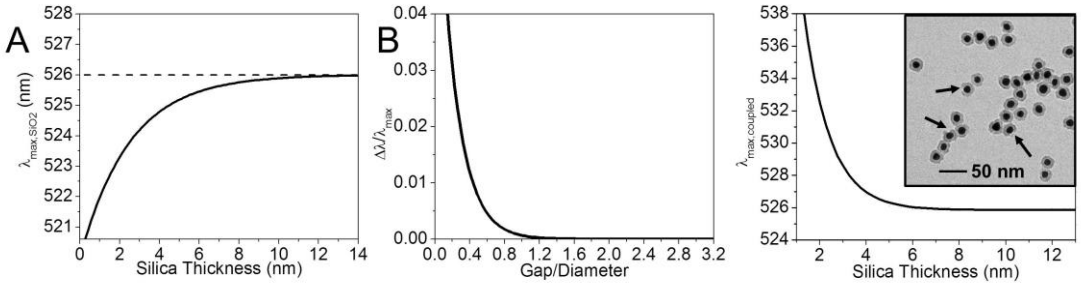

Figure 2.3. (A) Theoretical plot of $\lambda_{max,silica}$ *vs.* silica thickness during SEC using 10% isopropanol as bulk (RI 1.34). $\lambda_{max,silica}$ red shifts as silica shell thickness increases. For silica thickness <8 nm, significant decrease in $\lambda_{max,silica}$ as a function of decreasing silica thickness is observed. Beyond 8 nm silica thickness, $\lambda_{max,silica}$ values saturate at 525.9 nm. (B) Theoretical plot of LSPR wavelength shift as a function of nanoparticle plasmon coupling for ~12 nm Au nanoparticles. As gap distances between two 12 nm Au nanoparticles decreases below 9 nm, LSPR red shift of >1 nm is expected which increases sharply for gap distances <5 nm. (C) Expected $\lambda_{max,\ Coupled}$ as a function of silica shell thickness plotting for two Au@SiO_2 nanoparticles touching edge-edge through silica. Plot shows that as silica thickness increases, LSPR shift of coupled nanoparticle decreases exponentially and stabilizes above 6 nm. Inset shows TEM image of 23.4 ± 2.6 nm (11% RSD) Au@SiO2 nanoparticles with silica defects (partially or uncoated) shown with black arrows.

between two gold nanoparticle cores (2×Silica thickness), and d is the diameter of gold nanoparticle core (12.7 nm). Figure 2.3C shows the semi-empirical result that the LSPR wavelength maximum from gold nanoparticles will increase exponentially as silica shell thickness decreases. When the silica shell thickness is greater than 6 nm (for a total separation distance of 12 nm edge to edge), no significant electromagnetic coupling is expected.

Variation in silica shell thickness is a result of inherent inconsistencies in silica

hydrolysis and condensation during silica sol-gel synthesis. As shown in the TEM image (inset Figure 2.3C), $Au@SiO_2$ nanoparticles contain structural defects in the silica morphology which could also impact the electromagnetic coupling and average separation distance between nanoparticles in solution. The synthesized $Au@SiO_2$ nanoparticles exhibit average diameters of 23.4 ± 2.6 nm (11% RSD, N = 146). Assuming that variations in these total diameters arise primarily from the silica shell variations (not gold core diameters), the average silica shells are 4.3 - 6.7 nm. Considering the previously described electromagnetic coupling model, $Au@SiO_2$ nanoparticles with shell thickness less than ~ 6 nm can electromagnetically couple during SEC; thereby increasing LSPR maxima above 526 nm compared to isolated $Au@SiO_2$ nanoparticles. As a result, LSPR of $Au@SiO_2$ nanoparticle sample observed using in-line detection during SEC will be influenced not only by the silica shell thickness but also the electromagnetic coupling between nanoparticles specially when silica separation distance is <12 nm.

2.3.4 SEC Separation of Silica Coated Nanoparticles

Ideal SEC separates particles based on size where the solute distribution between the mobile and the stationary phase is controlled by entropy alone. The enthalpy term is assumed negligible when the enthalphic contribution on particle separation arising from hydrophobic/hydrophilic or electrostatic interactions is minimized. In this case, the free energy of separation is approximated by entropy term and the SEC equilibrium constant can be written as $K_{SEC} = \exp(\Delta S°/R)$. The entropy S, determines the number of equally probable states a particle can access inside the matrix pores larger in size. Because smaller diameter particles can occupy more number of probable states inside matrix pores

than larger diameter particles, smaller particles is retained longer and elute after larger particles. Figure 2.4. shows ideal SEC separation of $Au@SiO_2$ nanoparticles that differ in

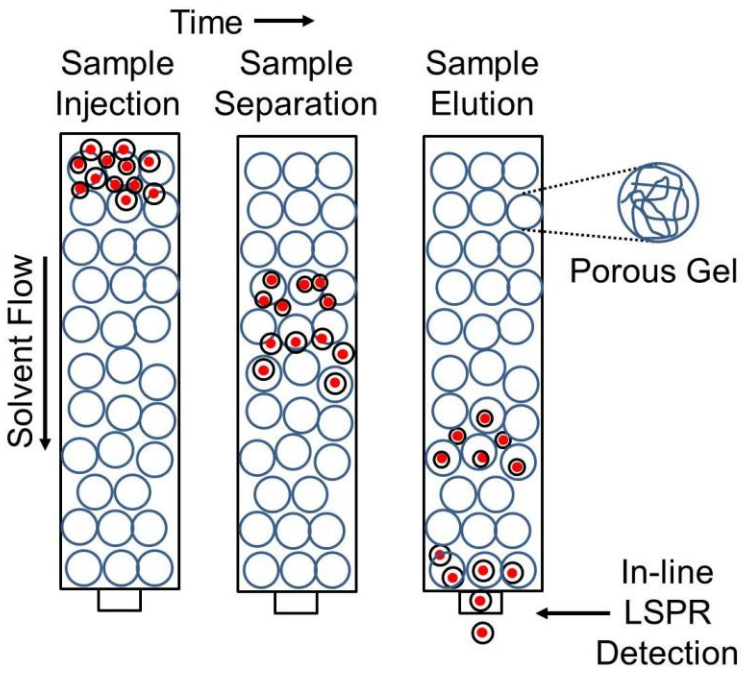

Figure 2.4. SEC separation of two $Au@SiO_2$ nanoparticle samples that differ in particle diameter. As $Au@SiO_2$ nanoparticles mixture pass though Sephacryl S-1000 column, nanoparticle separate based on size. Using in-line LSPR detection, $Au@SiO_2$ nanoparticle elution through SEC column is monitored.

total nanoparticle diameter. Size based purification of $Au@SiO_2$ nanoparticles can be achieved as long any non-specific interactions (mainly hydrophobic and electrostatic) between stationary matrix and sample are minimized.[54-55] To minimize above mentioned non-specific interactions, either stationary matrix or mobile phase compositions can be changed.[56] Changing stationary matrix is usually limited because of the required fractionation range needed to purify the sample.[57] Based on the size of the sample, there could only be few stationary matrices that are available for purification. Therefore,

changing mobile phase composition during SEC is preferred to minimize any non-specific interactions so that purification occurs based on size only.[56, 58]

$Au@SiO_2$ nanoparticle with average diameters of 27.0 ± 4.6 (11 %RSD) and 54.4 ± 5.8 (10 %RSD) are mixed together to test the separation efficiency of Sephacryl column. Because the silica shell thickness for 27 nm diameter $Au@SiO_2$ nanoparticle is ~ 6 nm, plasmon coupling is expected for distribution of nanoparticles with silica shell thickness < 6 nm during SEC fractionation.The mixture of two $Au@SiO_2$ nanoparticle samples is carefully loaded onto the column bed and SEC buffer is flowed through the column using peristaltic pump at a flow rate of 0.3 mL/min. Extinction at λ_{max} for $Au@SiO_2$ nanoparticles observed through in-line detection are plotted against elution volume to generate a chromatogram. A tailed Gaussian curve is fitted to each chromatographic peak using 10 integrations at 95% confidence interval. To evaluate column performance, a 0.5 μm polystyrene beads standard (size above the exclusion limit of Sephacryl S-1000 column) is ran before and after nanoparticle samples are fractionated. No significant differences in the polystyrene bead standard's elution profile are observed indicating no significant change in column performance. Finally, elution volumes for each $Au@SiO_2$ nanoparticle sample were adjusted to the average elution volume for the polystyrene beads standard (6.2_5 mL).

Figure 2.5A shows SEC chromatogram of $Au@SiO_2$ nanoparticle mixture with average nanoparticle diameters of 27.0 and 54.4 nm. $Au@SiO_2$ nanoparticle mixture passed through SEC exhibit two chromatographic peaks at 8.9 mL and 10.6 mL elution volumes. Maximum extinction and peak widths for the eluted peaks are: 0.93 AU, 0.59 mL; and 1.2 AU, and 0.72 mL, respectively. Because SEC separates particles based on

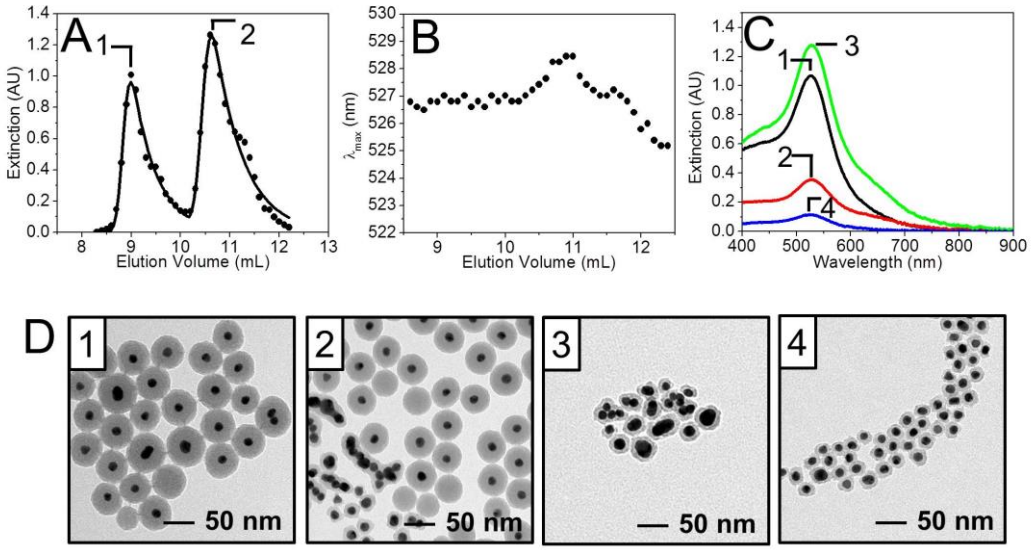

Figure 2.5. (A) SEC chromatogram of a mixture of Au@SiO_2 nanoparticles with average diameters (1) 54.4 ± 5.8 (10 %RSD) and (2) 27.0 ± 4.6 (11 %RSD). Nanoparticle samples elute at 8.9 and 10.6 mL elution volume. (B) LSPR λ_{max} analysis of eluted Au@SiO_2 nanoparticle mixture. λ_{max} remain stable at ~526.8 nm for 54.4 nm Au@SiO_2 nanoparticles. As smaller nanoparticles elute, λ_{max} increases to 528.5 nm and decreases as higher elution volumes. (C and D) LSPR spectra and TEM images of fractions collected at (1) 8.6, (2) 10.3, (3) 10.7, and (4)11.6 mL. TEM images shows the two samples are separated through SEC column. Au@SiO_2 nanoparticle sample eluted 8.6 mL does not contain smaller particles. Samples eluted at 10.3 mL show presence of both Au@SiO_2 nanoparticles.

size, it is expected that peak at 8.9 mL corresponds to larger Au@SiO_2 nanoparticles elutes and the peak at 10.6 mL consists of smaller Au@SiO_2 nanoparticles. Peak tailing are observed for both Au@SiO_2 nanoparticle samples. Calculated peak tailing factors at 10% peak height from fitted tailed Gaussian distribution are 2.5 and 2.4 for 54.4 and 27.0 nm $AuSiO_2$ nanoparticles, respectively. Peak tailing effect for both nanoparticle samples indicate presense of small non-specific Au@SiO_2 nanoparticle interactions with the column matrix. The data for separation of two Au@SiO_2 nanoparticle sizes using SEC is tabulated in Table 2.1.

LSPR λ_{max} analysis of $Au@SiO_2$ nanoparticles using in-line UV-vis detection is reported in Figure 2.5B. LSPR λ_{max} initially is ~constant at 526.8 nm which can be attributed for 54.4 nm $Au@SiO_2$ nanoparticles with average silica thickness ~21 nm so

Table 2.1. Elution volumes and peak tailing factors for a mixture of $Au@SiO_2$ nanoparticle samples through SEC.

$Au@SiO_2$ nanoparticle diameter	Elution Volume (mL)	Peak tailing factor (at 10% peak height)
54.4 ± 5.8 nm	8.9	2.5
27.0 ± 4.6 nm	10.6	2.4

that no plasmon coupling occurs. In addition the silica thickness for this sample ranges from 12.7 – 20.6 nm. Because both lower and higher end of silica thickness is greater than 8 nm, no LSPR shift as a function of silica thickness is observed for these particles as expected from model in Figure 2.3. However, as 27.0 nm $Au@SiO_2$ nanoparticles elute, the λ_{max} increases to 528.5 nm and blue shifts at higher elution volumes. Calculated average silica shell thickness for 27.0 nm diameter nanoparticles is ~6 nm. Therefore, distribution of nanoparticles with silica thickness < 6 nm is expected to electromagnetic couple according to the model in Figure 2.3C. In addition, increasing the size of Au core in $Au@SiO_2$ nanoparticle can also increase λ_{max}. As elution volume increases, λ_{max} blue shifts indicating that particles elute without the presence of electromagnetic coupling and LSPR maximum is influenced by decreasing silica thickness. Figure 2.5C and D shows

LSPR spectra and respective TEM images collected at 8.6, 10.3, 10.7, and 11.6 mL elution volumes. Two different average diameters are separated based on size where 54.4 nm particles elute at lower elution volume and 27.0 nm particles elute at longer elution volumes. LSPR spectrum of fraction collected at 8.6 mL elution volume exhibit wavelength maximum centered at 526.8 nm and indicate no plasmon coupling effect. However, λ_{max} of fractions at collected at 10.3 and 10.7 mL is red-shifted compared to 526.8 nm; and the LSPR spectra clearly show a shoulder at longer wavelenth (centered at 650 nm) indicating LSPR coupling and presence of multiple Au cores. TEM images collected for fraction at 8.6 mL shows individual Au@SiO_2 nanoparticles with silica shell thickness greater than 8 nm consistent with LSPR. Figure 2.5D2 collected at 10.3 mL elution volume shows presence of both big and small Au@SiO_2 nanoparticle samples indicating that both samples are not completely resolved. Calculated SEC resolution between the two Au@SiO_2 nanoparticle diameters of 0.72 also indicate partially resolved SEC peaks. In addition, some of the smaller Au@SiO_2 nanoparticles exhibit multiple cores (Au core clusters) that can cause new LSPR band to grow in at 650 nm. Similarly, TEM analysis of fraction collected at 10.7 nm not only exhibit Au@SiO_2 with multiple Au core but also some Au@SiO_2 nanoparticles with bigger Au cores. As a result λ_{max} increases to 528.5 nm and peak shoulder at longer wavelength (~650 nm) is observed. Finally, Figure 2.5D4 shows that Au@SiO_2 fraction at 11.6 mL contains single Au core. TEM diameter analysis of eluted fractions indicate that average nanoparticle diameters of 56.1 ± 7.4, 50.5 ± 5.0 (big AuSiO_2 nanoparticles only), 28.5 ± 9.3, and 24.3 ± 4.3 nm for fractions eluted at 8.6, 10.3, 10.7, and 11.6 mL, respectively. Average Au@SiO_2 nanoparticle diameters are verified to be statistically different using t-test. TEM analysis

indicate that modest fractionation of each $Au@SiO_2$ nanoparticle sample occurred during SEC. These results supports the hypothesis that surfactant-free SEC can be used to separate $Au@SiO_2$ nanoparticles, however, with limited fractionation capacity at the experimental conditions implemented above.

2.3.5 Conclusion

In conclusion, various diameters of $Au@SiO_2$ nanoparticles were synthesized by changing thickness of silica using 0.60 – 0.90 mM sodium silicate. The diameter distribution of $Au@SiO_2$ nanoparticles further increased upon silica coating signifying that sol-gel processing of nanoparticles increases sample heterogeneity. Upon passing 39.7 nm $Au@SiO_2$ nanoparticles through SEC column, the optical property and shape/size morphology was still maintained which is important for further nanoparticle applications. Moreover, it was also shown that a surfactant free separation of silica coated gold nanoparticles is possible. SEC data indicated that nanoparticle separation is a size dependent process; although only modest separation resolution of 0.7 was achieved between 54.4 and 27.0 nm silica coated Au nanoparticles. In addition, the surfactant-free SEC does not adversely affect nanoparticle stability (LSPR and size/shape morphology) and utility, making SEC an ideal technique for the purification/separation of nanoparticles once non-specific interactions are minimized.

1. Campbell, C. T.; Parker, S. C.; Starr, D. E., The Effect of Size-Dependent Nanoparticle Energetics on Catalyst Sintering. *Science* **2002**, *298*, 811-814.
2. Oh, E., et al., Cellular Uptake and Fate of Pegylated Gold Nanoparticles Is Dependent on Both Cell-Penetration Peptides and Particle Size. *ACS Nano* **2011**, *5*, 6434-6448.
3. Zeng, S.; Yu, X.; Law, W. C.; Zhang, Y.; Hu, R.; Dinh, X. Q.; Ho, H. P.; Yong, K. T., Size Dependence of Au Np-Enhanced Surface Plasmon Resonance Based on Differential Phase Measurement. *Sens. Actuators* **2013**, *176*, 1128-1133.

4. Wang, H.; Schultz, Z. D., The Chemical Origin of Enhanced Signals from Tip-Enhanced Raman Detection of Functionalized Nanoparticles. *Analyst* **2013**, *138*, 3150-1357.
5. Bell, S. E. J.; McCourt, M. R., Sers Enhancement by Aggregated Au Colloids: Effect of Particle Size. *Phys. Chem. Chem. Phys.* **2009**, *11*, 7455-7462.
6. Fang, P.; Li, J. F.; Yang, Z.; Li, L. M.; Ren, B.; Tian, Z., Optimization of Sers Activities of Gold Nanoparticles and Gold-Core–Palladium-Shell Nanoparticles by Controlling Size and Shell Thickness. *J. Raman Spect.* **2008**, *39*, 1679-1687.
7. Alvarez-Puebla, R. A.; Arceo, E.; Goulet, P. J. G.; Garrido, J. J.; Aroca, R. F., Role of Nanoparticle Surface Charge in Surface-Enhanced Raman Scattering. *J. Phys. Chem. B* **2005**, *109*, 3787-3792.
8. Haruta, M.; Delmon, B. J., *J. Chem. Phys.* **1986**, *83*, 859-868.
9. Haiss, W.; Thanh, N. T. K.; Aveyard, J.; Fernig, D. G., Determination of Size and Concentration of Gold Nanoparticles from Uv-Vis Spectra. *Anal. Chem.* **2007**, *79*, 4215-4221.
10. Volkert, A. A.; Subramaniam, V.; Haes, A. J., Implications of Citrate Concentration During the Seeded Growth Synthesis of Gold Nanoparticles. *Chem. Commun.* **2011**, *47*, 478-480.
11. McGilvray, K. L.; Fasciani, C.; Bueno-Alejo, C. J.; Schwartz-Narbonne, R.; Scaiano, J. C., Photochemical Strategies for the Seed-Mediated Growth of Gold and Gold-Silver Nanoparticles. *Langmuir* **2012**, *46*, 16148-16155.
12. Pierre, M. C. S.; Haes Amanda, J., Purification Implications on Sers Activity of Silica Coated Gold Nanospheres. *Anal Chem* **2012**, *84*, 7906-7911.
13. Green, A. A.; Hersam, M. C., Processing and Properties of Highly Enriched Double-Wall Carbon Nanotubes. *Nat. Nanotechnol.* **2009**, *4*, 64-70.
14. Novak, J. P.; Nickerson, C.; Franzen, S.; Feldheim, D. L., Purification of Molecularly Bridged Metal Nanoparticle Arrays by Centrifugation and Size Exclusion Chromatography. *Anal. Chem.* **2001**, *73*, 5758-5761.
15. Chen, G.; Wang, Y.; Tan, L. H.; Yang, M.; Tan, L. S.; Chen, Y.; Chen, H., High-Purity Separation of Gold Nanoparticle Dimers and Trimers. *J. Am. Chem. Soc.* **2009**, *131*, 4218-4219.
16. Sweeney, S. F.; Woehrle, G. H.; Hutchison, J. E., Rapid Purification and Size Separation of Gold Nanoparticles Via Diafiltration. *J. Am. Chem. Soc.* **2006**, *128*, 3190-3197.
17. Wei, G.-T.; Liu, F.-K.; Wang, C. R. C., Shape Separation of Nanometer Gold Particles by Size-Exclusion Chromatography. *Anal. Chem.* **1999**, *71*, 2085-2091.
18. Liu, F.-K., Monitoring Stability and Sizes of Au/Pd Core/Shell Nanoparticles by Sec. *Chromatogr.* **2009**, *70*, 7-13.
19. Liu, F.-K., Sec Characterization of Au Nanoparticles Prepared through Seed-Assisted Synthesis. *Chromatogr.* **2007**, *66*, 791-796.
20. Liu, F.-K., Monitoring the Synthesis of Au Nanoparticles Using Sec. *Chromatogr.* **2008**, *68*, 81-87.
21. Gole, A.; Murphy, C. J., Biotin-Streptavidin-Induced Aggregation of Gold Nanorods: Tuning Rod-Rod Orientation. *Langmuir* **2005**, *21*, 10756-10762.
22. Pastoriza-Santos, I. P.-J., J.; Liz-Marzan, L. M., Silica-Coating and Hydrophobation of Ctab-Stabilized Gold Nanorods. *Chem. Mater.* **2006**, *18*, 2465-2467.
23. Nikoobakht, B.; El-Sayed, M. A., Surface-Enhanced Raman Scattering Studies on Aggregated Gold Nanorods. *J. Phys. Chem. A* **2003**, *107*, 3372-3378.
24. Lou, S.; Ye, J.-y.; Li, K.-q.; Wu, A., A Gold Nanoparticle-Based Immunochromatographic Assay: The Influence of Nanoparticulate Size. *Analyst* **2011**, *137*, 1174-1181.
25. Siebrands, T.; Giersig, M.; Mulvaney, P.; Fischer, C. H., Steric Exclusion Chromatography of Nanometer-Sized Gold Particles. *Langmuir* **1993**, *9*, 2297-300.

26. Striegel, A.; Yau, W. W.; Kirkland, J. J.; Bly, D. D., *Modern Size-Exclusion Liquid Chromatography: Practice of Gel Permeation and Gel Filtration Chromatography*, 2 ed.; John Wiley & Sons, Inc., 2009.
27. Roca, M.; Haes, A. J., Silica-Void-Gold Nanoparticles: Temporally Stable Surf Ace-Enhanced Raman Scattering Substrates. *J. Am. Chem. Soc.* **2008**, *130*, 14273-14279.
28. Ciriminna, R.; Sciortino, M.; Alonzo, G.; Schrijver, A. d.; Pagliaro, M., From Molecules to Systems: Sol-Gel Microencapsulation in Silica-Based Materials. *Chemical Reviews* **2011**, *111*, 765-789.
29. Roca, M.; Haes, A. J., Silica-Void-Gold Nanoparticles: Temporally Stable Surface-Enhanced Raman Scattering Substrates. *J. Am. Chem. Soc.* **2008**, *130*, 14273-14279.
30. Liz-Marzan, L. M.; Giersig, M.; Mulvaney, P., Synthesis of Nanosized Gold-Silica Core-Shell Particles. *Langmuir* **1996**, *12*, 4329-4335.
31. Ung, T.; Liz-Marzan, L. M.; Mulvaney, P., Controlled Method for Silica Coating of Silver Colloids. Influence of Coating on the Rate of Chemical Reactions. *Langmuir* **1998**, *14*, 3740-3748.
32. Stober, W.; Finx, A.; Bohn, E., Controlled Growth of Monodisperse Silica Spheres
in the Micron Size Range. *J. Coll. Interface Sci.* **1968**, *26*, 62.
33. Roca, M.; Pandya, N. H.; Nath, S.; Haes, A. J., Linear Assembly of Gold Nanoparticle Clusters Via Centrifugation. *Langmuir* **2010**, ACS ASAP.
34. Roca, M.; Mackie, P. M.; Haes, A. J., Design of a Biocompatible and Optically-Stable Solution-Phase Substrate for Sers Detection. *Mat. Res. Soc. Symp. Proc.* **2009**, *1133*, AA09-02.
35. Tyler, T. P.; Henry, A.-I.; Van Duyne Richard, P.; Hersam, M. C., Improved Monodispersity of Plasmonic Nanoantennas Via Centrifugal Processing. *Journal of Physical Chemistry Letters* **2011**, *2*, 218-222.
36. Grabar, K. C.; Freeman, R. G.; Hommer, M. B.; Natan, M. J., Preparation and Characterization of Au Colloid Monolayers. *Anal. Chem.* **1995**, *67*, 735-43.
37. Park, S.-J.; Kim, Y.-J.; Park, S.-J., Size-Dependent Shape Evolution of Silica Nanoparticles into Hollow Structures. *Langmuir* **2008**, *24*, 12134-12137.
38. Marie Carmelle S. Pierre; Haes, A. J., Purification Implications on Sers Activity of Silica Coated Gold Nanospheres. *Anal. Chem.* **2012**, *84*, 7906-7911.
39. Liu, S.; Zhang, Z.; Wang, Y.; Wang, F.; Han, M.-Y., Surface-Functionalized Silica-Coated Gold Nanoparticles and Their Bioapplications. *Talanta* **2005**, *67*, 456-461.
40. Varuni Subramaniam; Griffith, L.; Haes, A. J., Varying Nanoparticle Pseudostationary Phase Plug Length During Capillary Electrophoresis. *Analyst* **2011**, *136*, 3469-3477.
41. Kimling, J.; Maier, M.; Okenve, B.; Kotaidis, V.; Ballot, H.; Plech, A., Turkevich Method for Gold Nanoparticle Synthesis Revisited. *J. Phys. Chem. B FIELD Full Journal Title:Journal of Physical Chemistry B* **2006**, *110*, 15700-15707.
42. Jain, P. K.; Huang, X.; El-Sayed, I. H.; El-Sayed, M. A., Noble Metals on the Nanoscale: Optical and Photothermal Properties and Some Applications in Imaging, Sensing, Biology, and Medicine. *Acc. Chem. Res.* **2008**, *41*, 1578-1586.
43. Berciaud, S.; Cognet, L.; Philippe, T.; Lounis, B., Observation of Intrinsic Size Effects in the Optical Response of Individual Gold Nanoparticles. *Nano Lett. FIELD Full Journal Title:Nano Letters* **2005**, *5*, 515-518.
44. Haes, A. J.; Van Duyne, R. P., A Nanoscale Optical Biosensor: Sensitivity and Selectivity of an Approach Based on the Localized Surface Plasmon Resonance Spectroscopy of Triangular Silver Nanoparticles. *J. Am. Chem. Soc.* **2002**, *124*, 10596 - 10604.
45. Anker, J. N.; Hall, W. P.; Lyandres, O.; Shah, N.; Zhao, J.; Van Duyne, R. P., Biosensing with Plasmonic Nanosensors. *Nat. Mat.* **2008**, *7*.
46. Jung, L. S.; Campbell, C. T.; Chinowsky, T. M.; Mar, M. N.; Yee, S. S.,

Quantitative Interpretation of the Response of Surface Plasmon Resonance Sensors to Adsorbed Films. *Langmuir* **1998**, *14*, 5636-5648.
47. Volkert, A. A.; Pierre, M. C. S.; Shrestha, B.; Haes, A. J., Implications of Sample Aging on the Formation of Internally Etched Silica Coated Gold Nanoparticles. *RSC Advances* **2015**, *5*, 3774-3780.
48. Kuchuk, V. I.; Shirokova, I. Y.; Golikova, E. V., Physicochemical Properties of Water-Alcohol Mixtures of a Homological Series of Lower Aliphatic Alcohols. *Glass Phys Chem* **2012**, *38*, 460-465.
49. Chu, K.-Y.; Thompson, A. R., Densities and Refractive Indices of Alcohol-Water Solutions of N-Propyl, Isopropyl, and Methyl Alcohols. *Journal of Chemical & Engineering Data* **1962**, *7*, 358-360.
50. Su, K. H.; Wei, Q.-H.; Zhang, X.; Mock, J. J.; Smith, D. R.; Schultz, S., *Nano Lett. FIELD Full Journal Title:Nano Letters* **2003**, *3*, 1087-1090.
51. Jain, P. K.; Huang, W.; El-Sayed, M. A., On the Universal Scaling Behavior of the Distance Decay of Plasmon Coupling in Metal Nanoparticle Pairs: A Plasmon Ruler Equation. **2007**.
52. Funston, A. M.; Novo, C.; Davis, T. J.; Mulvaney, P., Plasmon Coupling of Gold Nanorods at Short Distances and in Different Geometries. **2009**, *9*, 1651-1658.
53. Su, J.; Mrksich, M., Using Maldi-Tof Mass Spectrometry to Characterize Interfacial Reactions on Self-Assembled Monolayers. *Langmuir* **2003**, *19*, 4867-4870.
54. Belew, M.; Porath, J.; Fohlman, J., Absorption Phenomena on Sephacryl S-200 Superfine. *Journal of chromatgography* **1978**, *147*, 205-212.
55. Johansson, B.-L.; Gustavsson, J., Elution Behaviour of Some Proteins on Fresh, Acid- or Base- Treated Sephacryl S-200 Hr. *Journal of Chromatgography* **1988**, *457*, 205-213.
56. Arakawa, T.; Ejima, D.; Li, T.; Philo, J. S., The Critical Role of Mobile Phase Composition in Size Exclusion Chromatography of Protein Pharmaceuticals. *Journal of Pharmaceutical Sciences* **2010**, *99*, 1674-1692.
57. Berek, D., Size Exclusion Chromatography - a Blessing and a Curse of Science and Technology of Synthetic Polymers. *Journal of Separation Science* **2010**, *33*, 315-335.
58. Hong, P.; Koza, S.; Bouvier, E. S. P., A Review Size-Exclusion Chromatography for the Analysis of Protein Biopherapeutics and Their Aggregates. *Journal of Liquid Chromatography & Related Technologies* **2012**, *35*, 2923-2950.

CHAPTER 3 IMPLICATIONS OF SOLUTION IONIC STRENGTH, PH, AND POLARITY IN THE PASSIVE TRANSPORT OF SMALL ANALYTES THROUGH SILICA MEMBRANE STABILIZED GOLD COATED SILVER NANOPARTICLES

3.1 Introduction

Plasmonic nanoparticles possess unique optical property known as localized surface plasmon resonance (LSPR) that allows molecular detection using surface-enhanced Raman scattering in biological and environmental samples.[1-4]SERS phenomenon relies on chemical and electromagnetic enhancement mechanisms which increases molecular signal by 2 – 9 orders of magnitude.[1, 5-9] Both mechanisms require that molecules diffuse towards the plasmonic nanoparticle surface and interact at short metal to molecule distances (< 2 nm). To generate a detectable SERS signal that can be quantified within a short assay time, molecular mass transport from the bulk solution to the metal surface must be promoted while maintaining nanoparticle plasmonic property.

One class of microporous material which maintains the core properties and consists of practical significance in molecular transport is silica.[1, 10-12] Molecular transport through these porous membranes occurs mainly by diffusion and controls the overall rate of the process. Dense microporous silica matrix with pore size < 2 nm[13] often hinders molecular diffusion to the core, limiting use of such silica membranes for mass transport studies or sensing applications. Different diffusion mechanism diffusion control molecular transport in porous material. Diffusion in microporous spherical particle is governed by (1) sterics, (2) interactions between the diffusing molecule and the pore wall, and (3) mass transport resistance along the external surface of the porous particle.

Limitations in molecular transport across the porous material influence molecular detection ability regardless of the detection technique used.[14] For example with advancement in SERS and design of substrates with high enhancement factors, single molecular SERS is achieved; however, probability of detecting a single molecule still is limited by molecular diffusion to the SERS-active site.[15-16]

Molecular transport through silica membranes can be increased by increasing silica porosity. Previously, successful surface protective etching process allowed conversion of sol-gel derived silica into permeable structures by coating silica surface with layer of polymeric ligands such as polyvinyl pyrrolidone.[10] In another report, internally etched silica coated gold nanoparticles showed that quantitative SERS is possible by generating internal voids in the silica membrane.[1] Preferential etching of low crosslinked internal silica compared to high crosslinked external silica not only allowed molecular diffusion to metal core for SERS detection but also maintained nanoparticle plasmonic property. SERS detection was achieved by decreasing silica cross-linking near the metal core which increased internal voids for molecular adsorption. Temporally consistent SERS without electromagnetic coupling was reported. This was a tremendous break though in utilizing silica surface chemistry for achieving nanoparticle plasmonic stability and quantitative SERS. However, molecular transport studies that include how temporal SERS changes as a function of solution parameters such as ionic strength, pH, and polarity were lacking. Studying kinetics of molecular transport across internally etched silica coated nanoparticles is important in order to use these nanostructures for quantitative molecular detection or designing experimental conditions that allow selective molecular detection in complex sample conditions by utilizing differences in molecular

transport kinetics through silica.

Herein, internally etched silica coated silver@gold nanoparticles with constant silica effective refractive index are used to study the implicating of solution parameters such as ionic strength, pH, and polarity on mass transport of 2-naphthalenethiol, benzenethiol, 4-mercaptobenzoic acid, and p-aminothiophenol through silica. These molecules are chosen because they are similar molecules that differ either in size or functional group. It is expected that varying these solution parameters, molecular charge as well as charge on silica pores changes allowing molecules to interact with the silica and exhibit differences in molecular transport which can be studied using SERS. SERS temporal profiles are generated by plotting SERS signals as a function of time for each molecule. The observed SERS temporal profiles are fitted with first-order time dependent Langmuir isotherm model to generate rate constant that indicates rate at which the 3D SERS-active volume near the nanoparticle cores are filled as the solution parameters such as ionic strength, pH, and polarity are changed. Understanding the implication of molecular transport through silica membrane for IE Ag@Au@SiO_2 nanoparticles by studying SERS kinetic rate constants are important for designing parameters for selective molecular detection in complex biological/environmental samples.

3.2 Experimental Materials and Methods

3.2.1 Chemical Reagents

Gold(III) chloride trihydrate, sodium citrate dihydrate, Amberlite MB-150 mixed bed exchange resin, (3-aminopropyl) trimethoxysilane (APTMS), sodium chloride (NaCl), sodium trisilicate (27%), tetraethyl orthosilicate (TEOS), silver perchlorate, sodium borohydride, and hydroxylamine hydrochloride were purchased from Sigma. Ethanol,

ammonium hydroxide (NH_4OH), hydrochloric acid (HCl), and nitric acid (HNO_3) were purchased from Fisher Scientific (Pittsburgh, PA). Ultrapure water (18.2 MΩ cm^{-1}) was obtained from a Barnstead Nanopure System and used for all experiments. All glassware items were cleaned with aqua regia (3:1 HCl/ HNO_3) and rinsed thoroughly with water, and oven (glass) or air (plastic) dried overnight before use.

3.2.2 Silver@Gold Nanoparticle Synthesis

Ag@Au nanoparticles were synthesized using seeded growth method previously described in literature.[17-18] Briefly, 100 mL water containing 0.3 mM sodium citrate prepared in nitrogen-purged water stirred on an ice bath in the dark. Freshly prepared sodium borohydride solution in ice cold water was added onto the solution immediately following the preparation (final sodium borohydride concentration = 1 mM). Next, 1 mL of 10 mL of silver perchlorate was added to the solution within 2 minutes, and the resulting silver nanoparticles solution was stirred for 3 minutes. Stirring was stopped, and silver nanoparticles with average diameter ranging from 8 – 11 nm formed within 3 hours. After 3 hours of silver nanoparticle growth, the LSPR of silver nanoparticles was collected by diluting silver nanoparticle in half. Silver nanoparticles synthesized exhibited LSPR wavelength maximum between 393 – 397 nm.

Next, 20 mL of water was added to 25 mL of as-synthesized Ag seed stirred for ~2 minutes (4 °C). 15 mL of both 6.25 mM hydroxylamine hydrochloride and 0.465 mM gold salt solution were added slowly (3 mL/min) using syringe pump. This Ag@Au nanoparticle solution was stirred for 1 hour to ensure nanoparticle formation and stored at 2 – 4 °C until use. The concentration of these materials was estimated using a standard estimation model for the silver seeds using extinction spectroscopy.[19]

3.2.3 Microporous Silica-Coated Ag@Au Nanoparticles Synthesis

Silica shells on Ag@Au nanoparticles were synthesized via a modified Stöber method.[11, 20-22] Briefly, pH and conductivity of 25 mL as-synthesized Ag@Au nanoparticles were adjusted to 5 and ~110 µS/cm using NH_4OH and amberlite resin, respectively. After resin removal via filtration, 129.2 µL of 1 mM APTMS was added drop-wise to the nanoparticle solution (with stirring). After 30 minutes, 201 µL of 2.7 % sodium silicate solution was added slowly to the solution and stirred for 24 hours. The silica shell thickness was further increased by adding ethanol (final ratio of 1 part water to 4.4 parts ethanol). After 6 hours, 20 µL of 1 mM APTMS and 20 µL TEOS were added. The pH was increased to ~11 using concentrated ammonium hydroxide. After 16 hours, the $Ag@Au@SiO_2$ nanoparticles were centrifuged (45 min, 9383×g) three times with ethanol then 3 times with water. The $Ag@Au@SiO_2$ nanoparticles were then passed through Sephadex-G50 column to remove Ag@Au nanoparticles that did not contain complete silica shells[2] and stored in ethanol until use.

3.2.4 Internally Etched Silica-Coated Silver@Gold Nanoparticle Synthesis

Silica shells were converted into silica membranes via an internal silica etching process induced at basic pH values. Because the $Ag@Au@SiO_2$ was stored in ethanol, the samples were triply centrifuge and redispersed in water to a concentration of 3 nM. Concentrated NH_4OH was added to the solution to induce internal etching.[1, 20] The reaction was quenched by adding 100 mM HNO_3 until the solution pH was ~6. Finally, the nanoparticles were washed 3 times in water and passed through a Sephadex-G50

column to remove defect particles.

3.2.5 Extinction and SERS Spectroscopies

Localized surface plasmon resonance (LSPR) spectra were collected using disposable methacrylate cuvette (pathlength = 1 cm) and an ultraviolet-visible (UV-vis) spectrometer (Ocean Optics USB4000). Either deuterium or halogen lamps were used for UV and visible excitation, respectively. LSPR spectra were collected in transmission geometry every minute for 2 hours (integration time = 60 msec, average = 25 scans, and boxcar = 10), and extinction maximum wavelengths (λ_{max}) were determined from the zero-point crossing of the first derivative. LSPR spectra were processed using MATLAB program.

3.2.6 Transmission Electron Microscopy (TEM)

TEM was performed using a JEOL JEM-1230 microscope equipped with a Gatan CCD camera. Samples were prepared on 400 mesh copper grids that were coated with a thin film of Formvar and carbon (Ted Pella). The nanoparticle solution was diluted in a 50% water−ethanol mixture, and ~10 μL of the solutions were pipetted onto grids and dried. At least 200 nanoparticles were analyzed (Image Pro Analyzer) to estimate average nanoparticle diameters.

3.2.7 SERS Sample Preparation

SERS spectra were collected simultaneously to the LSPR measurements at a 90° angle from the UV-vis light sources. SERS measurements were performed using 6 nM IE Ag@Au@SiO_2 nanoparticles prepared in various solution ionic strength, pH, and polarity. Ionic strength of the solution was increased by adding various amounts of 100

mM KCl such that final ionic strengths from added salt were 0, 10, 25, 50, 75, and 100 mM. For pH studies, 6 nM IE Ag@Au@SiO_2 nanoparticles were suspended in 4.0, 5.5, 6.6, 7.5, and 9.0 solution pH. Solution polarity effect was studies by preparing, 6 nM IE Ag@Au@SiO_2 nanoparticles sample containing 0, 5, 10, 15, 20, and 30% v/v MeOH. 10 µM final 2-naphthalenethiol, benzenethiol, 4-mercaptobenzoic acid, and p-aminothiophenol were used for SERS studies. After the addition of analyte, samples were briefly vortexed for 3 s and SERS collected every 10 seconds using Delta Nu Advantage (laser = 632.8 nm) system. SERS spectra were processed using MATLAB program.

3.3 Results and Discussion

The transport process of molecules through silica pores is governed by molecular (a) Brownian motion in bulk solution, (b) diffusion through the solution layer at the silica interface, (c) adsorption and desorption from external silica interface, and (d) diffusion within and through the pores.[13] Separation of protein,[23-25] ion[26] and molecular transport[27] have previously been demonstrated using self-assembled silica nanospheres, polymers, and gold deposited polymeric nanopores. These studies indicate that solution parameters that control molecular and silica/polymer charge play a big role in molecular transport/separation. In the following study, SERS spectroscopy is used to monitor adsorption to the Ag@Au core after the molecules diffuse through etched silica; so that influence of solution parameters such as ionic strength, pH, and polarity on molecular transport as well as SERS is determined. Observed SERS intensities are limited by molecular transport to the metal core; therefore, kinetic constant determined using SERS temporal profile will elucidate molecular transport rate for a specific molecule. It is expected that for fixed solvent parameters and silica morphology (porosity and surface

charge), kinetic rate constant and SERS depends on molecular function group, molecular size, or any adsorption/desorption processes occurring at the silica-liquid interface as well as inside silica pores. To study these effects, 2-naphthalenethiol, benzenethiol, 4-mercaptobenzoic acid, and p-aminothiophenol molecules with various sizes, and functional groups are used. In order to study kinetic effects on SERS, the molecule must be evenly distributed in the solution (achieved by vortexing the solution for 3 seconds) so that molecular transport through silica is not limited by bulk solution mass transport from the source of molecule addition to the silica surface. Binding studies of benzenethiol on Klarite showed that the binding rate decreased by up to 30 times when the mass transport from the point of source to the Klarite substrate was limited by bulk mass transport.[28]

To study implications of solution parameters such as ionic strength, pH, and polarity on rate constants associated with temporal SERS intensities when molecules occupy the 3D SERS-active volume, IE Ag@Au@SiO_2 nanoparticles with silica effective refractive index of 1.38 are used. Figure 3.1A shows TEM image of IE Ag@Au@SiO2 nanoparticles synthesized by preferentially etching the internal lower crosslinked silica compared to the external high crosslinked silica shell as established in literature.[1] TEM image show porous silica membrane containing Ag@Au cores with core diameter of 26.0 ± 5.4 nm and total nanoparticle diameter of 76.9 ± 7.7 nm. The TEM image also shows presence of few etched free silica particles devoid of metal cores – one of the limitations in silica sol-gel synthesis. Free silica occurs because silica precursors nucleate during the ethanol addition step and grow.[11] Free silica nanoparticles cannot be separated using Sephadex G-50 column purification method used to remove silica

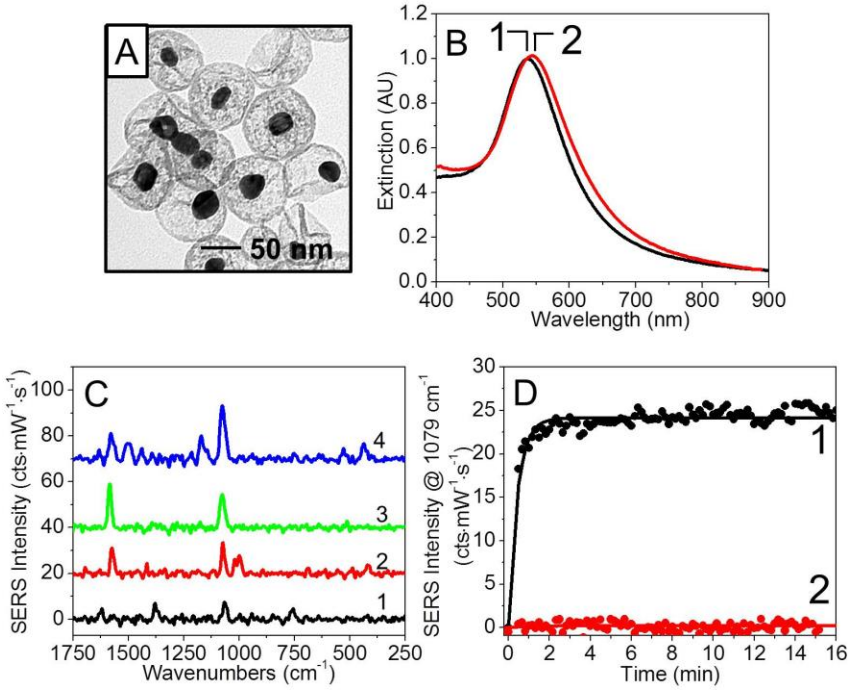

Figure 3.1. (A) TEM image of IE Ag@Au@SiO_2 nanoparticles. Ag@Au core and IE Ag@Au@SiO_2 nanoparticle average diameters are 26.0 ± 5.4 nm and 76.9 ± 7.7 nm. (B) LSPR analysis of IE Ag@Au@SiO_2 nanoparticles before and after addition of 4-aminothiophenol. After addition of 4-aminothiophenol molecules, LSPR λ_{max} red shifts from (1) 538.9 nm to (2) 543.8 nm as the local refractive index around nanoparticle core increases from molecules occupying SERS-active volume near metal core. (C) SERS spectra of 10 µM (1) 2-naphthalenethiol, (2) benzenethiol, (3) 4-mercaptobenzoic acid, and (4) p-aminothiophenol in 100 mM ionic strength and pH 6.5 phosphate buffer after 15 minutes of incubation time. Spectra show ring stretching mode at 1622, 1575, 1585, and 1594 cm^{-1}; and CS stretch contributions at 1067, 1074, 1078, and 1079 cm^{-1}; respectively for 2-naphthalenethiol, benzenethiol, 4-mercaptobenzoic acid, and p-aminothiophenol. In addition, 2-naphthalenethiol show strong ring stretching mode at 1380 cm^{-1} whereas benzenethiol shows additional intense peaks at 1021 and 997 cm^{-1} associated with CH bending and out of plane ring deformation. (D) Temporal SERS (1) and normal Raman (2) profile of p-aminothiophenol in 100 mM ionic strength and pH 6.5 phosphate buffer collected every 10s collected. The fitted curve represents first-order time dependent Langmuir isotherm.

uncoated Ag@Au nanoparticles. Depending on the total number of these free etched silica nanoparticles, SERS can be impacted because molecules can diffuse through these

free silica nanoparticles and lower the number of molecules available for SERS. Minimizing number of free silica by synthetic or purification method, therefore, is vital for SERS. Multiple TEM images obtained for IE Ag@Au@SiO_2 nanoparticles indicate ~10% free silica so that a 10% loss in available molecules for SERS is expected assuming added molecules equally diffuse through all silica shells with/without Ag@Au cores.

LSPR analysis of IE Ag@Au@SiO_2 nanoparticles shows that the λ_{max} red shifts 4.9 nm (538.9 to 543.8 nm) upon incubation with p-aminothiophenol molecules (Figure 3.1B). The red shift is attributed to increase in local refractive index as p-aminothiophenol occupy SERS-active volume near the metal core. No electromagnetic coupling of IE Ag@Au@SiO_2 nanoparticles even in the presence of p-aminothiophenol molecules indicate that the observed SERS signals solely arises from chemical and electromagnetic enhancement from isolated metal cores; therefore, SERS signals should increase and stabilizes over time. SERS spectra of 2-naphthalenethiol, benzenethiol, 4-mercaptobenzoic acid, and p-aminothiophenol collected using 632.8 nm Raman system is shown in Figure 3.1C. SERS spectra indicate that CS stretching mode appears at 1067, 1074, 1078, and 1079 cm^{-1}, for 2-naphthalenethiol, benzenethiol, 4-mercaptobenzoic acid, and p-aminothiophenol, respectively. Ring stretching modes are also observed at 1622, 1575, 1585, and 1594 $cm^{-1}$for these molecules. In addition, 2-naphthalenethiol also shows strong ring stretching mode at 1380 cm^{-1} whereas benzenethiol shows additional intense peaks at 1021 and 997 cm^{-1} associated with CH bending and out of plane ring deformation.

Figure 3.1D shows temporal SERS evolution for CS stretching mode of 10 µM p-

aminothiophenol in 6 nM IE Ag@Au@SiO_2 nanoparticles incubated in 100 mM KCl. Observed SERS profile is modeled with first-order time dependent Langmuir isotherm.[28-29] Equation 3.1 represents first-order time dependent Langmuir kinetics as[28]

$$\theta = 1 - e^{-kt} \qquad 3.1$$

where, $\theta = I_{SERS}/I_{SERS}^{max}$, k is the rate constant (min^{-1}), and t is the incubation time (min). Fitting SERS temporal curves for various molecules to equation 3.1, SERS rate constant were obtained. Langmuir kinetics of first order is selected because the SERS profile exhibited Langmuir type exponential curve; and for a fixed nanoparticle concentration and solution condition, SERS depends on the number of molecules occupying the 3D SERS-active volume. Detection of 10 μM concentration of 2-naphthalenethiol, benzenethiol, 4-mercaptobenzoic acid, or p-aminothiophenol using Raman under identical conditions as SERS is not possible because signal associated with these molecules are below the S/N. Figure 3.1D2 indicates that no Raman signal is observed for 10 μM p-aminothiophenol molecule alone. Through chemical and electromagnetic mechanisms, SERS allows enhancement of p-aminothiophenol signals above the detector S/N utilizing the LSPR properties of Ag@Au core. These data suggest that plasmonic properties of Ag@Au core is maintained and first-order time dependent Langmuir isotherm predicts SERS temporal profiles.

3.3.1 Determination of SERS rate constants as a function of ionic strength

To determine ionic strength implications on SERS rate constants, 6 nM IE Ag@Au@SiO_2 nanoparticles are suspended in 0, 10, 25, 50, 75, and 100 mM ionic strength solution adjusted with KCl. 10 μM 2-naphthalenethiol, benzenethiol, 4-

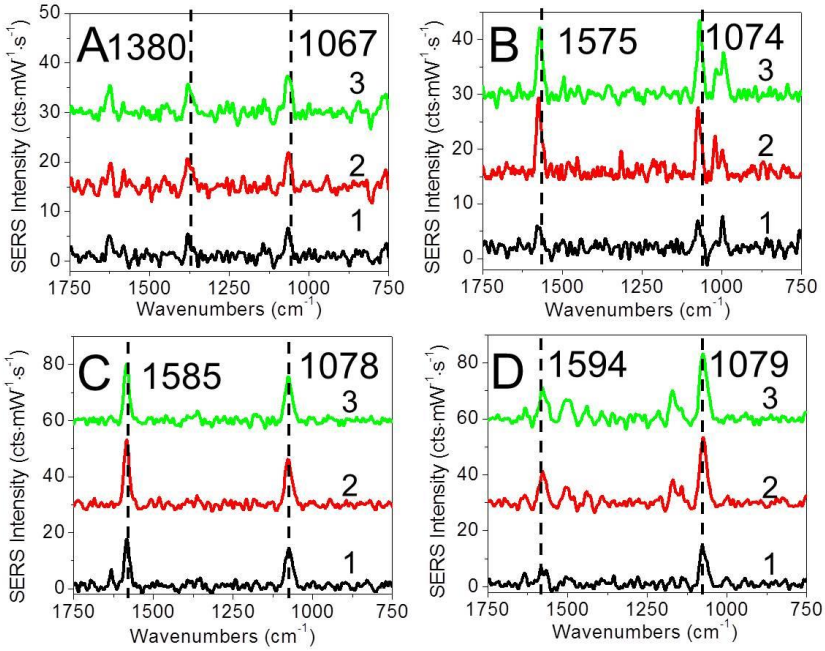

Figure 3.2. Saturated SERS spectra plotted for (A) 2-naphthalenethiol, (B) benzenethiol, (C) 4-mercaptobenzoic acid, and (D) p-aminothiophenol at (1) 0, (2) 50, and (3) 100 mM ionic strength and pH 6.5 phosphate buffer after 15 minutes of incubation time. Spectra show ring stretching mode at 1622, 1575, 1585, and 1594 cm^{-1}; and CS stretch contributions at 1067, 1074, 1078, and 1079 cm^{-1}; respectively for 2-naphthalenethiol, benzenethiol, 4-mercaptobenzoic acid, and p-aminothiophenol molecules. SERS parameters: λ_{ex} = 632.8 nm, t_{int} = 10 s, and P = 2 mW.

mercaptobenzoic acid, and p-aminothiophenol are used for the study. It is expected that benzenethiol, 4-mercaptobenzoic acid, and p-aminothiophenol molecules exhibit similar size based transport whereas 2-napthalenethiol with 2 benzene rings will have slower diffusion compared to other molecules based on size. Also 4-mercaptobenzoic acid is overall negatively charged whereas p-aminothiophenol is positively charged at pH 6.5 used for these experiments. Figure 3.2 shows SERS spectra of each molecule at 0, 50, and 100 mM solution ionic strength. CS stretching mode is clearly observed in all SERS spectra and signal for CS mode is higher for 100 mM ionic strength compared to 0 mM.

SERS spectra of 2-naphthalenethiol at 0, 50, and 100 mM ionic strength (Figure 3.2A) shows signals for CH/CS mode and ring stretch mode increases at 100 mM compared to 0 mM ionic strength. Because the peak ratio of 1064 cm^{-1}:1380 cm^{-1} is the same for each spectrum, increase in SERS signal is directly attributed to more 2-naphthalenethiol molecules occupying the SERS-active volume. Similar observations can be made about benzenethiol (Figure 3.2B), 4-mercaptobenzoic acid (Figure 3.2C), and p-aminothiophenol (Figure 3.2D) where the peak ratio of 1074 cm^{-1}:1575 cm^{-1}, 1078 cm^{-1}:1585 cm^{-1}, and 1079 cm^{-1}:1594 cm^{-1} are consistent.

CS stretching vibration for each molecule is used for kinetic studies because CS

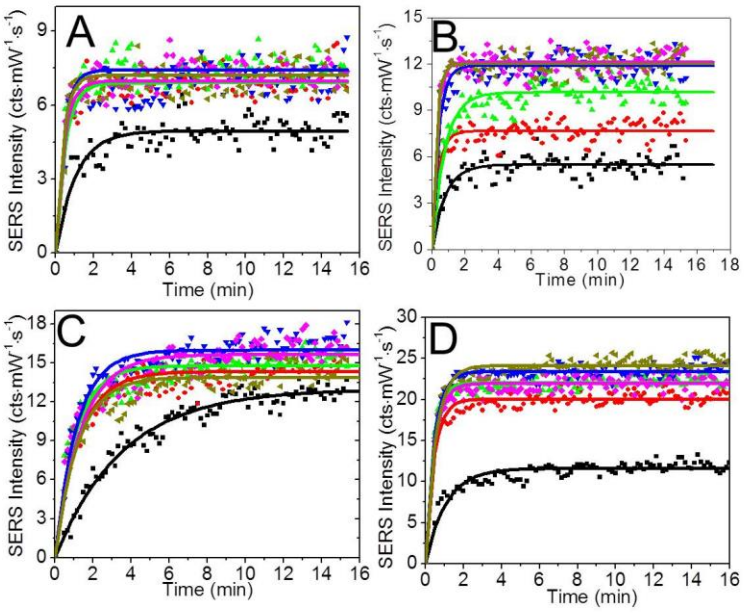

Figure 3.3. Time dependent SERS signals for 10 µM molecular concentration on IE $Ag@Au@SiO_2$ nanoparticles. Temporal profile of (A) 1067 cm^{-1} (CH bend/CS stretch) mode for 2-naphthalenethiol, (B) 1074 cm^{-1} (CS and CC symmetric stretch) mode for benzenethiol, (C) 1078 cm^{-1} (CC ring/CS stretch) for 4-mercaptobenzoic acid, and (D) 1079 cm^{-1} (CS stretch) for p-aminothiophenol. The curves are: black = 0, red = 10, green = 25, blue = 50, magenta = 75, and dark yellow = 100 mM ionic strength. The ionic strength of the solution is adjusted using 100 mM KCl solution. SERS parameters as in Figure 3.2.

stretching is closest to the metal and occurs near perpendicular to the surface so that molecular symmetry and orientation effect on CS stretching mode is assumed minimum. Figure 3.3 (A – D) show SERS temporal profiles fits using equation 3.1 for 1067 cm^{-1}, 1074 cm^{-1}, 1078 cm^{-1}, and 1079 cm^{-1} for 2-naphthalenethiol, benzenethiol, 4-mercaptobenzoic acid, and p-aminothiophenol molecules; respectively as a function of solution ionic strength. Plots indicate that SERS signal initially increases and then saturates as a function of incubation time as no more molecules bind on to Ag@Au surface. In all cases SERS signals saturate within 15 minute incubation time. The tangent in the SERS signal vs. time curves is the slowest for 0 mM KCl added samples for all molecules indicating that molecular diffusion is slower at 0 mM ionic strength. As the solution ionic strength increases, SERS signals increase faster and higher SERS saturation are achieved for 2-naphthalenethiol and benzenethiol molecules. Similar results are observed for 4-mercaptobenzoic acid and p-aminothiophenol; however, slower increase in SERS temporal profile is observed at 100 mM solution ionic strength for these two molecules.

To extract rate constants, the observed SERS temporal profiles for all molecules are fitted with first-order time dependent Langmuir isotherm represented in equation 3.1.[28-29] Figure 3.4 shows SERS rate constant obtained from fitting equation 3.1 to SERS temporal profiles for all molecules studied. The plot shows that rate constant (k) increases from 0 to 25 mM ionic strength (for 2-napthalenethiol, 4-mercaptobenzoic acid, and p-aminothiophenol while rate constant increases from 0 to 50 mM ionic strength for benzenethiol. Beyond these ionic strength values, rate constant either slightly decreases or stabilizes over 100 mM ionic strength. Similar observation in protein transport through

polycarbonate track etched membranes modified with $HSC_{10}H_{20}COOH$ SAM is reported in literature.[24] For example, flux of bovine serum albumin through polycarbonate track etched membranes increased by 40% at pH = pI (4.7) and are attributed to decrease in

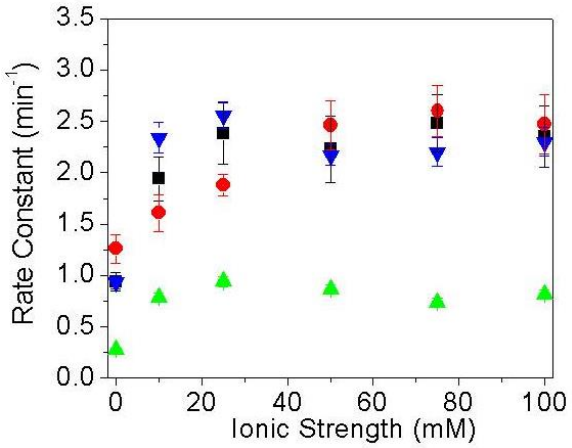

Figure 3.4. Rate constants determined for time dependent SERS signals as a function of solution ionic strength. Data points are: black = 2-naphthalenethiol, red = benzenethiol, green = 4-mercaptobenzoic acid, and blue = p-aminothiophenol. Rate constant increases with increasing solution ionic strength for 2-napthalenethiol, benzenethiol, and 4-mercaptobenzoic acid (except for 100 mM) molecules. Benzenethiol shows increase in rate constant up to 75 mM.

electrical double layer thickness when ionic strength increased from 0 to 100 mM. Other literature indicate that protein transport at a fixed pH is observed to be more pronounced at lower ionic strengths.[30-31] The increase in rate constant values for all molecules with increasing ionic strength (Figure 3.4), therefore, is ascribed to decrease in double layer thickness. The calculated double layer thicknesses are 3.0, 1.9, 1.3, 1.1, and 0.9 nm respectively at 10, 25, 50, 75, and 100 mM solution ionic strength. As the double layer thickness decreases, molecular transport from bulk to the silica increases because molecules only have to overcome smaller potential barrier. Silica at pH 6.5 is negatively

charged at all ionic strengths. Negatively charged 4-mercaptobenzoic acid (pK_a of COOH = 4.8)[32] experiences electrostatic repulsion from negatively charged silica at all ionic strengths, thereby decreasing 4-mercaptobenzoic acid transport and rate constant across silica compared to . neutral benzenethiol or positively charged p-aminothiophenol. Rate constant for p-aminothiophenol transport to the metal core increases up to 25 mM ionic strength and decreases ~12% beyond ionic strength of 25 mM. Rate constants for p-aminothiophenol (at ionic strengths below 25 mM) are higher than other molecules and can be described by electrostatic attraction between the positively charged p-aminothiophenol with the negatively charged silica surface promoting molecular transport across silica. Rate constant decrease for both charged 4-mercaptobenzoic acid and p-aminothiophenol by ~12% at higher solution ionic strength (i.e. > 25 mM) could be a result of electrostatic interactions with the silica surface at double layer thicknesses less than 1.1 nm.

In contrast, distribution of 2-naphthalenethiol and benzenethiol at pH 6.5 as neutral thiol and thiolate is 79/21 because the thiol pK_a is 6.6.[28] Neutral molecules diffuse through silica without any electrostatic interactions (attractive/repulsive), therefore, transport of neutral molecules like 2-naphthalenethiol and benzenethol is only governed by solvent barrier at silica-aqueous interface and diffusion inside silica pores. SERS rate constants for these molecules are higher than negatively charged 4-mercaptobenzoic acid but lower than positively charged p-aminothiophenol. Higher ionic strength greater than 25 mM exhibit minimum impact on rate constants (rate constants are within standard error) which is expected for these neutral molecules diffusing through silica without electrostatic interactions. Although mass transport for benzenethiol is expected to be

higher than 2-napthalenethiol (based on molecular size), higher rate constant for 2-napthalenethiol is observed particularly at ionic strength < 50 mM.

3.3.2 Determination of SERS rate constants as a function of pH

Study of molecular adsorption kinetics through internally etched nanoparticles in solution phase can be complex because solution pH affects protonated/deprotonated state of molecular functional group as well as charge on the silica matrix. To ensure negative

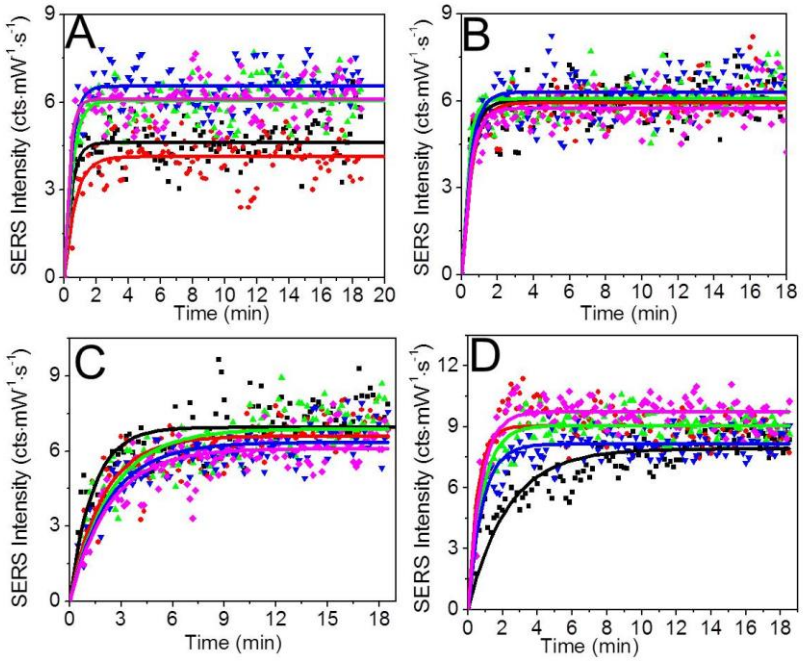

Figure 3.5. Time dependent SERS signals for 10 µM molecular concentration on IE Ag@Au@SiO_2 nanoparticles. Temporal profile of (A) 1067 cm^{-1} (CH bend/CS stretch) mode for 2-naphthalenethiol, (B) 1074 cm^{-1} (CS and CC symmetric stretch) mode for benzenethiol, (C) 1078 cm^{-1} (CC ring/CS stretch) for 4-mercaptobenzoic acid, and (D) 1079 cm^{-1} (CS stretch) for p-aminothiophenol molecules. The curves are: black = 4.0, red = 5.5, green = 6.6, blue = 7.5, and magenta = 9.0 pH solutions. SERS parameters as in Figure 3.2.

charge on the silica surface, all the pH experiments are done above pH 4.0. The reported pK_a of thiol dissociation at room temperature is 6.6.[28] pK_a of amine and carboxylic acid functional groups are 8.7 and 4.9.[32] Therefore, changing the pH from 4 – 9 should change the molecular charge and the dynamics of mass transport. A 40% increase in relative limiting current associated with transport of $Ru(NH_3)_6^{3+}$ ions through sulfonated silica colloidal films have been reported when solution pH changed from 4.0 to 9.0.[26] Similarly, examples of 3 to 4 fold increase in protein flux through porous membranes by tuning solution pH are also reported.[23-25]

To study how solution pH affect kinetic rate constants for SERS, 6 nM IE $Ag@Au@SiO_2$ nanoparticles are suspended in pH 4.0, 5.5, 6.6, 7.5, and 9.0 solution and 10 μM 2-naphthalenethiol, benzenethiol, 4-mercaptobenzoic acid, and p-aminothiophenol molecules are added separately. Solutions are vortexed for 3 seconds and SERS data collected using 632.8 nm Raman excitation. SERS temporal profiles for each molecule at various pH conditions are shown in Figure 3.5. 2-Naphthalenethiol (Figure 3.5A) shows that maximum saturated SERS signal increases for pH 6.6 where the distribution of neutral/thiolate form is 50:50. At pH 4 and 5.5, saturated SERS for 2-naphthalenethiol is nearly half compared to pH 6.6 indicating that total number of molecules occupying 3D SERS volume is nearly half. The decrease in 2-naphthalenethiol saturated SERS signal at pH 5.5 or below is attributed to molecular di-thiol bond formations which literature indicate occurs maximum at ~5.0 pH where both neutral and anionic thiolated forms are present.[33] Yoon and co-workers in the same article show that di-thiol formation is a photooxidation reaction (excitation wavelength dependent) and at 632.8 nm Raman excitation, only 20 – 30% of thiolated molecules undergo di-thiol

formation which could explain ~30% decrease in SERS signals at pH < 5.5 compared to other pH values (Figure 3.5A). As di-thiol bonds form, the overall molecular size of 2-naphthalenethiol exceeds diameter of micropores (< 2 nm) hindering mass transport to the Ag@Au core. SERS temporal profile for benzenethiol (Figure 3.5B) at various solution pHs show saturated SERS signals ~constant at all pH values indicating that benzenethiol transport across silica and SERS signals are minimally affected by pH. It appears that either the size of the molecule due to di-thiol formation at pH <5.5 are smaller than the silica pores or the two benzene rings re-orient to lower the energy barrier for passage through the silica pores as reported for benzene derivatives through zeolite micropores.[34] Choudhary and Akolekar used shuttlecock-shuttlebox model for explaining the implication of molecular configuration and flexibility over size in sorption/diffusion of benzene derivatives through similar pore size zeolite by hypothesizing that diffusion and/or potential gradient across the bulk solution-zeolite interface can overcome surface and pore mass transfer resistances allowing molecules to re-configure for transport through the pores.[34-35] Molecular transport of benzenethiol derivatives with di-thiol bonds through silica is expected to be facilitated by molecular re-orientation; however, rate constant will be smaller because the molecules need to overcome energy barrier associated to re-orientation inside silica pores.

Figure 3.5C shows higher saturated SERS signal at pH 4.0 for 4-mercaptobenzoic acid when the carboxylic acid is protonated and neutral so that transport is achieved

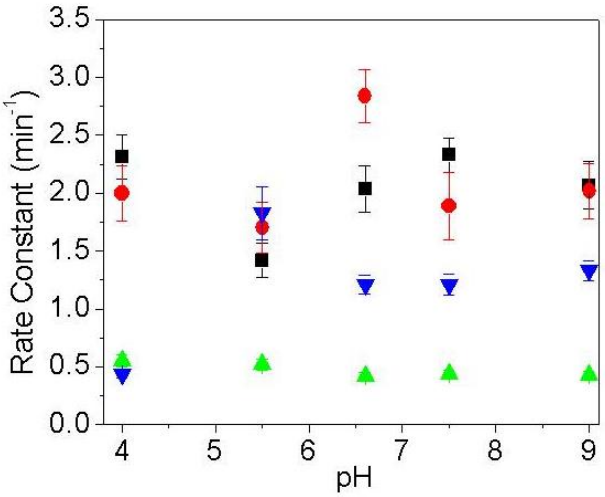

Figure 3.6. Rate constants determined for time dependent SERS signals as a function of solution pH. Data points are: black = 2-naphthalenethiol, red = benzenethiol, green = 4-mercaptobenzoic acid, and blue = p-aminothiophenol. Maximum rate constants are observed at pH 7.6, 6.6, 5.5, and 4.0 for 2-naphthalenethiol, benzenethiol, 4-mercaptobenzoic acid, and p-aminothiophenol, respectively.

without electrostatic interactions. As solution pH increases, carboxylic acid gets deprotonated and negatively charge so that the molecule experiences electrostatic repulsion with silica surface hindering molecular transport to the metal core. In contrast, saturated SERS signal is highest at pH 9.0 for p-aminothiophenol when the solution pH is closer to the pK_a of anime functional group. As the solution pH decreases, protonation of amine group increases overall positive charge on the molecule that can electrostatically interacts with the negatively charge silica and decrease p-aminothiophenol transport at lower solution pH (Figure 3.5D). Results imply that molecular transport is mainly

affected by pK_a for charged molecules like 4- mercaptobenzoic acid and p-aminothiophenol; and di-thiol formation for bigger 2-naphthalenethiol.

SERS kinetic rate constants (Figure 3.6) determined by fitting temporal profiles with equation 3.1 shows that the rate constant for 2-naphthalenethiol is nearly constant except at pH 5.5 where di-thiol formation is expected to can occur. SERS rate constant for benzenethiol is maximum at pH 6.6 (~ pK_a) where thiol:thiolate form is 50:50 so that transport of neutral molecules through silica occur at faster rate. Slower rate constant for benzenethiol at pH 5.5 can be attributed to possible slow transport of di-thiol form through silica pores. Rate constant for SERS slightly decreases for 4-mercaptobenzoic acid as the pH increases because of electrostatic repulsion between negatively charged molecules and silica. It was expected that rate constant for p-aminothiophenol would be similar at pH 4 and 5.5 because in both solution conditions > 90% molecules are positively charge and should exhibit similar rate constants; however, rate constant for p-aminothiophenol at pH 4 is unexpectedly lower than pH 5.5. Because the zeta potential of silica colloids decreases by half at pH 4 vs. pH 5.5,[26] the decrease in rate constant at pH 4 is attributed to less electrostatic attraction between silica and positively charged p-aminothiophenol molecules. Similar observations where decrease in bovine serum albumin flux at pH < pI and increase in flux at pH > pI is reported in literature for transport studies in negatively charged membrane pores indicating that electrostatic interactions between molecule and membrane at various pH values plays a huge role in transport and rates.[23-24]

3.3.3 Determination of SERS rate constants as a function of polarity

In addition to solution ionic strength and pH affect in molecular transport, solvent polarity also influence molecular diffusion and transport by affecting molecular solubility or partitioning between solution-silica interfaces. Changes in bulk molecular solubility for 10 µM 2-naphthalenethiol, benzenethiol, 4-mercaptobenzoic acid, or p-

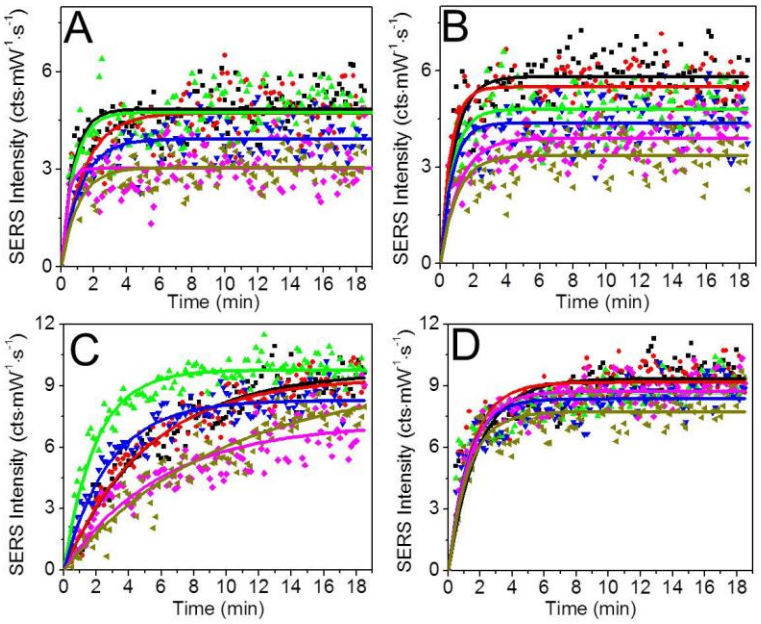

Figure 3.7. Time dependent SERS signals for 10 µM molecular concentration on IE Ag@Au@SiO_2 nanoparticles. Temporal profile of (A) 1067 cm^{-1} (CH bend/CS stretch) mode for 2-naphthalenethiol, (B) 1074 cm^{-1} (CS and CC symmetric stretch) mode for benzenethiol, (C) 1078 cm^{-1} (CC ring/CS stretch) for 4-mercaptobenzoic acid, and (D) 1079 cm^{-1} (CS stretch) for p-aminothiophenol molecules. The curves are: black = 0, red = 5, green = 10, blue = 15, magenta = 20, and dark yellow = 25% MeOH in samples. The polarity of the solution is adjusted using dehydrated MeOH. SERS temporal curve indicate that maximum saturated SERS signals are observed at between 0 – 10% MeOH. SERS parameters as in Figure 3.2.

aminothiophenol by changing MeOH composition from 0 to 25% is expected to be negligible because the concentration of molecules used is at least 4 times below the

solubility limit. Molecular partitioning, therefore, influences transport through silica pores. To study the implication of solution polarity on SERS kinetic rates, 6 nM IE $Ag@Au@SiO_2$ nanoparticles are suspended in 0, 5, 10, 15, 20, and 25% MeOH solutions at pH 6.5 phosphate buffer. 10 μM 2-naphthalenethiol, benzenethiol, 4-mercaptobenzoic acid, and p-aminothiophenol molecules are added separately, vortexed for 3 seconds and SERS data collected using 632.8 nm laser. From SERS temporal profile (Figure 3.7A), it is observed that decreasing solution polarity from 9 (0% MeOH) to 8.1 (10% MeOH) have no influence in saturated SERS signals for 2-naphthalenethiol. Beyond polarity of 8.1 (10% MeOH), saturated SERS signal systematically decreases. Decreasing saturated SERS signal at lower solution polarity for 2-naphthalenethiol is attributed to decrease in molecular partitioning between silica-solution interface. As solution polarity decrease, partitioning of small organic molecule in solution phase increases, hindering molecular transport through hydrophilic silica pores. Similar observation is made for benzenethiol and p-aminothiophenol where saturated SERS is maximum at higher solution polarity (i.e. 0% MeOH). In contrast, 4-mercaptobenzoic acid exhibit higher saturated SERS at solution polarity values 9.0 – 8.55 (0 – 10% MeOH).

Rate constants calculated from SERS temporal curves (Figure 3.8) indicate that rate constants for all the molecules are minimum at solution polarity of 6.3 (25% MeOH). Maximum rate constant occurs at solution polarity of 8.55 (5% MeOH) for neutral 2-naphthalenethiol and benzenethiol molecules while for charged 4-mercaptobenzoic acid and p-aminothiophenol, maximum rate constant associated with SERS occurs at 8.1 polarity (10% MeOH). Decrease in molecular partitioning across silica-solution interface decreases rate constants at lower polarity. These observations can be rationalized by

looking at the partition coefficients. For example, log partition coefficient (log(P)) values of naphthalene (similar to 2-naphthalenethiol), benzene, benzoic acid, and benzenethiol

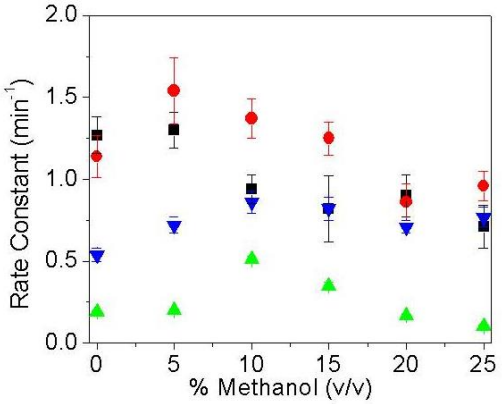

Figure 3.8. Rate constants determined for time dependent SERS signals as a function of solution polarity. Data points are: black = 2-naphthalenethiol, red = benzenethiol, green = 4-mercaptobenzoic acid, and blue = p-aminothiophenol. Rate constant increases up to 5% MeOH for 2-napthalenethiol and thiophenol. Maximum rate constant value is observed at 10% MeOH for charged molecules such as 4-mercaptobenzoic acid and p- aminothiophenol.

in octanol-water system are 3.35, 2.13, 1.87, and 2.52, respectively.[36] Octanol-water partition coefficient determines the ratio of molecules in organic to aqueous phase. Higher log(P) values indicate that molecular solubility in organic phase is higher and, therefore, molecule is non-polar. Log(P) values listed above indicate that addition of (1) benzene ring (i.e. benzene vs. naphthalene) increases partitioning, (2) charged functional group (benzene vs. benzoic acid) decreases partitioning, and (3) thiol functional group

(benzene vs. benzenethiol) increase partitioning. Decreasing solution polarity decreases saturated SERS signals for all molecules (2-naphthalenethiol, benzenethiol, 4-mercaptobenzoic acid, and p-aminothiophenol) because molecules partitioning from

Table 3.1. SERS rate constants (min^{-1}) for various solution conditions.

Ionic strength (mM)	0	10	25	50	75	100
2-naphthalenethiol	0.9 ± 0.1	1.9 ± 0.2	2.4 ± 0.3	2.2 ± 0.3	2.5 ± 0.3	2.35 ± 0.3
benzenethiol	1.3 ± 0.1	1.6 ± 0.2	1.9 ± 0.1	2.5 ± 0.2	2.6 ± 0.2	2.5 ± 0.3
4-mercaptobenzoic acid	0.3 ± 0.0_1	0.8 ± 0.0_4	0.9 ± 0.0_5	0.9 ± 0.0_4	0.7 ± 0.0_4	0.8 ± 0.0_4
p-aminothiophenol	0.9 ± 0.1	2.3 ± 0.1	2.6 ± 0.1	2.2 ± 0.1	2.2 ± 0.1	2.3 ± 0.1
pH	4.0	5.5	6.5	7.5	9.0	
2-naphthalenethiol	2.3 ± 0.2	1.4 ± 0.1	2.0 ± 0.2	2.3 ± 0.1	2.1 ± 0.2	
benzenethiol	2.0 ± 0.2	1.7 ± 0.2	2.8 ± 0.2	1.9 ± 0.3	2.0 ± 0.2	
4-mercaptobenzoic acid	0.6 ± 0.0_5	0.5 ± 0.0_5	0.4 ± 0.0_3	0.4 ± 0.0_3	0.4 ± 0.0_3	
p-aminothiophenol	0.4 ± 0.0_3	1.8 ± 0.2	1.2 ± 0.1	1.2 ± 0.1	1.3 ± 0.1	
Polarity	9.0	8.5_5	8.1	7.6_5	7.2	6.3
2-naphthalenethiol	1.3 ± 0.1	1.3 ± 0.1	0.9 ± 0.1	0.8 ± 0.2	0.9 ± 0.1	0.7 ± 0.1
benzenethiol	1.1 ± 0.1	1.5 ± 0.2	1.4 ± 0.1	1.2 ± 0.1	0.9 ± 0.1	1.0 ± 0.1
4-mercaptobenzoic acid	0.2 ± 0.0_1	0.2 ± 0.0_1	0.5 ± 0.0_2	0.3 ± 0.0_2	0.2 ± 0.0_1	0.1 ± 0.0_1
p-aminothiophenol	0.5 ± 0.0_4	0.7 ± 0.0_5	0.9 ± 0.1	0.8 ± 0.1	0.7 ± 0.0_4	0.8 ± 0.1

MeOH-water phase to hydrophilic silica decreases. Study by Bahrami and coworkers shows that increasing MeOH% in MeOH-water mobile phase decreased HPLC retention time for benzene using reverse phase C-18 column indicating partitioning of organic molecule in solvent increases with decreasing solvent polarity.[37] Finally SERS rate constant calculated as a function of solution ionic strength, pH, and polarity are summarized in Table 3.1.

3.3.5 Conclusion

In summary, molecular transport of 2-naphthalenethiol, benzenethiol, 4-mercaptobenzoic acid, and p-aminothiophenol molecules through silica matrix were studies as a function of solution ionic strength, pH, and polarity. SERS temporal profiles were generated and evaluated using first order time dependent Langmuir isotherm model. Analysis of SERS rate constants as a function of ionic strength showed that increasing ionic strength up to 25 mM increased SERS rate constants and higher saturated SERS signal were observed. Higher rate constant as a function of increasing ionic strength is attributed to decrease in double layer thickness and electrostatic interactions with silica. Changing solution pH changed molecular charge that either promoted or hindered molecular transport. Kinetic rate constants were highest at pH 7.5, 6.6, 4, and 5.5 for 2-naphthalenethiol, benzenethiol, 4-mercaptobenzoic acid, and p-aminothiophenol. Also decrease in transport and rate constant for 2-naphthalenethiol at pH 5.5 is attributed to possible di-thiol formation which increased molecular size and hindered transport of 2-naphthalenethol through silica pores. Di-thiol formation can also occur for benzenethiol, 4-mercaptobenzoic acid, and p-aminothiophenol; however, no significant decrease in saturated SERS signals were observed at pH 5.5 indicating that the size of the di-thiol form are smaller than silica pores and/or re-orientation of benzene rings occurs to lower resistance to molecular transport as established in literature for various benzene derivatives through zeolite micropores. In addition, SERS rate constants were observed to be highest at 5% MeOH for 2-naphthalenethiol and benzenethiol. In contrast, highest SERS rate constant at 10% MeOH was observed for 4-mercaptobenzoic acid and p-aminothiophenol. These results indicate that solution ionic strength, pH, and polarity play

important role in molecular transport and should be considered for SERS studies. Changing these solution parameters can allow selective molecular detection by modulating transport to the metal surface that dictates rate constant for a specific molecule compared to other molecules in a complex sample.

1. Roca, M.; Haes, A. J., Silica-Void-Gold Nanoparticles: Temporally Stable Surf Ace-Enhanced Raman Scattering Substrates. *J. Am. Chem. Soc.* **2008**, *130*, 14273-14279.
2. Pierre, M. C. S.; Haes Amanda, J., Purification Implications on Sers Activity of Silica Coated Gold Nanospheres. *Anal Chem* **2012**, *84*, 7906-7911.
3. Pierre, M. C. S.; Mackie, P. M.; Roca, M.; Haes, A. J., Correlating Molecular Surface Coverage and Solution-Phase Nanoparticle Concentration to Surface-Enhanced Raman Scattering Intensities. *The Journal of Physical Chemistry C* **2011**, *115*, 18511–18517.
4. Volkert, A. A.; Pierre, M. C. S.; Shrestha, B.; Haes, A. J., Implications of Sample Aging on the Formation of Internally Etched Silica Coated Gold Nanoparticles. *RSC Advances* **2015**, *5*, 3774-3780.
5. Jin, R.; Cao, Y. W.; Mirkin, C. A.; Kelly, K. L.; Schatz, G. C.; Zheng, J. G., Photoinduced Conversion of Silver Nanospheres to Nanoprisms. *Science* **2001**, *294*, 1901-1903.
6. Lee, K.-S.; El-Sayed, M. A., Gold and Silver Nanoparticles in Sensing and Imaging: Sensitivity of Plasmon Response to Size, Shape, and Metal Composition. *The Journal of Physical Chemistry B* **2006**, *110*, 19220-19225.
7. Roca, M.; Mackie, P. M.; Haes, A. J., Design of a Biocompatible and Optically-Stable Solution-Phase Substrate for Sers Detection. *Mat. Res. Soc. Symp. Proc.* **2009**, *1133*, AA09-02.
8. Jeanmaire, D. L.; Van Duyne, R. P., Surface Raman Spectroelectrochemistry. Part I. Heterocyclic, Aromatic, and Aliphatic Amines Adsorbed on the Anodized Silver Electrode. *J. Electroanal. Chem. & Interfac. Electrochem.* **1977**, *84*, 1-20.
9. Fang, P.; Li, J. F.; Yang, Z.; Li, L. M.; Ren, B.; Tian, Z., Optimization of Sers Activities of Gold Nanoparticles and Gold-Core–Palladium-Shell Nanoparticles by Controlling Size and Shell Thickness. *J. Raman Spect.* **2008**, *39*, 1679-1687.
10. Zhang, Q.; Zhang, T.; Ge, J.; Yin, Y., Permeable Silica Shell through Surface-Protected Etching. *Nano Lett.* **2008**, *8*, 2867-2871.
11. Liz-Marzan, L. M.; Giersig, M.; Mulvaney, P., Synthesis of Nanosized Gold-Silica Core-Shell Particles. *Langmuir* **1996**, *12*, 4329-4335.
12. Lu, Y.; Yin, Y.; Mayers, B. T.; Xia, Y., Modifying the Surface Properties of Superparamagnetic Iron Oxide Nanoparticles through a Sol−Gel Approach. *Nano Lett.* **2002**, *2*, 183-186.
13. Karger, J.; Ruthven, D. M., *Diffusion in Zeolites*, 1 ed.; John Wiley & Sons, INC.: New York, 1992.
14. De Angelis, F., et al., Breaking the Diffusion Limit with Super-Hydrophobic Delivery of Molecules to Plasmonic Nanofocusing Sers Structures. *Nat Photon* **2011**, *5*, 682-687.
15. Li, L.; Hutter, T.; Steiner, U.; Mahajan, S., Single Molecule Sers and Detection of Biomolecules with a Single Gold Nanoparticle on a Mirror Junction. *Analyst* **2013**, *138*, 4574-4578.

16. Liu, H.; Zhang, L.; Lang, X.; Yamaguchi, Y.; Iwasaki, H.; Inouye, Y.; Xue, Q.; Chen, M., Single Molecule Detection from a Large-Scale Sers-Active Au79ag21 Substrate. *Sci. Rep.* **2011**, *1*.
17. Srnova-Sloufova, I.; Vlckova, B.; Bastl, Z.; Hasslett, T. L., Bimetallic (Ag)Au Nanoparticles Prepared by the Seed Growth Method: Two-Dimensional Assembling, Characterization by Energy Dispersive X-Ray Analysis, X-Ray Photoelectron Spectroscopy, and Surface Enhanced Raman Spectroscopy, and Proposed Mechanism of Growth. *Langmuir* **2004**, *20*, 3407-3415.
18. Cui, Y.; Ren, B.; Yao, J.-L.; Gu, R.-A.; Tian, Z.-Q., Synthesis of Agcoreaushell Bimetallic Nanoparticles for Immunoassay Based on Surface-Enhanced Raman Spectroscopy. *The Journal of Physical Chemistry B* **2006**, *110*, 4002-4006.
19. Paramelle, D.; Sadovoy, A.; Gorelik, S.; Free, P.; Hobley, J.; Fernig, D. G., A Rapid Method to Estimate the Concentration of Citrate Capped Silver Nanoparticles from Uv-Visible Light Spectra. *Analyst* **2014**, *139*, 4855-4861.
20. Roca, M.; Mackie, P. M.; Haes, A. J., Design of a Biocompatible and Optically-Stable Solution-Phase Substrate for Sers Detection. *Mater. Res. Soc. Symp. Proc.* **2008**, *1133E*, No pp given.
21. Stober, W.; Finx, A.; Bohn, E., Controlled Growth of Monodisperse Silica Spheres
in the Micron Size Range. *J. Coll. Interface Sci.* **1968**, *26*, 62.
22. Grzelczak, M.; Correa-Duarte, M. A.; Liz-Marzan, L. M., Carbon Nanotubes Encapsulated in Wormlike Hollow Silica Shells. *Small* **2006**, *2*, 1174-1177.
23. Ku, J. R.; Stroeve, P., Protein Diffusion in Charged Nanotubes: "On-Off"' Behavior of Molecular Transport. *Langmuir* **2004**, *20*, 2030-2.
24. Chun, K.-Y.; Stroeve, P., Protein Transport in Nanoporous Membranes Modified with Self-Assembled Monolayers of Functionalized Thiols. *Langmuir* **2002**, *18*, 4653-4658.
25. Qiu, X.; Yu, H.; Karunakaran, M.; Pradeep, N.; Nunes, S. P.; Peinemann, K.-V., Selective Separation of Similarly Sized Proteins with Tunable Nanoporous Block Copolymer Membranes. *ACS Nano* **2013**, *7*, 768-776.
26. Smith, J. J.; Zharov, I., Ion Transport in Sulfonated Nanoporous Colloidal Films. *Langmuir* **2008**, *24*, 2650-2654.
27. Zharov, I.; Khabibullin, A., Surface-Modified Silica Colloidal Crystals: Nanoporous Films and Membranes with Controlled Ionic and Molecular Transport. *Acc. Chem. Res.* **2014**, *47*, 440-449.
28. Tripathi, A.; Emmons, E. D.; Christesen, S. D.; Fountain, A. W.; Guicheteau, J. A., Kinetics and Reaction Mechanisms of Thiophenol Adsorption on Gold Studied by Surface-Enhanced Raman Spectroscopy. *The Journal of Physical Chemistry C* **2013**, *117*, 22834-22842.
29. Islam, A.; Khan, M. R.; Mozumder, S. I., Adsorption Equilibrium and Adsorption Kinetics: A Unified Approach. *Chem. Eng. Technol* **2004**, *27*, 1095-1098.
30. van Eijndhoven, R. H. C. M.; Saksena, S.; Zydney, A. L., Protein Fractionation Using Electrostatic Interactions in Membranel Filtration. *Biotech. Bioeng.* **1995**, *48*, 406-414.
31. Ghosh, R.; Cui, Z. F., Fractionation of Bsa and Lysozyme Using Ultrafiltration: Effect of Ph and Membrane Pretreatment. *Journal of Membrane Science* **1998**, *139*, 17-28.
32. Hiramatsu, H.; Osterloh, F. E., Ph-Controlled Assembly and Disassembly of Electrostatically Linked Cdse−Sio2 and Au−Sio2 Nanoparticle Clusters. *Langmuir* **2003**, *19*, 7003-7011.
33. Kim, H. J.; Yoon, J. H.; Yoon, S., Photooxidative Coupling of Thiophenol Derivatives to Disulfides. *The Journal of Physical Chemistry A* **2010**, *114*, 12010-12015.

34. Choudhary, V. R.; Nayak, V. S.; Choudhary, T. V., Single-Component Sorption/Diffusion of Cyclic Compounds from Their Bulk Liquid Phase in H-Zsm-5 Zeolite. *Industrial & Engineering Chemistry Research* **1997**, *36*, 1812-1818.
35. Choudhary, V. R.; Akolekar, D. B., Shuttlecock-Shuttlebox Model for Shape Selectivity of Medium-Pore Zeolites in Sorption and Diffusion. *Journal of Catalysis* **1989**, *117*, 542-548.
36. Sangster, J., Octanol-Water Partition Coefficients of Simple Organic Compounds. *Journal of Physical and Chemical Reference Data* **1989**, *18*, 1111-1229.
37. Bahrami, A.; Mahjub, H.; Sadeghian, M.; Golbabaei, F., Determination of Benzene, Toluene and Xylene (Btx) Concentrations in Air Using Hplc Developed Method Compared to Gas Chromatography. *International Journal of Occupational Hygiene* **2011**, *3*, 12-17.

CHAPTER 4 QUANTITATIVE AND REPRODUCIBLE SERS DETECTION USING SILICA MEMBRANE DENSITY CONTROL ON GOLD COATED SILVER NANOPARTICLES

4.1 Introduction

Metal nanoparticles exhibit localized surface plasmon resonance (LSPR) spectra, which can be exploited for molecular detection using surface-enhanced Raman scattering (SERS) [1-4]. SERS can be performed with either bottom-up or top-down synthetic strategies. While top-down prepared SERS substrates can exhibit a high degree of spatial reproducibility, limitations of mass transport during an assay for trace molecules can increase detection time additionally beyond those required for building up a detectable molecular concentration. In contrast, bottom-up prepared nanomaterials can be synthesized in large scales at a relatively low cost and exhibit ~1000x greater mass transport of small molecules vs. top-down SERS materials. As such, bottom-up prepared SERS-active nanomaterials, which are widely availability, easy to synthesize, and easy to structurally tune provide ideal platforms for studying impacts of surface chemistry on the magnitude of SERS signals.

Both bottom-up and top down SERS substrates induce the SERS phenomenon, which relies on at least two mechanisms for molecular detection [5-15]. The largest SERS enhancement factor depends on the LSPR spectra of the nanostructured substrate, which gives rise to strong electromagnetic fields that extend several nanometers away from its surface [6, 8-16]. The second contribution is a short range chemical effect, which arises from

[1] Adapted from *Improving Surface Enhanced Signal Reproducibility using Gold-coated Silver Nanospheres Encapsulated in Silica Membranes*, Binaya K. Shrestha and Amanda J. Haes, J. Opt, In Press. **2015**.

the electronic coupling of, charge transfer between, and adsorption of a molecule on a nanostructure [17-19]. Both mechanisms are hypothesized to broaden the molecular orbitals, which subsequently can overlap with the LSPR of the nanostructures [20-22].

For these mechanisms to result in detectable average SERS signals, molecules must diffuse toward the plasmonic nanostructured surface and interact at short metal to molecule separation distances. Surface functionalization can be used to promote selective interactions between molecules and the nanostructured surface at these length scales. For instance, molecular adsorption can be promoted using specific surface chemistry, which facilitates binding and detection [23]. Silica, for instance, is a structurally versatile, biocompatible, and optically transparent protective material which can be subsequently modified with a variety of different chemical functionalities. If these layers are porous, target molecules can interact with the metal through the porous regions of this layer and be detected using SERS [2].

Previously, bottom-up synthesized internally etched silica coated gold nanoparticles were used as SERS substrates for the direct and quantitative detection of molecules [1, 4, 24]. Modest signal enhancements were observed from these materials and were facilitated by the formation of internal voids in the silica membrane near the metal nanoparticle core, which facilitated molecular diffusion [1]. Furthermore, the silica membranes were shown to also maintain the electromagnetic properties of the nanoparticle even when nanoparticle aggregation occurred. In a separate study, SERS substrates were prepared so that controlled three dimensional volumes where SERS activity was maximized were designed [25]. The three dimensional SERS volumes were defined as the focal volumes associated with optimal optical scattering. Maximizing the

number of scattered photons generated in these volumes was shown to increase SERS signals [25-26] and lower limits of detection for small molecules [25, 27-29].

Herein, internally etched silica membrane stabilized gold coated silver ($Ag@Au@SiO_2$) nanospheres with well characterized morphologies and silica properties are synthesized to better understand how internal void volumes and effective local refractive index impact the reproducibility of SERS signals for 4-aminothiophenol. Transmission electron microscopy (TEM), LSPR spectroscopy and dielectric modeling are used to estimate effective local refractive indices. The resulting silica membranes are used to systematically vary the three-dimensional SERS volumes near the surface of Ag@Au nanoparticles, and 4-aminothiophenol is used to evaluate how SERS signals vary as a function of effective refractive index as well as molecular and nanoparticle concentrations. By exploiting the effective refractive index surrounding internally etched $Ag@Au@SiO_2$ nanoparticles, quantitative and reproducible SERS detection is achieved.

4.2 Experimental Materials and Methods

4.2.1 Chemical Reagents

Gold(III) chloride trihydrate, sodium citrate dihydrate, Amberlite MB-150 mixed bed exchange resin, (3-aminopropyl) trimethoxysilane (APTMS), sodium chloride (NaCl), sodium trisilicate (27%), tetraethyl orthosilicate (TEOS), silver perchlorate, sodium borohydride, and hydroxylamine hydrochloride were purchased from Sigma. Ethanol, ammonium hydroxide (NH_4OH), hydrochloric acid (HCl), and nitric acid (HNO_3) were purchased from Fisher Scientific (Pittsburgh, PA). Ultrapure water (18.2 $M\Omega\ cm^{-1}$) was obtained from a Barnstead Nanopure System and used for all experiments. All glassware items were cleaned with aqua regia (3:1 HCl/ HNO_3) and rinsed thoroughly with water,

and oven (glass) or air (plastic) dried overnight before use.

4.2.2 Silver@Gold Nanoparticle Synthesis

Ag@Au nanoparticles were synthesized using a seeded growth method previously described in the literature [30-31]. Briefly, 100 mL of a 0.3 mM sodium citrate solution prepared in nitrogen-purged water was stirred on an ice bath in the dark. Freshly prepared sodium borohydride (final concentration = 1 mM) was added to the citrate solution. Next, 1 mL of 10 mM silver perchlorate was added to the solution within 2 minutes, and the resulting silver nanoparticle solution was stirred for 3 minutes. Stirring was stopped, and silver nanoparticles with average diameters of 11.5 ± 3.2 nm formed within 3 hours. Next, 20 mL of water was added to 25 mL of as-synthesized Ag seeds and stirred for ~2 minutes (4 °C). Fifteen mL of both 6.25 mM hydroxylamine hydrochloride and 0.465 mM gold salt were added slowly (3 mL/min) using syringe pump. This Ag@Au nanoparticle solution was stirred for 1 hour to ensure nanoparticle formation and stored at 2 – 4 °C until use. The concentration of these materials was estimated using a standard estimation model for the silver seeds [32], and an average diameter of 18.5 ± 2.3 nm was determined using TEM.

4.2.3 Microporous Silica-Coated Ag@Au Nanoparticles Synthesis

Silica shells on Ag@Au ($Ag@Au@SiO_2$) nanoparticles were synthesized via a modified Stöber method [24, 33-35]. Briefly, the pH and conductivity of 25 mL of the as synthesized Ag@Au nanoparticles were adjusted to 5 and ~110 µS/cm using NH_4OH and Amberlite resin, respectively. After resin removal via filtration, 129.2 µL of 1 mM APTMS was added drop-wise to the nanoparticle solution (with stirring). After 30

minutes, 201 µL of 2.7% sodium silicate was added slowly to the solution and stirred for 24 hours. The silica shell thickness was further increased by adding ethanol (final ratio of 1 part water to 4.4 parts ethanol). After 6 hours, 20 µL of 1 mM APTMS and 20 µL TEOS were added. The pH of the solution was increased to ~11 using concentrated ammonium hydroxide. After 16 hours, the Ag@Au@SiO_2 nanoparticles were centrifuged (45 minutes, 9383xg) three times with ethanol then three times with water. The Ag@Au@SiO_2 nanoparticles were then passed through Sephadex-50 column to remove Ag@Au nanoparticles that did not contain complete silica shells [2] and stored in ethanol until use. These samples exhibited average diameters of 48.7 ± 6.4 nm with an average silica shell thickness of 15.1 ± 6.8 nm.

4.2.4 Internally Etched Silica-Coated Silver@Gold Nanoparticle Synthesis

Silica shells were converted into silica membranes via an internal silica etching process induced at basic pH values. Because the Ag@Au@SiO_2 nanoparticles were stored in ethanol, the samples were triply centrifuged and redispersed in water to a concentration of 3 nM. Concentrated NH_4OH was added to the solution to induce internal etching [1, 24]. The reaction was quenched by adding 100 mM HNO_3 until the solution pH was ~6. Finally, the nanoparticles were washed 3 times in water and passed through a Sephadex-G50 column to remove defect particles. These samples exhibited average diameters of 46.1 ± 6.0 nm with an average silica shell thickness of 13.8 ± 6.5 nm.

4.2.5 Extinction and SERS Spectroscopies

LSPR spectra were collected using disposable methacrylate cuvettes (pathlength = 1 cm) and an ultraviolet-visible (UV-vis) spectrometer (Ocean Optics USB4000). Either

deuterium or halogen lamps were used for UV and visible excitation, respectively. LSPR spectra were collected in transmission geometry every minute for 2 hours (integration time = 60 msec, average = 25 scans, and boxcar = 10), and extinction maximum wavelengths (λ_{max}) were determined from the zero-point crossing of the first derivative. SERS spectra were collected simultaneous to the LSPR measurements at a 90° angle from the UV-vis light sources. SERS measurements were performed using 6 nM Ag@Au@SiO_2 nanoparticle solutions prepared in 10 mM phosphate buffer (pH 7.4) and 4-aminothiophenol. Prior to SERS measurements, samples were mixed and incubated for at least 1 hour. SERS data were collected using a BW Tek iRaman spectrometer with an excitation wavelength (λ_{ex}) of 785 nm. Blank spectra were collected using cuvettes containing everything but analyte. All SERS spectra shown represent sample data minus these blank spectra.

4.2.6 Transmission Electron Microscopy (TEM)

TEM was performed using a JEOL JEM-1230 microscope equipped with a Gatan CCD camera. Samples were prepared on 400 mesh copper grids that were coated with a thin film of Formvar and carbon (Ted Pella). The nanoparticle solution was diluted in a 50% water−ethanol mixture, and ~10 μL of the solutions were pipetted onto grids and dried. At least 200 nanoparticles were analyzed (Image Pro Analyzer) to estimate average nanoparticle diameters, and average silica shell thicknesses were determined by calculating the differences between Ag@Au and Ag@Au@SiO_2 nanoparticle diameters (error is from propagated error in these measurements).

4.3 Results and Discussion

4.3.1 Evaluating the Optical and Dielectric Properties of Ag@Au and Ag@Au@SiO_2 Nanoparticles

Improvements in the direct SERS detection of target molecules using various silver or gold nanoparticles is well-established in the literature [36-45], and plasmonic solution-phase nanomaterials are widely used as SERS substrates because of their tunable LSPR and inherent structural properties (*i.e.*, radius of curvature, shape and size tunability, *etc.*) [25, 46-47]. Ag@Au nanoparticles are selected as SERS substrates given their increased SERS activity relative to Au nanoparticles, greater dielectric sensitivity vs. Au nanoparticles (*vide infra*), and superior chemical stability versus Ag nanoparticles [48]. Example TEM images of some Ag@Au solution-phase SERS substrates is shown in Figure 4.1A. For instance, Ag nanoparticles (diameter, d = 11.5 ± 3.2 nm) are coated in a thin Au shell (thickness = 3.5 ± 3.9 nm) to promote larger SERS intensities versus yet promote improved chemical stability in basic conditions from the Ag cores. These materials can be stabilized in silica shells to provide controlled electromagnetic coupling between nanostructures. The sample shown in Figure 4.1A-2 represents Ag@Au@SiO_2 nanoparticles (total diameter = 48.7 ± 6.8 nm, silica shell thickness = 15.1 ± 6.8 nm). These samples can be converted into internally etched Ag@Au@SiO_2 nanoparticles (Figure 4.1A-3, total diameter = 46.1 ± 6.0 nm with an average silica thickness of 13.8 ± 6.5 nm).

Importantly, satisfying both the chemical and electromagnetic enhancement mechanism and their distance dependencies are critical for achieving large SERS signals [49]. For this reason, SERS is used to improve detection; however, molecules must diffuse

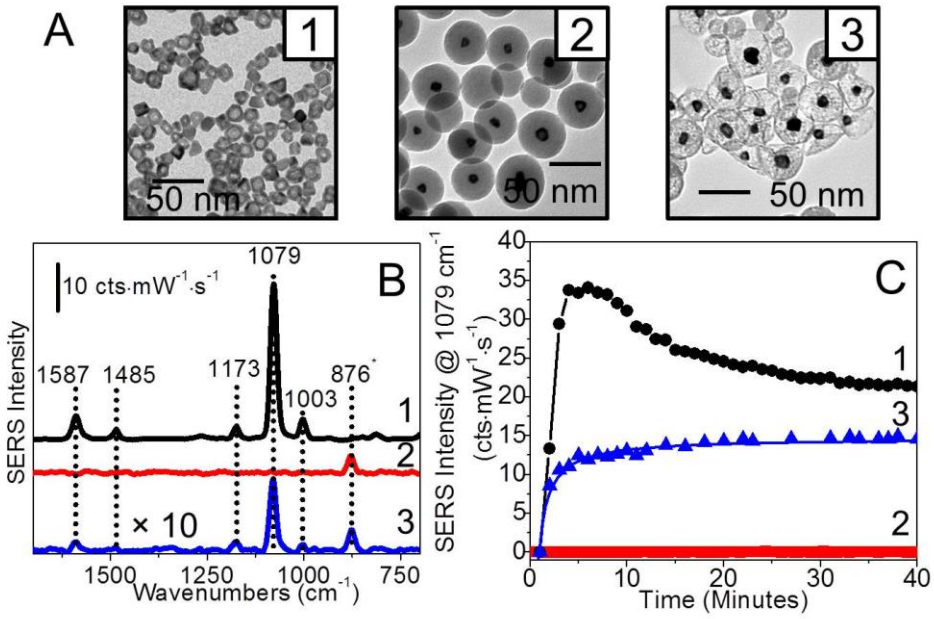

Figure 4.1. Ag@Au nanoparticles stabilized by (1) citrate, (2) silica shells, and (3) silica membranes. (A) Representative TEM images, (B) SERS spectra with the largest signal for 30 μM 2-aminothiophenol incubated with 6 nM nanoparticles, and (C) time-dependent SERS intensities. SERS parameters: λ_{ex} = 785 nm, t_{int} = 30 s, and P = 64 mW. Vibrational assignments: CC and CS stretch: 1587 cm^{-1}, CC stretch and CH bend: 1485 cm^{-1}, CC stretch and CH bend: 1173 cm^{-1}, CC and CS stretch: 1079 cm^{-1}, ring deformation: 1003 cm^{-1}, and ethanol: 876 cm^{-1}.

toward the plasmonic nanostructured surface and interact at short separation distances. Surface functionalization can be used to promote selective interactions between molecules and the nanostructured surface. For instance, molecular adsorption can be promoted using specific surface chemistry, which facilitates binding and detection [23]. Silica, for instance, is a structurally versatile, biocompatible, and optically transparent

protective material which can be subsequently modified with a variety of different chemical functionalities. If these layers are porous, target molecules can interact with the metal through the porous regions of this layer and be detected using SERS [2].

An example of SERS detection of 4-aminothiophenol on Ag@Au nanoparticles stabilized by (1) ions, (2) microporous silica shells, and (3) internally etched silica membranes is shown in Figures 5.1B and 5.1C. Ion stabilized nanoparticles reveal the largest SERS signals (Figure 4.1B-1); however, these signals vary rapidly with time. This occurs as molecules bind to the metal surface and destabilizes the materials and impacts the LSPR and SERS spectral properties (Figure 4.1C-1). In contrast, silica shell-stabilized Ag@Au nanoparticles (Figure 4.1A/B/C-2) are stable yet exhibit no SERS activity because the analytes do not interact with the large electric fields near the metal surface [2, 49]. Finally, silica membrane stabilized Ag@Au nanoparticles (Figure 4.1A/B/C-3) exhibit time dependent SERS signals, which are smaller than those observed with ion stabilized nanoparticles because the silica membranes prevent the formation of hot-spots between nanostructures, but the signals stabilize with time once the nanoparticle surfaces are saturated by molecules [1].

While membrane-stabilized nanoparticles result in predictable SERS signals as a function of time once surface saturation occurs, silica membrane formation depends on silica cross-linking and density [4]. Conditions such as pH, temperature, storage conditions, and storage time impact the formation of the silica membranes, which are important requirements for SERS [1, 4]. As previously reported for silica membrane stabilized Au nanoparticles, considerations of synthesis and storage parameters are important to achieve silica coated nanoparticles with similar silica cross-linking. Although attempts

are made to achieve consistent silica with uniform refractive indices, some variations in silica cross-linking can still exist because of the amorphous nature of the silica shell.

As a result, the optical properties of the Ag@Au nanoparticle cores can be used to characterize the dielectric properties of the silica shells and membranes. To do this, well-established dielectric models can be utilized [4, 50-51] using the LSPR properties of these materials. First, LSPR spectra are collected for Ag@Au and Ag@Au@SiO_2 nanoparticle samples are collected in water and varying bulk refractive index. Example LSPR spectra for these two samples are shown in Figure 4.2A. As expected, the presence of the silica shell induces a 14 nm red shift in the extinction maximum wavelength (λ_{max}) upon shell formation.

These samples can be rinsed and redispersed in solvents with known bulk refractive indices. This is shown in Figure 4.2B. To achieve varying bulk refractive indices, sucrose solutions varying from 0-85% (w/v) and 2 nM nanoparticle solutions are used. After a 30 minute incubation period, an increase in bulk refractive index causes the extinction maximum wavelengths for both samples to red shift. Equation 1, which describes the LSPR wavelength shift response ($\Delta\lambda_{max}$), can be used to describe these data as follows:

$$\Delta\lambda_{max} = m_1(n_{eff} - n_{water}) - m_2(n_{eff} - n_{water})^2 \quad (4.1)$$

where m_1 and m_2 are the linear and non-linear refractive index sensitivity terms that account for linear and non-linear changes in the local electric fields near the Ag@Au nanoparticle surfaces, n_{eff} is the effective local refractive index, and n_{water} is the refractive index of the water 1.33_3.

Both qualitative and quantitative differences are observed between LSPR spectra collected at various sucrose concentrations. For instance, Figure 4.2B shows that increasing bulk refractive index from 1.33 to 1.47_5 of ion stabilized Ag@Au and Ag@Au@SiO_2 nanoparticles

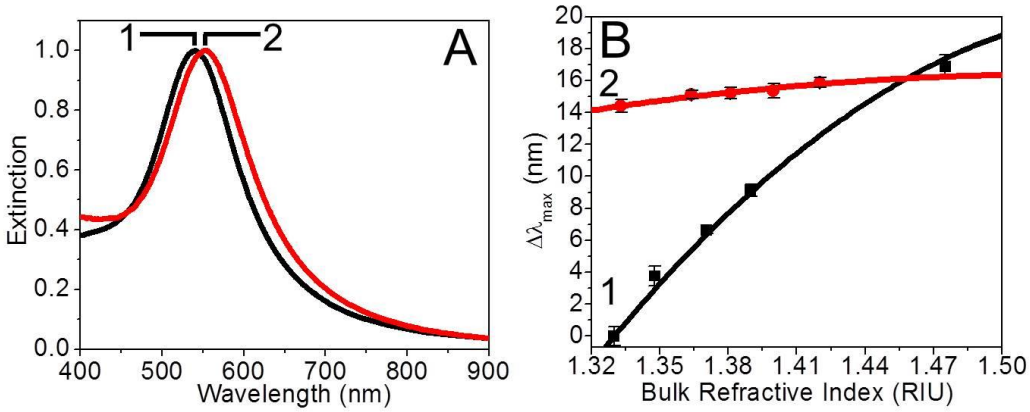

Figure 4.2. Evaluation of the dielectric properties of silica shells on Ag@Au nanoparticles. (A) LSPR spectra of (1) Ag@Au (λ_{max} = 539 nm) and (2) Ag@Au@SiO_2 (λ_{max} = 553 nm, silica shell thickness = 15.1 ± 6.8 nm) nanoparticles in water. (B) Shifts in the maximum LSPR wavelength as a function of bulk refractive index. Bulk refractive index was varied using 0-80% (w/v) sucrose solutions. Linear and non-linear refractive index sensitivities are 170 and 360 nm/RIU for the Ag@Au nanoparticles. The intersection point of the two curves represents the effective refractive–index on Ag@Au@SiO_2 nanoparticles. Furthermore, the LSPR decay length (l_d) is calculated to be ~11 nm according to the model. Error bars represent standard deviations from a minimum of three measurements.

(silica shell thickness = 15.1 ± 6.8 nm) red-shifts the maximum LSPR wavelengths non-linearly relative to initial λ_{max} of Ag@Au nanoparticles in water. From these data, the refractive index sensitivity is easily estimated using Equation 1. Second, the linear and non-linear refractive index sensitivities for Ag@Au nanoparticles are estimated as 170 and 360 nm/RIU, respectively. Third, the effective refractive index of the local condensed silica (including voids) around Ag@Au nanoparticles can be estimated using the intersection of the refractive index sensitivity responses as shown in Figure 4.2B. As such, the silica refractive index is found to be 1.45_8, a value that is

consistent with silica condensed on Au nanoparticles synthesized using a similar synthetic protocol [4]. Finally, the characteristic LSPR decay length (l_d) [51] for Ag@Au nanoparticles can be estimated as follows [4, 50]:

$$\Delta\lambda_{max} = m_1\left[(n_{silica} - n_{water})\left(1\text{-}e^{-\frac{2a}{l_d}}\right)\right] - m_2\left[(n_{silica} - n_{water})\left(1\text{-}e^{-\frac{2a}{l_d}}\right)\right]^2 \qquad (4.2)$$

where a is the silica shell thickness, n_{silica} is the refractive index of silica, and n_{water} is the refractive index of water. As such, the LSPR decay length is estimated at ~11 nm and can be subsequently used to quantify the dielectric characteristics of the silica membrane on Ag@Au@SiO_2 nanoparticles.

In addition, the effective refractive index (n_{eff}) of the silica-containing layer surrounding Ag@Au@SiO_2 nanoparticles can be estimated so that the LSPR properties of the metal cores can be correlated to effective silica density. First, 3 nM silica shell stabilized Ag@Au nanoparticles are immersed in 1.5 M NH_4OH for varying periods of time to induce membrane formation. The reaction is quenched by the addition of acid, and the samples are rinsed and redispersed in water. Example TEM images and LSPR spectra for three internally etched Ag@Au@SiO_2 nanoparticle samples are shown in Figures 5.3A and 5.3B, respectively. As expected, membrane formation is visible from varying silica contrast near the metal surfaces in the TEM images and results in systematic blue-shifts in the LSPR spectra.

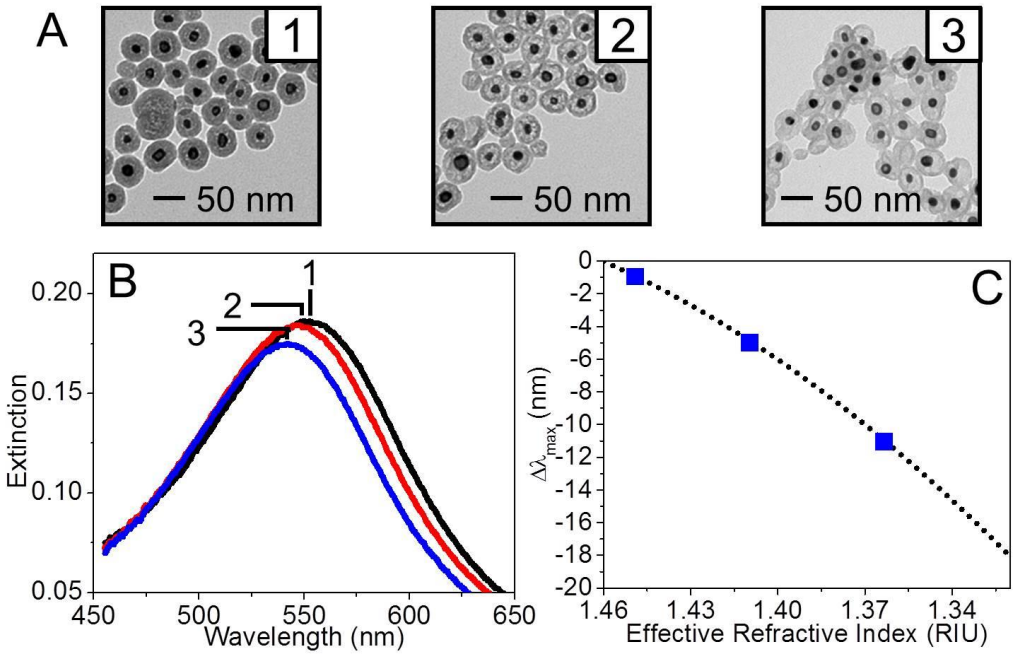

Figure 4.3. Determination of local effective refractive index for membrane stabilized Ag@Au@SiO_2 nanoparticles. (A) TEM images and (B) LSPR spectra of Ag@Au@SiO_2 nanoparticles after (1) 10 (λ_{max} = 551.9 nm, $\Delta\lambda_{max}$ = -1.1 nm), (2) 30 (λ_{max} = 547.9 nm, $\Delta\lambda_{max}$ = -5.1 nm), and (3) 40 (λ_{max} = 541.9 nm, $\Delta\lambda_{max}$ = -11.1 nm) minutes. (C) LSPR wavelength maximum shifts as a function of effective refractive index of silica membrane stabilized nanoparticles. The effective refractive index is estimated using the previously determined dielectric properties of the materials.

Next, equation 3 can be used to relate nanoparticle morphology to the optical properties of the internally etched Ag@Au@SiO_2 nanoparticles. The relationship between n_{eff} and the void near the surface of the metal nanoparticles is related as follows:

$$n_{eff} = n_{void}\left(1-e^{-\frac{2V}{l_d}}\right) + n_{silica}\left(e^{-\frac{2V}{l_d}}-e^{-\frac{2S}{l_d}}\right) + n_{water}\left(e^{-\frac{2S}{l_d}}\right) \quad (4.3)$$

where n_{void} is the refractive index of the void areas in the silica shell, V is the void

thickness, and S is the silica membrane thickness (*i.e.*, total silica shell thickness – void thickness). The observed LSPR wavelength shift data in Figure 4.3B are then related to effective refractive index around the Ag@Au cores. This result is shown in Figure 4.3C. As expected, shifts in the λ_{max} increase in magnitude as etching progresses and voids around the nanoparticle cores form. As the effective refractive index decreases from 1.45_8 (silica) to 1.33_3 (water), an 18 nm blue-shift is clearly observed for internally etched Ag@Au@SiO_2 nanoparticles. By combining these straight-forward LSPR measurements, TEM images, and dielectric model, the effective refractive index for the porous silica in Figures 5.3A-1, 5.3A-2, and 5.3A-3 are estimated at 1.44_8, 1.40_8, and 1.36_2, respectively. The impact of the effective refractive index and as a result, effective silica density are expected to impact the diffusion of molecules near the metal nanoparticle core [1], which should influence the size of the SERS-active volume near the metal surface and as a consequence, the magnitude of the SERS signal of small molecules (*vide infra*).

4.3.2 SERS Signals as a Function of Effective Refractive Index

SERS signals arise from molecules occupying the volume nearest to the metal substrate [25] and is often approximated in terms of distance dependence [3]. For internally etched Ag@Au@SiO_2 nanoparticles, the silica membrane and interior void is the matter that occupies the SERS-active volume and facilitates molecular diffusion through the silica shells for SERS detection. As such, SERS intensities are expected to increase as the effective refractive index decreases. To evaluate this hypothesis, nine internally etched Ag@Au@SiO_2 nanoparticle samples are prepared so that the effective refractive index varies from 1.36 to 1.46. The nanoparticle samples are diluted to final concentrations of 6

nM and incubated with 30 μM 4-aminothiophenol for at least 1 hour. SERS signals were

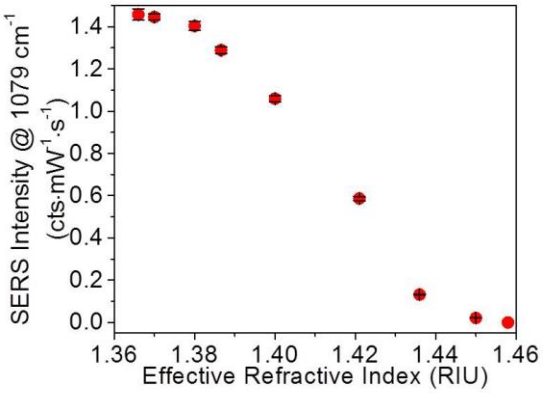

Figure 4.4. SERS signals for 6 nM silica membrane stabilized Ag@Au nanoparticles incubated with 30 μM 4-aminothiophenol for at least 1 hour. Effective refractive index was varied from 1.36_6 to 1.45_8 and SERS intensity was plotted using the 1079 cm^{-1} CS/CC stretching frequency. At lower effective refractive indices, SERS intensities are limited by saturation of the metal surface area and volume near the metal surface whereas at high effective refractive indices, the volume near the metal surface is blocked by silica thereby reducing the overall SERS intensity. Averages and standard deviations are reported using at least 3 measurements. Same SERS parameters as in Figure 4.1.

collected, and the CS/CC stretching frequency centered at 1079 cm^{-1} is plotted as a function of effective refractive index. These data are summarized in Figure 4.4 and reveal that SERS intensity increases with decreasing effective refractive index (*i.e.*, increasing void volume). As the effective refractive index decreases from 1.45_8 to 1.33_3 nm, Si-O-Si bonds in the polymer matrix are broken thereby generating silica voids near the metal surface, which can then be occupied by molecules or solvent. Of note, decreasing the effective refractive index from 1.44 to 1.38 shows significant changes in SERS intensities. As more molecules occupy the internal silica volume, SERS signals increase.

Above an effective refractive index of 1.48, insufficient internal volume is available thereby hindering molecular diffusion and as a result, reduces SERS intensities. When the effective local refractive index is less than 1.38, SERS intensities saturate and are limited by monolayer formation of 4-aminothiophenol on the Ag@Au nanoparticle surfaces. Because small changes in effective refractive index near the metal core impact SERS intensities, these data suggest that SERS signals are reproducible if effective refractive index of the local environment of the local SERS-active volume surrounding the SERS substrate is considered.

4.3.3 SERS Signal Dependencies on Molecular Concentrations

SERS signals from analytes depend on the silica-free surface area and volume near the Ag@Au nanoparticles, SERS signals should vary as a function of analyte to molecule concentration. To understand how molecular concentration impacts SERS signals, 6 nM internally etched Ag@Au@SiO_2 nanoparticles were incubated with 4-aminothiophenol concentrations ranging from 1 - 30 μM for at least 1 hour in 10 mM phosphate buffer (pH 7.4). The effective refractive index is maintained at 1.38 to ensure consistent internal void volumes. Representative SERS spectra are shown in Figure 4.5A and reveal that the unique molecular vibrational modes for 4-aminothiophenol centered at 1173 cm^{-1} (CH bend, CC stretch), 1079 cm^{-1} (CC and CS stretches), and 393 cm^{-1} (CS bend) [52-55] are consistent with the a_1 vibrational modes for 4-aminothiophenol and the formation of a monolayer of 4-aminothiophenol on the metal surface.

The largest SERS intensity in each spectrum is observed for the CC/CS stretching transitions, which is consistent with molecules attached to the metal surface through

sulfur atom and enhanced by the strong electromagnetic fields near the metal surface [52-54].Of note, only a_1 symmetric vibrational modes are observed for 4-aminothiophenol, which suggests that the molecules are oriented on the metal surface as a loosely packed monolayer with an average tilt angle of ~30° [56-57].

Previously, silica membranes were shown to prevent plasmon coupling between gold nanoparticle cores [1-2, 4], and similar observations are observed here for internally etched Ag@Au@SiO_2 nanoparticles. Thus, SERS signal changes are a consequence of local 4-aminothiophenol concentration inside the silica membrane and are expected to provide quantitative molecular detection. Because SERS signals are directly proportional to the number of molecules within the localized SERS-active volume near the metal surface, saturated SERS signals should be limited by 4-aminothiophenol monolayer

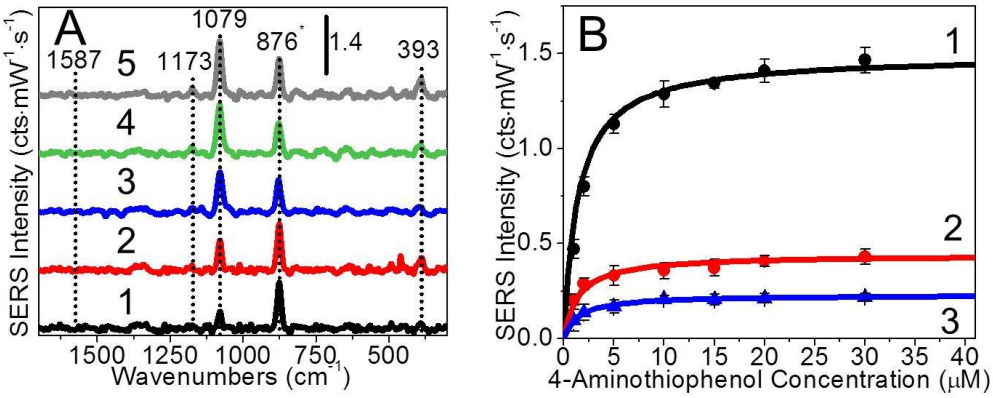

Figure 4.5. SERS data for 6 nM IE Ag@Au@SiO_2 nanoparticles with effective silica refractive index of 1.38 as a function of molecular concentration. (A) Maximum SERS spectra for (1) 1, (2) 2, (3) 5, (4) 20, and (5) 30 μM 4-aminothiophenol and (B) SERS intensity for the vibrational modes centered at (1) 1079 cm^{-1} (CC and CS stretches), (2) 393 cm^{-1} (CS bend), and (3) 1173 cm^{-1} (CC stretch and CH bend) as a function of 4-aminothiophenol concentration. Averages and standard deviations are reported using at least 3 measurements. Same SERS parameters as in Figure 4.1.

formation. To evaluate these trends, SERS intensities for CC stretch/CH bend, CS/CC stretch, and CS bend modes are plotted as a function of 4-aminothiophenol concentration and 6 nM internally etched Ag@Au@SiO_2 nanoparticles with an effective refractive index of 1.38 (1+ hour incubation).

As shown in Figure 4.5B, the SERS intensities for each vibrational frequency systematically increase then saturate after the addition of ~20 μM 4-aminothiophenol. First, the CC/CS stretching and CC stretching/CH bending modes, which are orientation independent, represent SERS signals from all molecules that occupy SERS-active volume inside each silica membrane. Second, the CS bending mode centered at 393 cm^{-1} is consistent with molecules bound to the metal surface [58-60]. Finally, because of the absence of b_2 vibrational modes, 4-aminothiophenol signals are limited to molecules inside the silica shells in the absence of strong electric fields induced by hot-spots [55, 61], and the effective molecular footprint of molecules are estimated at 0.535 nm^2/molecule [57]. As such, a monolayer of 4-aminothiophenol would be achieved if ~2000 molecules/nanoparticle were added to solution (assuming an average Ag@Au nanoparticle diameter = 18.5 nm). For a 6 nM nanoparticle solution, this equates to a 12 μM 4-aminothiophenol concentration. As a result, any molecular concentration below 12 μM should provide a concentration dependent response while concentrations above this value should be concentration independent. This is observed in Figure 4.5B. These results demonstrate that quantitative and reproducible SERS detection is possible once the effective refractive index surrounding internally etched Ag@Au@SiO_2 nanoparticles as well as metal surface area are considered.

4.3.4 SERS Signal Dependencies on Nanoparticle Concentrations

Finally, SERS signals are evaluated as a function of internally etched Ag@Au nanoparticle concentration. The concentration of internally etched silica coated Ag@Au

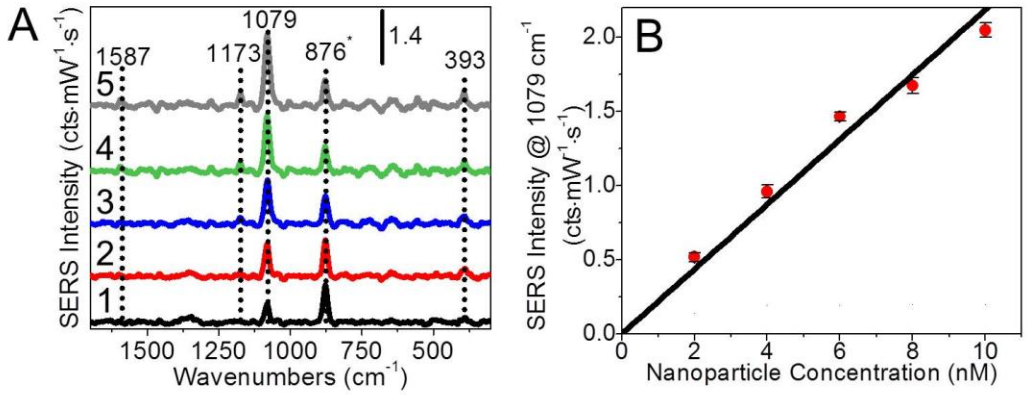

Figure 4.6. Nanoparticle concentration dependent (A) SERS spectra and (B) intensities for 30 μM 4-aminothiophenol. Nanoparticle concentration was varied from (1) 2, (2) 4, (3) 6, (4) 8, and (5) 10 nM 4-aminothiophenol. The samples were spiked with 1% ethanol, and the ethanol signal at 876 cm^{-1} was used to account for sample to sample focus variations. Vibrational assignments: CC and CS stretch: 1587 cm^{-1}, CC stretch and CH bending: 1173 cm^{-1}, CC and CS stretches: 1079 cm^{-1}, ethanol: 876 cm^{-1}, and CS bending: 393 cm^{-1}. Averages and standard deviations are reported using at least 3 measurements. Same SERS parameters as in Figure 4.1.

nanoparticles with an effective refractive index of 1.38 were varied from 0-10 nM and incubated with 30 μM 4-aminothiophenol for at least 1 hour to ensure that a molecular excess was added to solution. Representative SERS spectra are shown in Figure 4.6A and show a systematic increase in SERS intensity with increasing nanoparticle concentration. The SERS intensity for the CS\CC stretch at 1079 cm^{-1} is plotted as a function of

internally etched Ag@Au@SiO_2 nanoparticle concentration and increases linearly over the concentration range studied (Figure 4.6B). Above this concentration, signals and background vary significantly from measurement to measurement and are attributed to detector limitations and/or light throughput. This suggests that nanoparticle concentration directly impacts SERS signals, and can be used to lower detection limits as well as to expand the dynamic range for quantitative SERS detection of small molecules.

4.3.5 Conclusion

In summary, the optical properties of Ag@Au nanoparticles were estimated using a semi-empirical approach to estimate the refractive index sensitivity and characteristic electromagnetic field decay length of Ag@Au nanoparticles as well as the dielectric properties of the silica membrane. Using the local effective refractive index surrounding the Ag@Au nanoparticles, internally etched Ag@Au@SiO_2 nanoparticles were synthesized and used as SERS substrates. Several trends were observed. First, by maintaining nanoparticle morphology (including silica thickness and effective refractive index), systematic changes in SERS signals were observed and attributed to silica-limited SERS-active volumes near the metal core. Second, when low molecule concentrations were added to internally etched Ag@Au@SiO_2 nanoparticles, SERS signals were limited by the number of molecules on the metal surface, and SERS signals saturated when a monolayer of 4-aminothiophenol formed. Finally, when an excess of 4-aminothiophenol was added relative to the SERS-active volume/surface area, SERS signals depended on the nanoparticle concentration. All in all, these findings show that using dielectric modeling to gain insight into effective refractive index around internally etched Ag@Au@SiO_2 nanoparticles is important for quantitative and reproducible SERS.

Future studies could be carried out to use these materials for quantitative SERS detection with tunable linear dynamic ranges and detection limits.

1. Roca, M.; Haes, A. J., Silica-Void-Gold Nanoparticles: Temporally Stable Surface-Enhanced Raman Scattering Substrates. *J. Am. Chem. Soc.* **2008**, *130*, 14273-14279.
2. Pierre, M. C. S.; Haes, A. J., Purification Implications on Sers Activity of Silica Coated Gold Nanospheres. *Analytical Chemistry* **2012**, *84*, 7906-7911.
3. Pierre, M. C. S.; Mackie, P. M.; Roca, M.; Haes, A. J., Correlating Molecular Surface Coverage and Solution-Phase Nanoparticle Concentration to Surface-Enhanced Raman Scattering Intensities. *The Journal of Physical Chemistry C* **2011**, *115*, 18511–18517.
4. Volkert, A. A.; Pierre, M. C. S.; Shrestha, B.; Haes, A. J., Implications of Sample Aging on the Formation of Internally Etched Silica Coated Gold Nanoparticles. *RSC Advances* **2015**, *5*, 3774-3780.
5. Zhao, J.; Pinchuk, A. O.; McMahon, J. M.; Li, S. Z.; Ausman, L. K.; Atkinson, A. L.; Schatz, G. C., Methods for Describing the Electromagnetic Properties of Silver and Gold Nanoparticles. *Accounts of Chemical Research* **2008**, *41*, 1710-1720.
6. Xu, H.; Aizpurua, J.; Kall, M.; Apell, P., Electromagnetic Contributions to Single-Molecule Sensitivity in Surface-Enhanced Raman Scattering. *Physical Review E* **2000**, *62*, 4318-24.
7. Doering, W. E.; Nie, S., Single-Molecule and Single-Nanoparticle Sers: Examining the Roles of Surface Active Sites and Chemical Enhancement. *J. Phys. Chem. B* **2002**, *106*, 311-317.
8. Haynes, C. L.; Van Duyne, R. P., Nanosphere Lithography: A Versatile Nanofabrication Tool for Studies of Size-Dependent Nanoparticle Optics. *J. Phys. Chem. B* **2001**, *105*, 5599-5611.
9. Mulvaney, P., Not All That's Gold Does Glitter. *MRS Bulletin* **2001**, *26*, 1009-1014.
10. El-Sayed, M. A., Some Interesting Properties of Metals Confined in Time and Nanometer Space of Different Shapes. *Acc. Chem. Res.* **2001**, *34*, 257-264.
11. Link, S.; El-Sayed, M. A., Spectral Properties and Relaxation Dynamics of Surface Plasmon Electronic Oscillations in Gold and Silver Nano-Dots and Nano-Rods. *J. Phys. Chem. B* **1999**, *103*, 8410-8426.
12. Kreibig, U.; Gartz, M.; Hilger, A.; Hovel, H., Optical Investigations of Surfaces and Interfaces of Metal Clusters. In *Advances in Metal and Semiconductor Clusters*, Duncan, M. A., Ed. JAI Press Inc.: Stamford, 1998; Vol. 4, pp 345-393.
13. Mulvaney, P., Surface Plasmon Spectroscopy of Nanosized Metal Particles. *Langmuir* **1996**, *12*, 788-800.
14. Kreibig, U., Optics of Nanosized Metals. In *Handbook of Optical Properties*, Hummel, R. E.; Wissmann, P., Eds. CRC Press: Boca Raton, 1997; Vol. II, pp 145-190.
15. Hulteen, J. C.; Treichel, D. A.; Smith, M. T.; Duval, M. L.; Jensen, T. R.; Van Duyne, R. P., Nanosphere Lithography: Size-Tunable Silver Nanoparticle and Surface Cluster Arrays. *J. Phys. Chem. B* **1999**, *103*, 3854-3863.
16. Fang, J. X.; Yi, Y.; Ding, B. J.; Song, X. P., A Route to Increase the Enhancement Factor of Surface Enhanced Raman Scattering (Sers) Via a High Density Ag Flower-Like Pattern. *Appl Phys Lett* **2008**, *92*, 131113.
17. Kneipp, K.; Kneipp, H.; Itzkan, I.; Dasari, R. R.; Feld, M. S., Ultrasensitive Chemical Analysis by Raman Spectroscopy. *Chemical Reviews* **1999**, *99*, 2957-76.
18. Liu, Y. C., Evidence of Chemical Effect on Surface-Enhanced Raman Scattering

of Polypyrrole Films Electrodeposited on Roughened Gold Substrates. *Langmuir* **2002**, *18*, 174-181.
19. Fromm, D. P.; Sundaramurthy, A.; Kinkhabwala, A.; Schuck, P. J.; Kino, G. S.; Moerner, W. E., Exploring the Chemical Enhancement for Surface-Enhanced Raman Scattering with Au Bowtie Nanoantennas. *J Chem Phys* **2006**, *124*, 061101.
20. Campion, A.; Kambhampati, P., Surface-Enhanced Raman Scattering. *Chem. Soc. Rev.* **1998**, *27*, 241-250.
21. Kinnan, M. K.; Chumanov, G., Surface Enhanced Raman Scattering from Silver Nanoparticle Arrays on Silver Mirror Films: Plasmon-Induced Electronic Coupling as the Enhancement Mechanism. *Journal of Physical Chemistry C* **2007**, *111*, 18010-18017.
22. Daniels, J. K.; Chumanov, G., Nanoparticle-Mirror Sandwich Substrates for Surface-Enhanced Raman Scattering. *Journal of Physical Chemistry B* **2005**, *109*, 17936-17942.
23. Berrade, L.; Garcia, A. E.; Camarero, J. A., Protein Microarrays: Novel Developments and Applications. *Pharmaceutical Research* **2011**, *28*, 1480-1499.
24. Roca, M.; Mackie, P. M.; Haes, A. J., Design of a Biocompatible and Optically-Stable Solution-Phase Substrate for Sers Detection. *Mater. Res. Soc. Symp. Proc.* **2008**, *1133E*, No pp given.
25. Stoerzinger, K. A.; Lin, J. Y.; Odom, T. W., Nanoparticle Sers Substrates with 3d Raman-Active Volumes. *Chemical Science* **2011**, *2*, 1435-1439.
26. Lee, S.; Hahm, M. G.; Vajtai, R.; Hashim, D. P.; Thurakitseree, T.; Chipara, A. C.; Ajayan, P. M.; Hafner, J. H., Utilizing 3d Sers Active Volumes in Aligned Carbon Nanotube Scaffold Substrates. *Adv. Mat.* **2012**, *24*, 5261-5266.
27. Zhang, L.; Lang, X.; Hirata, A.; Chen, M., Wrinkled Nanoporous Gold Films with Ultrahigh Surface-Enhanced Raman Scattering Enhancement. *ACS Nano* **2011**, *5*, 4407-4413.
28. Ko, H.; Chang, S.; Tsukruk, V. V., Porous Substrates for Label-Free Molecular Level Detection of Nonresonant Organic Molecules. *ACS Nano* **2009**, *3*, 181-188.
29. Chan, S.; Kwon, S.; Koo, T. W.; Lee, L. P.; Berlin, A. A., Surface-Enhanced Raman Scattering of Small Molecules from Silver-Coated Silicon Nanopores. *Advanced Materials* **2003**, *15*, 1595-1598.
30. Srnova-Sloufova, I.; Vlckova, B.; Bastl, Z.; Hasslett, T. L., Bimetallic (Ag)Au Nanoparticles Prepared by the Seed Growth Method: Two-Dimensional Assembling, Characterization by Energy Dispersive X-Ray Analysis, X-Ray Photoelectron Spectroscopy, and Surface Enhanced Raman Spectroscopy, and Proposed Mechanism of Growth. *Langmuir* **2004**, *20*, 3407-3415.
31. Cui, Y.; Ren, B.; Yao, J.-L.; Gu, R.-A.; Tian, Z.-Q., Synthesis of Agcoreaushell Bimetallic Nanoparticles for Immunoassay Based on Surface-Enhanced Raman Spectroscopy. *The Journal of Physical Chemistry B* **2006**, *110*, 4002-4006.
32. Paramelle, D.; Sadovoy, A.; Gorelik, S.; Free, P.; Hobley, J.; Fernig, D. G., A Rapid Method to Estimate the Concentration of Citrate Capped Silver Nanoparticles from Uv-Visible Light Spectra. *Analyst* **2014**, *139*, 4855-4861.
33. Stober, W.; Finx, A.; Bohn, E., Controlled Growth of Monodisperse Silica Spheres
in the Micron Size Range. *J. Coll. Interface Sci.* **1968**, *26*, 62.
34. Liz-Marzan, L. M.; Giersig, M.; Mulvaney, P., Synthesis of Nanosized Gold-Silica Core-Shell Particles. *Langmuir* **1996**, *12*, 4329-4335.
35. Grzelczak, M.; Correa-Duarte, M. A.; Liz-Marzan, L. M., Carbon Nanotubes Encapsulated in Wormlike Hollow Silica Shells. *Small* **2006**, *2*, 1174-1177.
36. Suzuki, M.; Maekita, W.; Wada, Y.; Nagai, K.; Nakajima, K.; Kimura, K.; Fukuoka, T.; Mori, Y., Ag Nanorod Arrays Tailored for Surface-Enhanced Raman Imaging in the near-Infrared Region. *Nanotechnology* **2008**, *19*, 265304/1-265304/7.
37. Giallongo, G.; Pilot, R.; Durante, C.; Rizzi, G. A.; Signorini, R.; Bozio, R.; Gennaro, A.; Granozzi, G., Silver Nanoparticle Arrays on a Dvd-Derived Template: An

Easy & Cheap Sers Substrate. *Plasmonics* **2011**, *6*, 725-733.
38. Guieu, V.; Garrigue, P.; Lagugne-Labarthet, F.; Servant, L.; Sojic, N.; Talaga, D., Remote Surface Enhanced Raman Spectroscopy Imaging Via a Nanostructured Optical Fiber Bundle. *Optics Express* **2009**, *17*, 24030-24035.
39. Liu, G. L.; Lee, L. P., Nanowell Surface Enhanced Raman Scattering Arrays Fabricated by Soft-Lithography for Label-Free Biomolecular Detections in Integrated Microfluidics. *Appl Phys Lett* **2005**, *87*, 074101/1-074101/3.
40. Kantarovich, K.; Tsarfati, I.; Gheber, L. A.; Haupt, K.; Bar, I., Writing Droplets of Molecular Imprinted Polymers by Nano Fountain Pen and Detecting Their Molecular Interactions by Surface-Enhanced Raman Scattering. *Analytical Chemistry* **2009**, *81*, 5686-5690.
41. Kantarovich, K.; Tsarfati, I.; Gheber, L. A.; Haupt, K.; Bar, I., Reading Microdots of a Molecularly Imprinted Polymer by Surface-Enhanced Raman Spectroscopy. *Biosensors and Bioelectronics* **2010**, *26*, 809-814.
42. Theiss, J.; Pavaskar, P.; Echternach, P. M.; Muller, R. E.; Cronin, S. B., Plasmonic Nanoparticle Arrays with Nanometer Separation for High-Performance Sers Substrates. *Nano Letters* **2010**, *10*, 2749-2754.
43. Qin, L.; Zou, S.; Xue, C.; Atkinson, A.; Schatz, G. C.; Mirkin, C. A., Designing, Fabricating, and Imaging Raman Hot Spots. *Proceedings of the National Academy of Sciences of the United States of America* **2006**, *103*, 13300-13303.
44. Zamuner, M.; Talaga, D.; Deiss, F.; Guieu, V.; Kuhn, A.; Ugo, P.; Sojic, N., Fabrication of a Macroporous Microwell Array for Surface-Enhanced Raman Scattering. *Advanced Functional Materials* **2009**, *19*, 3129-3135.
45. Qian, L.; Mookherjee, R., Convective Assembly of Linear Gold Nanoparticle Arrays at the Micron Scale for Surface-Enhanced Raman Scattering. *Nanoparticle Research* **2011**, *4*, 1117-1128.
46. Henry, A.-I.; Bingham, J. M.; Ringe, E.; Marks, L. D.; Schatz, G. C.; Van Duyne, R. P., Correlated Structure and Optical Property Studies of Plasmonic Nanoparticles. *Journal of Physical Chemistry C* **2011**, *115*, 9291-9305.
47. Giannini, V.; Fernandez-Dominguez, A. I.; Heck, S. C.; Maier, S. A., Plasmonic Nanoantennas: Fundamentals and Their Use in Controlling the Radiative Properties of Nanoemitters. *Chemical Reviews* **2011**, *111*, 3888-3912.
48. Rivas, L.; Sanchez-Cortes, S.; García-Ramos, J. V.; Morcillo, G., Mixed Silver/Gold Colloids: A Study of Their Formation, Morphology, and Surface-Enhanced Raman Activity. *Langmuir* **2000**, *16*, 9722-9728.
49. Jensen, L.; Aikens, C. M.; Schatz, G. C., Electronic Structure Methods for Studying Surface-Enhanced Raman Scattering. *Chem. Soc. Rev.* **2008**, *37*, 1061-1073.
50. Jung, L. S.; Campbell, C. T.; Chinowsky, T. M.; Mar, M. N.; Yee, S. S., Quantitative Interpretation of the Response of Surface Plasmon Resonance Sensors to Adsorbed Films. *Langmuir* **1998**, *14*, 5636-5648.
51. Haes, A. J.; Zou, S.; Schatz, G. C.; Van Duyne, R. P., A Nanoscale Optical Biosensor: The Long Range Distance Dependence of the Localized Surface Plasmon Resonance of Noble Metal Nanoparticles. *J. Phys. Chem. B* **2004**, *108*, 109-116.
52. Zhu, Z.; Zhu, T.; Liu, Z., Raman Scattering Enhancement Contributed from Individual Gold Nanoparticles and Interparticle Coupling. *Nanotech.* **2004**, *15*, 357-364.
53. Kim, K.; Lee, H. S., Effect of Ag and Au Nanoparticles on the Sers of 4-Aminobenzenethiol Assembled on Powdered Copper. *The Journal of Physical Chemistry B* **2005**, *109*, 18929-18934.
54. Hu, X.; Wang, T.; Wang, L.; Dong, S., Surface-Enhanced Raman Scattering of 4-Aminothiophenol Self-Assembled Monolayers in Sandwich Structure with Nanoparticle Shape Dependence: Off-Surface Plasmon Resonance Condition. *The Journal of Physical Chemistry C* **2007**, *111*, 6962-6969.
55. Huang, Y.-F.; Wu, D.-Y.; Zhu, H.-P.; Zhao, L.-B.; Liu, G.-K.; Ren, B.; Tian, Z.-Q., Surface-Enhanced Raman Spectroscopic Study of P-Aminothiophenol. *Phys. Chem.*

Chem. Phys. **2012**, *14*, 8485-8497.
56. Janesko, B. G.; Scuseria, G. E., Surface Enhanced Raman Optical Activity of Molecules on Orientationally Averaged Substrates: Theory of Electromagnetic Effects. *The Journal of Chemical Physics* **2006**, *125*, 124704.
57. Wan, L.-J.; Terashima, M.; Noda, H.; Osawa, M., Molecular Orientation and Ordered Structure of Benzenethiol Adsorbed on Gold(111). *The Journal of Physical Chemistry B* **2000**, *104*, 3563-3569.
58. Olson, L. G.; Harris, J. M., Surface-Enhanced Raman Spectroscopy Studies of Surfactant Adsorption to a Hydrophobic Interface. *Applied Spect.* **2008**, *62*, 149-156.
59. Izquierdo-Lorenzo, I.; García-Ramos, J. V.; Sanchez-Cortes, S., Vibrational Characterization and Surface-Enhanced Raman Scattering Detection of Probenecid Doping Drug. *J. Raman Spect.* **2013**, *44*, 1422-1427.
60. Haynes, C. L.; Yonzon, C. R.; Zhang, X.; Van Duyne, R. P., Surface-Enhanced Raman Sensors: Early History and the Development of Sensors for Quantitative Biowarfare Agent and Glucose Detection. *Journal of Raman Spectroscopy* **2005**, *36*, 471-484.
61. Choi, H.-K.; Shon, H. K.; Yu, H.; Lee, T. G.; Kim, Z. H., B2 Peaks in Sers Spectra of 4-Aminobenzenethiol: A Photochemical Artifact or a Real Chemical Enhancement? *The Journal of Physical Chemistry Letters* **2013**, *4*, 1079-1086.

CHAPTER 5 ADSORPTION OF THIOLATED MOLECULES ON INTERNALLY ETCHED AG@AU NANOPARTICLES USING LSPR AND SERS

5.1 Introduction

Solution-phase nanoparticles are extensively used as surface enhanced Raman scattering (SERS) substrates[1-4] but often fail at providing reproducible signals for a given molecular concentration because of their dynamic optical properties[3, 5] and sometimes poor solution-phase stabilities.[9] Furthermore, molecule orientation and surface selection rules[5, 10-11] can lead to often unexpected SERS intensities. For instance, molecules exhibit different SERS enhancements based on the polarizability and symmetry of vibrational mode. Vibrational modes oriented perpendicular with respect to the surface exhibit the largest enhancements while those parallel to the surface can be absent. Various studies utilized inherent sensitivity of SERS to explain molecular orientation of aromatic species in electrochemical and colloidal surfaces.[8, 11] These studies analyzed sensitivity of vibration modes such as CH, out of plane, and in plane ring modes to surface enhancements. Specifically, enhancement of in plane modes vs. out of plane modes (b_2 symmetry relative to a_2 symmetry in C_{2V} molecule can relate to molecular orientation[13-14] in solution phase nanoparticles. Because solution-phase nanoparticles exhibit inherently high surface energies, these trends are often difficult to assess because of nanoparticle aggregation and fluctuating electromagnetic properties of the metal nanoparticles. As a result, quantitative detection is often limited using these SERS substrates.[16]

Understanding molecular orientation is important in the interactions between adsorbates and nanomaterial substrates such as those used in SERS, and the adsorption

process can influence the measurable signals. Molecular orientation, however, is influenced by adsorbate concentration and composition. For instance, the adsorption dynamics of DNA onto citrate stabilized Au nanoparticles,[17] Hg(II) adsorption on polyrhodanine-coated Fe_2O_3 nanoparticles,[18] and oxalic acid on TiO_2 nanoparticles[19] were previously reported. These studies successfully yielded information regarding surface chemistry and nanoparticle stability yet provided limited to no information regarding molecule orientation. In addition, contributing factors from nanoparticle aggregation kinetics and molecular adsorption dynamics are largely influenced by surface energy.[19] Thus, nanoparticle stability and adsorption dynamics must be considered if molecular orientation information or if quantitative detection using SERS is desired.

To promote nanoparticle stability, surface modification of SERS-active substrates can be achieved using silica and/or polymers.[1, 20-22] One substrate that provides both optical stability of the SERS-active metal surface and molecular accessibility to the metal is internally etched silica coated metal nanoparticles.[1, 4] Quantitative SERS detection is achieved with these materials by the formation of internal voids in the silica matrix near the metal nanoparticle core, which not only allowed molecular diffusion, but also maintained nanoparticle optical stability. Only molecules that diffused through the silica membrane were detected using SERS. Additionally, averaged molecular coverage on the entire metal surface[23] contributed to the overall SERS intensity. This is fortunate given that these SERS signals were modest at best because the silica shells prevented electromagnetic coupling between the metal cores.

Herein, IE Ag@Au@SiO_2 nanoparticles are synthesized for their use as SERS substrates to ensure electromagnetic stability of the metal cores and surface accessibility

for molecular adsorption for SERS detection. The implications of molecular identity and concentration on molecular adsorption and SERS intensity are evaluated using localized surface plasmon resonance (LSPR) spectroscopy, SERS, and Langmuir adsorption isotherm modeling. Four molecules, 2-naphthalenethiol, benzenethiol, p-aminothiophenol, and 4-mercaptobenzoic acid are selected because they contain different molecular footprints and functionalities. Synergistic results suggesting molecule-dependent tilt angles on the Ag@Au nanoparticle surface are estimated using LSPR spectroscopy and implications evaluated using SERS. While multiple vibrational modes are observed and exhibit similar adsorption behavior for each molecule, molecule to molecule SERS intensity differences are consistent with slight differences in molecular tilt angle relative to the metal surface. These findings are confirmed through Langmuir adsorption isotherm modeling where equilibrium constants and free energies of adsorption associated suggest favorable binding for 4-mercaptobenzoic acid and p-aminothiophenol vs. 2-naphthalenethiol and benzenethiol. These differences are attributed to London dispersion force stabilization between the ligands and the metal surface and are easily observed because of the optical stability and controlled adsorbate interactions with IE Ag@Au@SiO_2 nanoparticles. As such, this approach could be extended to other molecules in the future to better understand and evaluate the quantitative capabilities of SERS substrates.

5.2 Materials and Methods

5.2.1 Chemical Reagents.

Gold(III) chloride trihydrate, sodium citrate dihydrate, Amberlite MB-150 mixed bed exchange resin, (3-aminopropyl) trimethoxysilane (APTMS), sodium chloride

(NaCl), sodium trisilicate (27%), tetraethyl orthosilicate (TEOS), silver perchlorate, sodium borohydride, 2-naphthalenethiol, benzenthiol, 4-mercaptobenzoic acid, p-aminothiophenol, and hydroxylamine hydrochloride were purchased from Sigma. Ethanol, ammonium hydroxide (NH_4OH), hydrochloric acid (HCl), and nitric acid (HNO_3) were purchased from Fisher Scientific (Pittsburgh, PA). Ultrapure water (18.2 $M\Omega\ cm^{-1}$) was obtained from a Barnstead Nanopure System and used for all experiments. All glassware items were cleaned with aqua regia (3:1 HCl/ HNO_3) and rinsed thoroughly with water, and oven (glass) or air (plastic) dried overnight before use.

5.2.2 Nanoparticle Synthesis.

Ag@Au nanoparticles were synthesized using a seeded growth method previously described in the literature.[24-25] Briefly, 100 mL of a 0.3 mM sodium citrate solution prepared in nitrogen-purged water was stirred on an ice bath in the dark. Freshly prepared sodium borohydride (final concentration = 1 mM) was added to the citrate solution. Next, 1 mL of 10 mM silver perchlorate was added to the solution within 2 minutes, and the resulting silver nanoparticle solution was stirred for 3 minutes. Stirring was stopped, and silver nanoparticles with average diameters of 11.5 ± 3.2 nm formed within 3 hours. Next, 20 mL of water was added to 25 mL of as-synthesized Ag seeds and stirred for ~2 minutes (4 °C). Fifteen mL of both 6.25 mM hydroxylamine hydrochloride and 0.465 mM gold salt were added slowly (3 mL/min) using syringe pump. This Ag@Au nanoparticle solution was stirred for 1 hour to ensure nanoparticle formation and stored at 2 – 4 °C until use. The concentration of these materials was estimated using a standard estimation model for the silver seeds,[26] and an average diameter of 18.5 ± 2.3 nm was determined using TEM.

Silica shells on Ag@Au ($Ag@Au@SiO_2$) nanoparticles were synthesized via a modified Stöber method.[20, 27-29] Briefly, the pH and conductivity of 25 mL of the as synthesized Ag@Au nanoparticles were adjusted to 5 and ~110 µS/cm using NH_4OH and Amberlite resin, respectively. After resin removal via filtration, 129.2 µL of 1 mM APTMS was added drop-wise to the nanoparticle solution (with stirring). After 30 minutes, 201 µL of 2.7% sodium silicate was added slowly to the solution and stirred for 24 hours. The silica shell thickness was further increased by adding ethanol (final ratio of 1 part water to 4.4 parts ethanol). After 6 hours, 20 µL of 1 mM APTMS and 20 µL TEOS were added. The pH of the solution was increased to ~11 using concentrated ammonium hydroxide. After 16 hours, the $Ag@Au@SiO_2$ nanoparticles were centrifuged (45 minutes, 9383xg) three times with ethanol then three times with water. The $Ag@Au@SiO_2$ nanoparticles were then passed through Sephadex-50 column to remove Ag@Au nanoparticles that did not contain complete silica shells[2] and stored in ethanol until use. Silica shells were converted into silica membranes via an internal silica etching process induced at basic pH values. Because the $Ag@Au@SiO_2$ nanoparticles were stored in ethanol, the samples were triply centrifuged and redispersed in water to a concentration of 3 nM. Concentrated NH_4OH was added to the solution to induce internal etching.[1, 20] The reaction was quenched by adding 100 mM HNO_3 until the solution pH was ~6. Finally, the nanoparticles were washed 3 times in water and passed through a Sephadex-G50 column to remove defect particles. These samples exhibited average diameters of 81.4 ± 15.7 nm with an average silica shell thickness of 31.4 ± 15.9 nm

5.2.3 Transmission Electron Microscopy.

TEM was performed using a JEOL JEM-1230 microscope equipped with a Gatan

CCD camera. Samples were prepared on 400 mesh copper grids that were coated with a thin film of Formvar and carbon (Ted Pella). The nanoparticle solution was diluted in a 50% water−ethanol mixture, and ~10 μL of the solutions were pipetted onto grids and dried. At least 200 nanoparticles were analyzed (Image Pro Analyzer) to estimate average nanoparticle diameters, and average silica shell thicknesses were determined by calculating the differences between Ag@Au and Ag@Au@SiO_2 nanoparticle diameters (error is from propagated error in these measurements).

5.2.4 Extinction and SERS Spectroscopies.

Localized surface plasmon resonance (LSPR) spectra were collected using disposable methacrylate cuvette (pathlength = 1 cm) and an ultraviolet-visible (UV-vis) spectrometer (Ocean Optics USB4000). Either deuterium or halogen lamps were used for UV and visible excitation, respectively. LSPR spectra were collected in transmission geometry every minute for 2 hours (integration time = 60 msec, average = 25 scans, and boxcar = 10), and extinction maximum wavelengths (λ_{max}) were determined from the zero-point crossing of the first derivative. LSPR spectra were processed using MATLAB program. SERS measurements were performed using 6 nM IE Ag@Au@SiO_2 nanoparticles prepared in 10 mM phosphate buffer (pH 7.4) and mixed with various concentrations of 2-naphthalenethiol, benzenethiol, p-aminothiophenol, and 4-mercaptobenzoic acid. Prior to SERS measurements, samples were mixed and incubated for 1 hour. SERS data were collected using BW tek iRaman spectrometer with an excitation wavelength (λ_{ex}) of 785 nm. SERS spectra were processed using MATLAB program.

5.3 Results and Discussion

5.3.1 Layer Thickness and Molecular Orientation.

Thiols readily adsorb to gold surfaces and were used to evaluate how molecular size (benzenethiol vs. 2-naphthalenethiol) and functional group (benzenethiol vs. 4-mercaptobenzoic acid vs. p-aminothiophenol) impact monolayer formation. These molecules are shown in Figure 5.1A in their protonated/deprotonated states at pH 7.4. Previously, the packing densities of 2-naphthalenethiol, benzenethiol, 4-mercaptobenzoic acid, and p-aminothiophenol were shown to be 4.1,[1] 6.8,[30] 3.0,[31] and 2.8[32] x 10^{14} molecules/cm^2, respectively. These differences are attributed to variations in molecular tilt angle (θ) and molecule-molecule interactions as well as surface roughness and composition.

Because these packing densities depend on the composition and roughness of the substrate, changes in LSPR spectra of IE Ag@Au@SiO_2 nanoparticles (silica effective RI = 1.38_0) are used to evaluate molecular tilt angle as orientation of these molecules are important[33] in SERS studies. First, 6 nM concentrations of the nanomaterials are suspended in 10 mM phosphate buffer (pH 7.4). A representative TEM image of this sample is shown in Figure 5.1B. These materials contain relatively homogeneous Ag@Au nanoparticles, which serve as reproducible SERS substrates when encapsulated in internally etched silica membranes. The metal core is on average 18.5 ± 2.3 nm and the silica membrane is 31.4 ± 7.9 nm thick. Large variations in silica shell thickness are observed and attributed to residual metal reagents in solution prior to silica coating. Because of the porous silica membrane, the LSPR properties of the metal cores are electromagnetically stable. Here, we demonstrate that the pores in the silica membrane

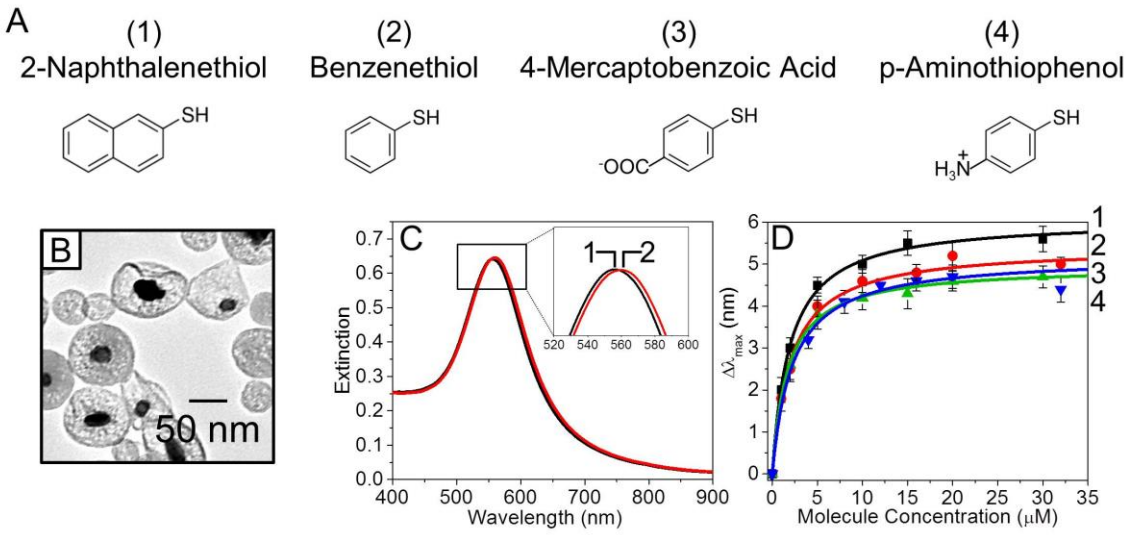

Figure 5.1. (A) Chemical structures of (1) 2-naphthalenethiol, (2) benzenethiol, (3) 4-mercaptobenzoic acid, and (4) p-aminothiophenol. (B) TEM image of internally etched Ag@Au@SiO_2 nanoparticles with nanoparticle diameter of 81.4 ± 15.7 nm and an effective refractive index of 1.38. (C) Representative LSPR spectra of internally etched Ag@Au@SiO_2 nanoparticles (1) before (black) and (2) after (red) incubation with the thiolated molecules. (D) Shifts in the λ_{max} of 6 nM IE Ag@Au@SiO_2 nanoparticles incubated for 1 hour in (1) 2-naphthalenethiol, (2) benzenethiol, (3) 4-mercaptobenzoic acid, and (4) p-aminothiophenol. Error bars represent the standard deviation of the $\Delta\lambda_{max}$ changes from at least three replicate measurements. Lines represent analysis using the Langmuir adsorption model.

are small enough and facilitate the diffusion of the previously described thiolated molecules.

To monitor molecular binding to the metal surface, changes in the LSPR spectra of the IE Ag@Au nanoparticles are used to monitor molecular binding and tilt angle. Previously, shifts in the LSPR wavelength maximum ($\Delta\lambda_{max}$) of metal nanoparticles were shown to provide an accurate measure of alkanethiol layer thickness.[34-36] Specifically, changes in $\Delta\lambda_{max}$ is related to local refractive index changes by the equation

$$\Delta\lambda_{max} = \lambda_{max,\ SAM} - \lambda_{bulk} = m\Delta n\ (1-e^{-\frac{2t}{l_d}}) \quad (5.1)$$

where $\lambda_{max,SAM}$ is the extinction maximum wavelength after SAM formation, λ_{bulk} is the extinction maximum wavelength before functionalization, m is the linear refractive index sensitivity of the nanoparticles (125 nm/RIU), Δn is the change in refractive index resulting from surface functionalization and is a difference of the refractive index of the SAM ($n_{SAM} = 1.65$)[37] and the nanoparticles prior to functionalization ($n_{eff,bulk} = 1.38$), t is the effective monolayer thickness (where t = maximum ligand layer thickness*cos(θ) and θ is the tilt angle of the SAM relative to the surface normal), and l_d is the local electromagnetic field decay length of the metal particles (11 nm). The maximum ligand thicknesses were previously determined to be 1.15 nm for benzenethiol and 2-naphthalenethiol and 1.5 the other two molecules.

Because shifts in the LSPR extinction maximum wavelength are isolated from electromagnetic coupling from near particles, LSPR data can be used to estimate effective monolayer thickness and tilt angles on the Ag@Au nanoparticle surfaces. To do this, 6

Table 5.1. Summary of SAM thicknesses and molecular tilt angles from LSPR analysis.

Molecule	Thickness (t)	Tilt angle (θ)
2-naphthalenethiol	1.1 nm	18°
benzenethiol	1.1_5 nm	0°
4-mercaptobenzoic acid	1.2 nm	36°
p-aminothiophenol	1.1_5 nm	40°

nM concentrations of the IE Ag@Au@SiO_2 nanoparticles are incubated in varying concentrations of the thiolated molecules for 1 hour and LSPR spectra are measured.

Example LSPR spectra before and after incubation with 30 μM p-aminothiophenol are shown in Figure 1C. The LSPR λ_{max} red shifts from 556.1 to 561.0 nm as molecules bind to the nanoparticle surfaces. The red shift in λ_{max} arises from an increase in local refractive index from molecular binding on the nanoparticles.[38] Notably, the only significant change in LSPR properties are these small variations in extinction maximum wavelength. As such, this demonstrates that IE Ag@Au@SiO_2 nanoparticles are electromagnetically stable, an important parameter for quantitative SERS studies.

In addition, these wavelength shifts depend on the composition and concentration of the thiolated molecules. These data are summarized in Figure 5.1D. Initially, increasing the molecular concentration causes the $\Delta\lambda_{max}$ to increase in magnitude for all molecules. Additional increases in concentration yield no additional changes in $\Delta\lambda_{max}$, which indicates that the metal surface is saturated by the molecules and no additional change in effective refractive index is observed. Importantly, the magnitude of the $\Delta\lambda_{max}$ at saturation, however, depends on molecule composition. These vary from 6.1, 5.4, 5.2, and 4.9 nm for 2-naphthalenethiol, benzenethiol, 4-mercaptobenzoic acid, and p-aminothiophenol, respectively. Using equation 1, the effective SAM thicknesses for the four molecules are ~1.1, 1.15, 1.2, 1.15 nm, respectively. In addition, tilt angles relative to the surface normal are estimated at ~18, 0, 36, and 40 °, respectively. SAM thickness and tilt angles calculated from LSPR analysis are summarized in Table 5.1. This suggests that 2-naphthalenethiol is slightly titled on the nanoparticle surface while benzenethiol forms a tight monolayer with a nearly perpendicular orientation relative to the surface. The charged molecules, however, exhibit significant tilt angles likely from the amine and carboxylic acid groups exhibiting some affinity for the metal surface. These results are

consistent with previous literature studies[23, 39-41] and this information can be used to understand the relative SERS enhancements of various vibrational modes associated with the thiolated molecules.

5.3.2 Molecular Adsorbate, Concentration, and Vibrational Mode Dependence.

Solution-phase nanoparticles are extensively used as SERS substrates but often fail at providing reproducible S/N for a given molecular concentration because of their dynamic optical properties[3] and sometimes poor solution-phase stabilities.[9] Furthermore, molecule orientation and surface selection rules can lead to often unexpected SERS intensities.[10-11, 23, 39-41] As shown in Figure 5.1, IE Ag@Au@SiO_2 nanoparticles do not exhibit electromagnetic coupling and are ideal for studying molecule concentration-dependent SERS intensity changes for 2-naphthalenethiol, benzenethiol, 4-mercaptobenzoic acid, and p-aminothiophenol. As a compromise, these substrates do not exhibit large hot-spots,[42-43] which give rise to large SERS enhancement factors and are difficult to control with solution-phase SERS substrates. As such, all SERS intensities reported represent averaged SERS signals from all molecules on the metal surface.[44]

Although all four molecules are structurally similar, SERS allows molecular identification using their unique vibrational modes. As in the LSPR studies, 6 nM IE Ag@Au@SiO_2 nanoparticles are incubated with 2-naphthalenethiol, benzenethiol, 4-mercaptobenzoic acid, and p-aminothiophenol for 1 hour to ensure equilibrium binding conditions. Additionally, the internal void volume and effective refractive index surrounding the nanomaterials (composed of silica and buffer) is maintained at 1.38 to ensure that the effective 3D SERS volume is maintained in all experiments.[45-46] As shown

in Figure 5.2, unique vibrational modes are observed for each molecule, and these agree well with previously reported vibrational frequencies. These vibrational modes are summarized in Table 5.2.

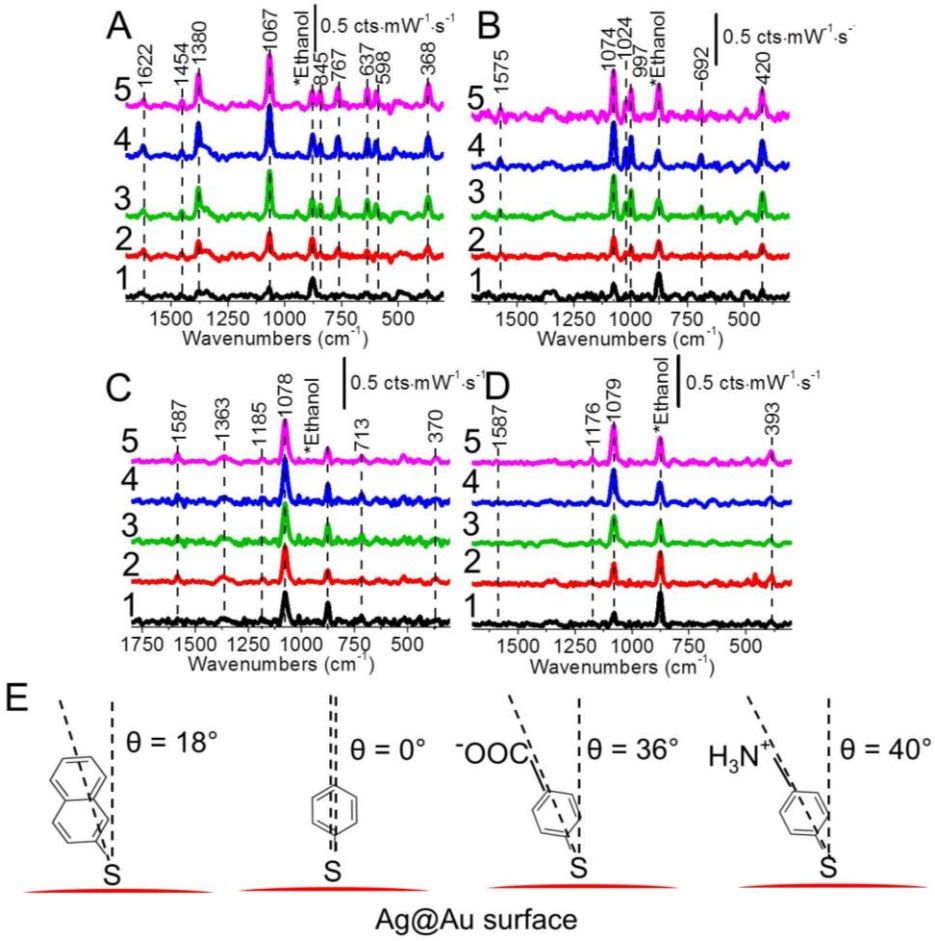

Figure 5.2. SERS spectra as a function of molecular concentration using 6 µM IE Ag@Au@SiO_2 nanoparticles with effective refractive index of 1.38. (A) SERS spectra for (1) 2, (2) 5, (3) 15, (4) 30, and (5) 40 µM 2-naphthalenethiol. (B) SERS spectra for (1) 2, (2) 5, (3) 10, (4) 20, and (5) 32 µM benzenethiol. (C) SERS spectra for (1) 4, (2) 8, (3) 12, (4) 20, and (5) 32 µM 4-mercaptobenzoic acid. (D) SERS spectra for (1) 1, (2) 2, (3) 5, (4) 20, and (5) 30 µM p-aminothiophenol. (E) Representative orientation of 2-naphthalenethiol, benzenethiol, 4-mercaptobenzoic acid, and p-aminothiophenol on Ag@Au surface. All vibrational mode assignments are found in Table 1. SERS parameters: λ_{ex} = 785 nm, t_{int} = 30 s, and P = 64 mW.

For instance, 2-naphthalenethiol shows the most vibrational modes in these SERS studies. Ring stretching and deformation modes are observed at 1622, 1454, and 1380 cm^{-1} and at 637 and 598 cm^{-1}, respectively. In addition, CH and CS vibrational modes are observed at 1067, 845, 767, and 368 cm^{-1}. Fewer bands are observed for the other three molecules because of ring differences. Many similarities and differences are noted. First, ring bending modes are more intense than ring and CC stretching modes. This suggests that molecules are oriented in a way that promotes the selective enhancement of certain vibrational modes as a result of their symmetry relative to the electric fields[10] and/or distance from the metal surface.[47] Second, symmetric CS stretches for 2-naphthalenethiol, benzenethiol, 4-mercaptobenzoic acid, and p-aminothiophenol are located at 1067, 1074, 1078, and 1079 cm^{-1}in SERS compared to 1083, 1093, 1073, and 1087 cm^{-1} in normal Raman (solution), respectively.[5-8, 12-13, 15] This vibrational mode is the most intense feature in all the molecules and are shifted compared to solution Raman indicating that these molecules are bound to the Ag@Au cores through the formation of a gold-sulfur bond. As such, this mode experiences the strongest electromagnetic fields that are located near the metal surface vs. the other functional groups and enhanced to the greatest degree.[48-50] Third, the CS bending mode exhibits molecule specific trends. An observable CS bending mode is observed at 368, 370, and 393 cm^{-1} for 2-naphthalenethiol, 4-mercaptobenzoic acid, and p-aminothiophenol, respectively.Surface selection rules can be used, once again, to explain this result.

Table 5.2. Vibrational frequency assignments for possible species present in these samples.

Molecule	Vibration Mode (symmetry)	Vibrational Frequency (cm^{-1})		Ref.
		Literature	This Work	
2-Napthalenethiol	Ring stretch	1621	1622	[6]
	Ring stretch	1452	1454	
	Ring stretch (a_1)	1378	1380	
	CH bend (b_2)/CS stretch (a_1)	1065	1067	
	CH twist (a_2)	842	845	
	CH wag	767	767	
	Ring deformation	639	637	
	Ring deformation	599	598	
	CS bend (b_2)	369	368	
Benzenethiol	Ring stretch (a_1)	1573	1575	[7-8]
	CS/CC stretch (a_1)	1073	1074	
	CH bend (a_1)	1020	1024	
	CCC in plane bend (a_1)	1000	997	
	CCC in plane bend/CS stretch (a_1)	691	692	
	CS stretch/CCC in plane bend (a_1, a_2)	417	420	
4-Mercaptobenzoic Acid	Ring stretch (a_1)	1588	1587	[12-13]
	COO^- stretch	1375	1363	
	CH in plane bend (a_1)	1182	1185	
	CS/CC stretch (a_1)	1077	1078	
	CCC out of plane bend	718	713	
	CS bend (b_2)	369	370	
p-Aminothiophenol	CH bend/CC stretch/CN stretch (a_1)	1587	1587	[15]
	CH bend (a_1)	1181	1176	
	CC/CS stretch (a_1)	1078	1079	
	CS bend (b_2)	391	393	

SERS spectral analysis of 2-naphthalenethiol molecule on Ag@Au surface indicate that peak ratio of the ring stretching mode at 1380 cm^{-1} and CS bending mode at 368 cm^{-1} to CS symmetric stretching mode are ~0.7 and 0.5 indicating that both modes

contribute to the polarizability tensor along the surface normal and significantly enhanced.[7, 11] In addition, CH twisting mode for 2-naphthalenethiol is also observed at 845 cm^{-1}. Enhancement of ring stretching, CS stretching, CS in plane bending, and presence of CH twisting vibrational modes indicate that 2-naphthalenethiol molecule is tilted along the surface normal.

In comparison, SERS spectra of benzenethiol at various concentrations indicate absence of vibrational modes of a_2 symmetry. Presence of ring stretching mode at 1575 cm^{-1};[7] strongly enhanced CH in plane bending mode at 1024 cm^{-1} (ratio of CH in plane bending to CS symmetric stretching vibration is ~0.5); and absence of a_2 symmetry mode[33] suggest that the benzenethiol orients nearly vertical to the surface as indicated by LSPR studies described above. Given the ~0 ° tilt angle estimated for benzenethiol on these metal surfaces, absence of CS bending indicate that this vibrational mode is likely occurring parallel to the metal surface and not enhanced.

SERS spectra of both 4-mercaptobenzoic acid and p-aminothiophenol show relatively weak enhancements for CH in plane bending mode compared to CS symmetric stretching (peak ratio ~0.1 – 0.15). Weaker SERS enhancements for these molecular vibrational modes indicate that the polarizability tensor associated with these vibrational modes exhibit only small contribution along the surface normal and are weakly enhanced. In addition, the non-zero but large tilt angles for CS bending mode associated with these molecules facilitate non-zero polarizability changes normal to the surface and are thus moderately enhanced. 4-mercaptobenzoic acid, in particular, reveals a broad spectral feature centered at 1363 cm^{-1}. This vibrational mode is consistent with a COO^- stretch and suggests that the carboxylic acid groups for these molecules are deprotonated[12-13] and

likely close to the metal surface (*i.e.*, because the molecules exhibit a large tilt angle). In addition, the ring breathing mode for p-aminothiophenol is only observable at the highest molecule concentrations and is very weak in the 4-mercaptobenzoic acid spectra further supporting the argument that these molecule exhibit large tilt angles relative to the surface normal, which would cause these in-plane totally symmetric vibrations to occur nearly parallel to the metal surface thus violating surface selection rules.[10] These spectral observations for both 4-mercaptobenzoic acid and p-aminothiophenol are consistent with predictions of large tilt angles for these same molecules in the previously discussed LSPR spectral analysis. Figure 5.2E summarizes molecular orientation of 2-naphthalenethiol, benzenethiol, 4-mercaptobenzoic acid, and p-aminothiophenol on Ag@Au surface determined from LSPR and SERS analysis. All of these results are consistent with ordered monolayer formation on the Ag@Au nanoparticle surfaces with tilt angles consistent with what was predicted from the LSPR data.

Now that the vibrational modes are understood with respect to their orientation relative to their surfaces, concentration dependent trends for each molecule are evaluated. Figure 5.2 shows representative SERS spectra while Figure 5.3 reveals spectral trends for distinct vibrational modes collected for various concentrations of 2-naphthalenethiol, benzenethiol, p-aminothiophenol, and 4-mercaptobenzoic acid incubated for one hour with the IE Ag@Au@SiO_2 nanoparticle samples. In general, similar concentration dependent trends are observed for each vibrational mode for a given molecule.

While the orientation (*i.e.*, tilt angle) of each molecule likely varies throughout these studies, all vibrational modes follow the Langmuir adsorption model. By fitting the data to this isotherm model, SERS intensity as a function of molecule concentration can

be estimated by the following equation

$$I_{SERS}=I_{SERS}^{max}\left[\frac{K_{eq}*C}{1+K_{eq}C}\right] \quad (2)$$

where I_{SERS} is a SERS intensity for a measurement, I_{SERS}^{max} is the maximum SERS intensity, K_{eq} is the equilibrium constant (in μM^{-1}), and C is the concentration of analyte added to the nanoparticle solution. This suggests that SERS signal response is related to

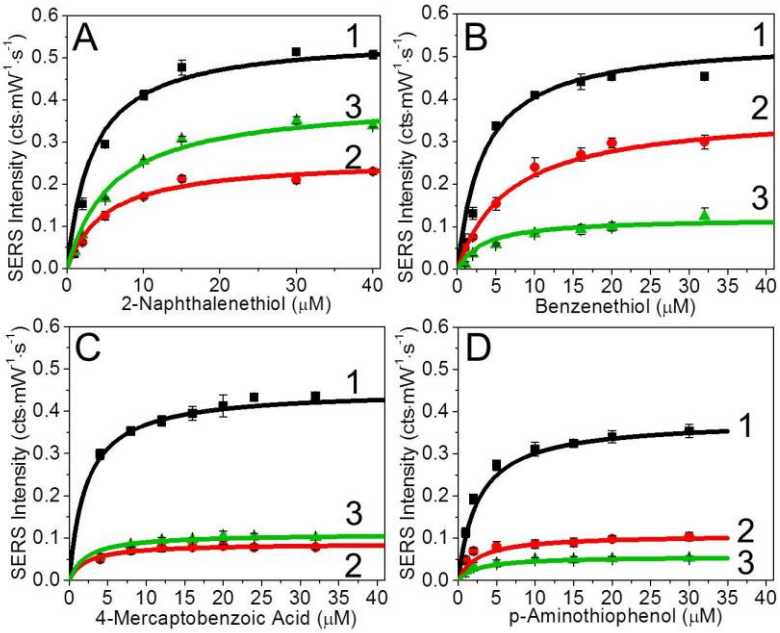

Figure 5.3. SERS signals as a function of molecular concentration and vibrational mode. (A) SERS intensity for (1) 1067 cm^{-1} (CH bend/CS stretch), (2) 368 cm^{-1} (CS bend), and (3) 1380 cm^{-1} (ring stretch) as a function of 2-naphthalenethiol concentration. (B) SERS intensity for (1) 1074 cm^{-1} (CS/CC symmetric stretch), (2) 420 cm^{-1} (CS stretch and CCC in plane bend), and (3) 1573 cm^{-1} (ring stretch) as a function of benzenethiol concentration. (C) SERS intensity for (1) 1078 cm^{-1} (CS/CC ring stretch), (2) 713 cm^{-1} (CCC out of plane bend), and (3) 1585 cm^{-1} (ring stretch) as a function of 4-mercaptobenzoic acid concentration. (D) SERS intensity for (1) 1079 cm^{-1} (CS stretch), (2) 393 cm^{-1} (CS bend), and (3) 1173 cm^{-1} (CH bend) as a function of p-aminothiophenol concentration. Averages and standard deviations represent those of 3 measurements. Same experimental conditions as in Figure 2.

the concentration of the analyte in a surface area (or SERS 3D volume) dependent manner. At the highest concentrations, these signals saturate suggesting surface saturation. This is consistent with previous studies that suggested that SERS signals are directly proportional to the number of molecules in the SERS volume until molecular saturation on metal surface occurs (assuming a fixed tilt angle).[51-53]

In addition, the magnitude of the vibrational mode intensities should depend on [7]both average molecule tilt angle and surface concentration. For fixed molecular tilt angle, SERS intensities depends on molecular surface concentration until SERS-active 3D volumes near metal core saturates. Figure 5.3 compares the magnitude for the vibrational mode for each molecule. SERS intensities increases initially as molecules occupy SERS-active volume and then signals saturate once ~monolayer forms on the surface. Similar trends are observed for all vibrational modes, but this discussion will focus on the vibrational mode with the largest SERS intensity for each molecule. As previously discussed, these are all associated with CS symmetric stretch. Specifically, these are centered at 1067 cm^{-1} (CH bend/CS stretch), 1074 cm^{-1}(CS/CC symmetric stretching), 1078 cm^{-1}(CS/CC ring stretching), and1079 cm^{-1}(CS stretching) for 2-naphthalenethiol, benzenethiol, 4-mercaptobenzoic acid, and p-aminothiophenol, respectively. Using the results from the Langmuir adsorption fits, the maximum theoretical SERS signals for this vibrational modes for the same molecules are ~0.55, 0.54, 0.45, and 0.38 $cts \cdot mW^{-1} \cdot s^{-1}$. Previously, the footprints of 2-naphthalenethiol, benzenethiol, 4-mercaptobenzoic acid, and p-aminothiophenol were estimated at 0.244 nm^2/molecule, 0.147 nm^2/molecule,[30] 0.332 nm^2/molecule,[31] and 0.359 nm^2/molecule[32], respectively.

If molecular footprints played a large role the maximum SERS intensity for benzenethiol would be the largest followed by 2-naphthalenethiol, 4-mercaptobenzoic acid, and p- aminothiophenol. The results for 2-naphthalenethiol and benzenethiol are similar and suggest that differences in tilt angle (and thus satisfying surface selection rules for this vibrational mode) likely give rise to these spectral differences as the

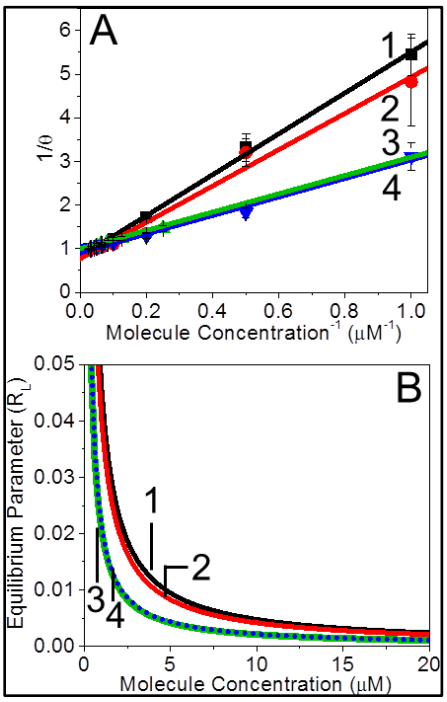

Figure 5.4. Langmuir adsorption isotherm analysis for CS stretching mode. (A) Linear transformations of the Langmuir adsorption isotherm fitted to SERS data and (B) equilibrium parameter calculations for (1) 2-naphthalenethiol, (2) benzenethiol, (3) 4-mercaptobenzoic acid, and (4) p-aminothiophenol.

footprints for these molecules differ by a factor of ~2. In addition, the maximum SERS intensities for benzenethiol, 4-mercaptobenzoic acid, and p-aminothiophenol follow tilt angle trends estimated from LSPR data (0, 36, and 40 º, respectively). This suggests that tilt angle and the symmetry of the vibrational modes play a major role in the magnitude

of the SERS signals.

5.3.3 Adsorption Isotherm Analysis.

The Langmuir adsorption isotherm model is one of the simplest and most widely used models to describe adsorption processes and assumes monolayer adsorption, homogeneous binding sites, no adsorbate – adsorbate interactions, and dynamic equilibrium between adsorbed and free molecules in the solution. While deviations from

Table 5.3. Langmuir adsorption isotherm results for CS stretching mode from the SERS data.

Molecule	Slope (M)	Intercept	R^2	Equilibrium adsorption constant, K_{eq} (M^{-1}) x 10^5	Gibbs free energy, ΔG_{ads} (kcal/mol)
2-Naphthalenethiol	4.7 ± 0.1	$0.8_2 \pm 0.0_4$	0.99	$2.1_3 \pm 0.0_5$	$-7.26 \pm 0.01_4$
Benzenethiol	4.2 ± 0.2	0.8 ± 0.1	0.98	2.4 ± 0.1	-7.34 ± 0.02
4-Mercaptobenzoic Acid	2.1 ± 0.1	$0.9_5 \pm 0.0_1$	0.98	4.7 ± 0.3	-7.75 ± 0.04
p-Aminothiophenol	2.1 ± 0.1	$0.9_2 \pm 0.0_3$	0.99	4.7 ± 0.2	-7.73 ± 0.02

Langmuir conditions are likely (reversible adsorption, heterogeneous binding sites with non-uniform adsorption affinities, and multilayer formation[54-55]), these deviations are estimated to be minimal. As such, the linearized form of the Langmuir adsorption isotherm can be used to provide information regarding equilibrium adsorption conditions using the following equation

$$\frac{1}{\theta} = 1 + \frac{1}{K_{eq}C} \tag{3}$$

where θ is the normalized SERS signal (I_{SERS}/I_{SERS}^{max}) for a particular vibrational mode and molecule, K_{eq} is the equilibrium adsorption constant, and C is the concentration of

analyte added to the nanoparticle solution.

Figure 5.4A shows linearly transformed Langmuir adsorption isotherms modeled for the CS symmetric stretch for 2-naphthalenethiol, benzenethiol, 4-mercaptobenzoic acid, and p-aminothiophenol. The results for these data are summarized in Table 5.3 and indicate Langmuir behavior. Using equation 3 and the slope determined from linear regression, the equilibrium adsorption constants can be calculated for 2-naphthalenethiol, benzenethiol, 4-mercaptobenzoic acid, and p-aminothiophenol and are estimated at 2.1×10^5, 2.4×10^5, 4.7×10^5, and 4.7×10^5 M^{-1}, respectively. Finally, a dimensionless constant commonly referred to as the equilibrium parameter (R_L)[56] can be defined by

$$R_L = \frac{1}{1 + K_{eq}C} \tag{4}$$

so that the favorability of adsorption can be defined. In general, unfavorable adsorption is

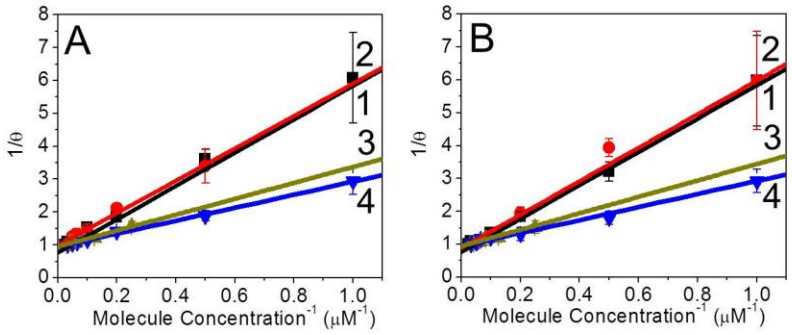

Figure 5.5. Langmuir adsorption isotherm model analysis. (A) Linear transformation of Langmuir model fitted to CC ring stretching mode at 1380, 1575, and 1587 cm^{-1} for (1) 2-naphthalenethiol, (2) benzenethiol, and (3) 4-mercaptobenzoic acid; and CH bending mode at 1176 cm^{-1} for (4) p-aminothiophenol. (B) Linear transformation of Langmuir model fitted to CS bending mode at 368 and 393 cm^{-1} for (1) 2-naphthalenethiol and (4) p-aminothiophenol; CCC in plane bend/CS stretching at 420 cm^{-1} for (2) benzenethiol; and CCC out of plane bending at 713 cm^{-1} for (3) 4-mercaptobenzoic acid. Correlation coefficient R^2 for Langmuir isotherms are at least 0.96. Calculated Langmuir isotherm parameters are listed in Table 5.4.

indicated by a R_L value greater than 1 ($R_L > 1$), favorable adsorption occurs when R_L is between 0 and 1 ($0 < R_L < 1$), and irreversible adsorption takes place when R_L is 0.[56] As shown in Figure 5.4B, this parameter is small (<0.05) for all molecule concentrations. As such, adsorption of all molecules to the Ag@Au nanoparticles is favorable and nearly irreversible. It should be noted that R_L is slightly smaller for 4-mercaptobenzoic acid and p-aminothiophenol indicating slightly more affinity for the metal surface relative to 2-naphthalenethiol and benzenethiol. To quantify these differences, the free energy of adsorption (ΔG_{ads}) is calculated using the equilibrium constant and $\Delta G_{ads} = - RT \ln K_{eq}$ (Table 5.3). Linear Langmuir fits for CS symmetric stretching mode indicate that the free energies for these molecules range from -7.26 – -7.75 kcal/mol. These values are similar

Table 5.4. Langmuir adsorption isotherm results from the SERS data.

Molecule	Vibrational mode	Equilibrium adsorption constant, K_{eq} (M^{-1}) $\times 10^5$	Gibbs free energy, ΔG_{ads} (kcal/mole)
2-naphthalenethiol	CC ring stretch at 1380 cm^{-1}	$1.9_1 \pm 0.0_5$	-7.20 ± 0.02
	CS bending at 368 cm^{-1}	$1.9_7 \pm 0.0_4$	$-7.21 \pm 0.01_3$
benzenethiol	CC ring stretch at 1380 cm^{-1}	2.0 ± 0.1	-7.22 ± 0.03
	CCC/CS stretching at 420 cm^{-1}	$1.8_7 \pm 0.1$	-7.19 ± 0.01
4-mercaptobenzoic acid	CC ring stretch at 1380 cm^{-1}	4.2 ± 0.3	-7.67 ± 0.04
	CCC out of plane bending at 713 cm^{-1}	$4.3_6 \pm 0.3$	-7.69 ± 0.04
p-aminothiophenol	CH bending at 1176 cm^{-1}	5.0 ± 0.1	-7.77 ± 0.03
	CS bending at 393 cm^{-1}	5.2 ± 0.4	-7.80 ± 0.05

to those previously observed for 1-octadecanethiol (-5.6 kcal/mole) and 1-octanethiol (-4.4 kcal/mole) on a flat gold surface.[57] Langmuir adsorption analysis of additional

vibrational modes other than CS symmetric stretching for these molecules are shown in Figure 5.5 and ΔG_{ads} listed in Table 5.4. The average ΔG_{ads} for 2-naphthalenethiol, benzenethiol, 4-mercaptobenzoic acid, and p-aminothiophenol calculated using three ΔG_{ads} values (3 vibrational modes analyzed) are 7.22 ± 0.03, 7.25 ± 0.08, 7.70 ± 0.04, and 7.76 ± 0.04 kcal/mol, respectively. Comparing ΔG_{ads} for the four molecules used in this study, the adsorption of 4-mercaptobenzoic acid or p-aminothiophenol is slightly more favorable vs. that of 2-naphthalenethiol and benzenethiol. This small, ~0.5 kcal/mol on average difference likely arises from weak London dispersion interactions between the molecules and the gold surface.[58] This slight favorability of 4-mercaptobenzoic acid and p-aminothiophenol to adsorb to the metal surface is likely because of the larger tilt angles these molecules possess relative to the surface.

5.4 Conclusion

In summary, the implications of molecular composition and concentration on molecular adsorption and SERS intensity were evaluated using LSPR spectroscopy, SERS, and Langmuir adsorption isotherm modeling. Four molecules, 2-naphthalenethiol, benzenethiol, p-aminothiophenol, and 4-mercaptobenzoic acid molecules were selected because they contain different molecular footprints and functionality. Internally etched silica coated Ag@Au nanoparticles with a fixed SERS-active void volume were used to ensure electromagnetic stability of the metal cores and molecular availability for SERS detection. First, shifts in the LSPR maximum wavelength were used to estimate molecular tilt angles for these ligands. 4-Mercaptobenzoic acid and p-aminothiophenol exhibited the largest tilt angles relative to benzenethiol. These differences were attributed to functional group differences in molecular density on the surface. Next, SERS was

evaluated as a function of molecule concentration. Multiple vibrational modes were observed for each molecule and exhibited similar adsorption behavior for each functional group. By comparing the maximum magnitude of the totally symmetric CS stretch for each molecule, the largest signals were observed for 2-naphthalenethiol and benzenethiol. Because these two molecules exhibit packing densities that differ by a factor of ~2, differences in the SERS intensity likely arise from differences in tilt angle where surface selection rules must be considered. In addition, the maximum SERS intensities were only slightly smaller for the two charged molecules. These differences were attributed to the large tilt angle of these molecules relative to the surface normal. This was confirmed through Langmuir adsorption isotherm modeling. Equilibrium constants and the free energy associated with adsorption associated with 4-mercaptobenzoic acid and p-aminothiophenol vs. 2-naphthalenethiol and benzenethiol. Binding was estimated to be more favorable for the two charged molecules vs. the others from likely London dispersion force stabilization between the ligands and the metal surface. All in all, these studies suggest that the SERS intensities observed for these thiolated ligands are highly sensitive to vibrational mode symmetry and their tilt angle relative to the nanoparticle surface. These differences were easily observed because of the optical stability and controlled adsorbate interactions with IE Ag@Au@SiO_2 nanoparticles. These optical properties and orientation dependencies could be used for future studies of other more complex molecules and trace detection.

1. Roca, M.; Haes, A. J., Silica-Void-Gold Nanoparticles: Temporally Stable Surface-Enhanced Raman Scattering Substrates. *J. Am. Chem. Soc.* **2008**, *130*, 14273-14279.
2. Pierre, M. C. S.; Haes, A. J., Purification Implications on Sers Activity of Silica Coated Gold Nanospheres. *Analytical Chemistry* **2012**, *84*, 7906-7911.

3. Pierre, M. C. S.; Mackie, P. M.; Roca, M.; Haes, A. J., Correlating Molecular Surface Coverage and Solution-Phase Nanoparticle Concentration to Surface-Enhanced Raman Scattering Intensities. *The Journal of Physical Chemistry C* **2011**, *115*, 18511–18517.
4. Volkert, A. A.; Pierre, M. C. S.; Shrestha, B.; Haes, A. J., Implications of Sample Aging on the Formation of Internally Etched Silica Coated Gold Nanoparticles. *RSC Advances* **2015**, *5*, 3774-3780.
5. Shi, X.-Z.; Shen, C.; Wang, D.-K.; Li, C.; Tian, Y.; Xu, Z.-C.; Wang, C.-M.; Gao, H., Surface-Enhanced Raman Scattering Properties of Highly Ordered Self-Assemblies of Gold Nanorods with Different Aspect Ratios. *Chin. Phys. B* **2011**, *20*, 1-7.
6. Alvarez-Puebla, R. A.; Dos Santos Jr, D. S.; Aroca, R. F., Surface-Enhanced Raman Scattering for Ultrasensitive Chemical Analysis of 1 and 2-Naphthalenethiols. *Analyst* **2004**, *129*, 1251-1256.
7. Carron, K. T.; Hurley, L. G., Axial and Azimuthal Angle Determination with Surface-Enhanced Raman Spectroscopy: Thiophenol on Copper, Silver, and Gold Metal Surfaces. *The Journal of Physical Chemistry* **1991**, *95*, 9979-9984.
8. Joo, T. H.; Kim, M. S.; Kim, K., Surface-Enhanced Raman Scattering of Benzenethiol in Silver Sol. *Journal of Raman Spectroscopy* **1987**, *18*, 57-60.
9. Wijenayaka, L. A.; Ivanov, M. R.; Cheatum, C. M.; Haes, A. J., Improved Parametrization for Extended Derjaguin, Landau, Verwey, and Overbeek Predictions of Functionalized Gold Nanosphere Stability. *The Journal of Physical Chemistry C* **2015**, *119*, 10064-10075.
10. Chowdhury, J., How the Charge Transfer (Ct) Contributions Influence the Sers Spectra of Molecules? A Retrospective from the View of Albrecht's "a" and Herzberg-Teller Contributions. *Applied Spectroscopy Reviews* **2014**, *50*, 240-260.
11. Moskovits, M.; Suh, J. S., Surface Selection Rules for Surface-Enhanced Raman Spectroscopy: Calculations and Application to the Surface-Enhanced Raman Spectrum of Phthalazine on Silver. *The Journal of Physical Chemistry* **1984**, *88*, 5526-5530.
12. Lee, S. B.; Kim, K.; Kim, M. S., Surface-Enhanced Raman Scattering of O-Mercaptobenzoic Acid in Silver Sol. *Journal of Raman Spectroscopy* **1991**, *22*, 811-817.
13. Michota, A.; Bukowska, J., Surface-Enhanced Raman Scattering (Sers) of 4-Mercaptobenzoic Acid on Silver and Gold Substrates. *Journal of Raman Spectroscopy* **2003**, *34*, 21-25.
14. Gao, X.; Davies, J. P.; Weaver, M. J., Test of Surface Selection Rules for Surface-Enhanced Raman Scattering: The Orientation of Adsorbed Benzene and Monosubstituted Benzenes on Gold. *The Journal of Physical Chemistry* **1990**, *94*, 6858-6864.
15. Huang, Y.-F.; Wu, D.-Y.; Zhu, H.-P.; Zhao, L.-B.; Liu, G.-K.; Ren, B.; Tian, Z.-Q., Surface-Enhanced Raman Spectroscopic Study of P-Aminothiophenol. *Physical Chemistry Chemical Physics* **2012**, *14*, 8485-8497.
16. Rodger, C.; Rutherford, V.; White, P. C.; Smith, W. E., Towards Quantitative Surface Enhanced Resonance Raman Scattering (Serrs): A Study of Aggregation and Concentration for Two Rhodamine Dyes. *Journal of Raman Spectroscopy* **1998**, *29*, 601-606.
17. Zhang, X.; Servos, M. R.; Liu, J., Surface Science of DNA Adsorption onto Citrate-Capped Gold Nanoparticles. *Langmuir* **2012**, *28*, 3896-3902.
18. Song, J.; Kong, H.; Jang, J., Adsorption of Heavy Metal Ions from Aqueous Solution by Polyrhodanine-Encapsulated Magnetic Nanoparticles. *Journal of Colloid and Interface Science* **2011**, *359*, 505-511.
19. Pettibone, J. M.; Cwiertny, D. M.; Scherer, M.; Grassian, V. H., Adsorption of Organic Acids on Tio2 Nanoparticles: Effects of Ph, Nanoparticle Size, and Nanoparticle Aggregation. *Langmuir* **2008**, *24*, 6659-6667.
20. Roca, M.; Mackie, P. M.; Haes, A. J., Design of a Biocompatible and Optically-Stable Solution-Phase Substrate for Sers Detection. *Mater. Res. Soc. Symp. Proc.* **2008**, *1133E*, No pp given.

21. Pastoriza-Santos, I. P.-J., J.; Liz-Marzan, L. M., Silica-Coating and Hydrophobation of Ctab-Stabilized Gold Nanorods. *Chem. Mater. FIELD Full Journal Title:Chemistry of Materials* **2006**, *18*, 2465-2467.
22. Zhan, Q.; Qian, J.; Li, X.; He, S., A Study of Mesoporous Silica-Encapsulated Gold Nanorods as Enhanced Light Scattering Probes for Cancer Cell Imaging. *Nanotechnology* **2010**, *21*, 1-12.
23. Ling, X.; Wu, J.; Xu, W.; Zhang, J., Probing the Effect of Molecular Orientation on the Intensity of Chemical Enhancement Using Graphene-Enhanced Raman Spectroscopy. *Small* **2012**, *8*, 1365-1372.
24. Srnova-Sloufova, I.; Vlckova, B.; Bastl, Z.; Hasslett, T. L., Bimetallic (Ag)Au Nanoparticles Prepared by the Seed Growth Method: Two-Dimensional Assembling, Characterization by Energy Dispersive X-Ray Analysis, X-Ray Photoelectron Spectroscopy, and Surface Enhanced Raman Spectroscopy, and Proposed Mechanism of Growth. *Langmuir* **2004**, *20*, 3407-3415.
25. Cui, Y.; Ren, B.; Yao, J.-L.; Gu, R.-A.; Tian, Z.-Q., Synthesis of Agcoreaushell Bimetallic Nanoparticles for Immunoassay Based on Surface-Enhanced Raman Spectroscopy. *The Journal of Physical Chemistry B* **2006**, *110*, 4002-4006.
26. Paramelle, D.; Sadovoy, A.; Gorelik, S.; Free, P.; Hobley, J.; Fernig, D. G., A Rapid Method to Estimate the Concentration of Citrate Capped Silver Nanoparticles from Uv-Visible Light Spectra. *Analyst* **2014**, *139*, 4855-4861.
27. Stober, W.; Finx, A.; Bohn, E., Controlled Growth of Monodisperse Silica Spheres in the Micron Size Range. *Journal of Colloid and Interface Science* **1968**, *26*, 62.
28. Liz-Marzan, L. M.; Giersig, M.; Mulvaney, P., Synthesis of Nanosized Gold-Silica Core-Shell Particles. *Langmuir* **1996**, *12*, 4329-4335.
29. Grzelczak, M.; Correa-Duarte, M. A.; Liz-Marzan, L. M., Carbon Nanotubes Encapsulated in Wormlike Hollow Silica Shells. *Small* **2006**, *2*, 1174-1177.
30. Haynes, C. L.; Van Duyne, R. P., Plasmon-Sampled Surface-Enhanced Raman Excitation Spectroscopy†. *The Journal of Physical Chemistry B* **2003**, *107*, 7426-7433.
31. Taylor, C. E.; Pemberton, J. E.; Goodman, G. G.; Schoenfisch, M. H., Surface Enhancement Factors for Ag and Au Surfaces Relative to Pt Surfaces for Monolayers of Thiophenol. *Appl. Spectrosc.* **1999**, *53*, 1212-1221.
32. Hayes, W. A.; Shannon, C., Electrochemistry of Surface-Confined Mixed Monolayers of 4-Aminothiophenol and Thiophenol on Au. *Langmuir* **1996**, *12*, 3688-3694.
33. Yoon, J. H.; Park, J. S.; Yoon, S., Time-Dependent and Symmetry-Selective Charge-Transfer Contribution to Sers in Gold Nanoparticle Aggregates. *Langmuir* **2009**, *25*, 12475-12480.
34. Jensen, T.; Kelly, L.; Lazarides, A.; Schatz, G. C., Electrodynamics of Noble Metal Nanoparticles and Nanoparticle Clusters. *Journal of Cluster Science* **1999**, *10*, 295-317.
35. Haes, A. J.; Van Duyne, R. P., A Nanoscale Optical Biosensor: Sensitivity and Selectivity of an Approach Based on the Localized Surface Plasmon Resonance Spectroscopy of Triangular Silver Nanoparticles. *J. Am. Chem. Soc.* **2002**, *124*, 10596-10604.
36. Jung, L. S.; Campbell, C. T.; Chinowsky, T. M.; Mar, M. N.; Yee, S. S., Quantitative Interpretation of the Response of Surface Plasmon Resonance Sensors to Adsorbed Films. *Langmuir* **1998**, *14*, 5636-5648.
37. Haes, A. J.; Zou, S.; Schatz, G. C.; Van Duyne, R. P., Nanoscale Optical Biosensor: Short Range Distance Dependence of the Localized Surface Plasmon Resonance of Noble Metal Nanoparticles. *The Journal of Physical Chemistry B* **2004**, *108*, 6961-6968.
38. Haes, A. J.; Van Duyne, R. P., A Nanoscale Optical Biosensor: Sensitivity and Selectivity of an Approach Based on the Localized Surface Plasmon Resonance

Spectroscopy of Triangular Silver Nanoparticles. *J. Am. Chem. Soc.* **2002**, *124*, 10596 - 10604.
39. Chulhai, D. V.; Jensen, L., Determining Molecular Orientation with Surface-Enhanced Raman Scattering Using Inhomogenous Electric Fields. *The Journal of Physical Chemistry C* **2013**, *117*, 19622-19631.
40. Janesko, B. G.; Scuseria, G. E., Surface Enhanced Raman Optical Activity of Molecules on Orientationally Averaged Substrates: Theory of Electromagnetic Effects. *The Journal of Chemical Physics* **2006**, *125*, 124704.
41. Wan, L.-J.; Terashima, M.; Noda, H.; Osawa, M., Molecular Orientation and Ordered Structure of Benzenethiol Adsorbed on Gold(111). *The Journal of Physical Chemistry B* **2000**, *104*, 3563-3569.
42. Li, W.; Camargo, P. H. C.; Lu, X.; Xia, Y., Dimers of Silver Nanospheres: Facile Synthesis and Their Use as Hot Spots for Surface-Enhanced Raman Scattering. *Nano Letters* **2009**, *9*, 485-490.
43. Kleinman, S. L.; Frontiera, R. R.; Henry, A.-I.; Dieringer, J. A.; Van Duyne, R. P., Creating, Characterizing, and Controlling Chemistry with Sers Hot Spots. *Physical Chemistry Chemical Physics* **2013**, *15*, 21-36.
44. Qian, X. M.; Nie, S. M., Single-Molecule and Single-Nanoparticle Sers: From Fundamental Mechanisms to Biomedical Applications. *Chem. Soc. Rev.* **2008**, *37*, 912-920.
45. Stoerzinger, K. A.; Lin, J. Y.; Odom, T. W., Nanoparticle Sers Substrates with 3d Raman-Active Volumes. *Chemical Science* **2011**, *2*, 1435-1439.
46. Lee, S.; Hahm, M. G.; Vajtai, R.; Hashim, D. P.; Thurakitseree, T.; Chipara, A. C.; Ajayan, P. M.; Hafner, J. H., Utilizing 3d Sers Active Volumes in Aligned Carbon Nanotube Scaffold Substrates. *Advanced Materials* **2012**, *24*, 5261-5266.
47. Kennedy, B. J.; Spaeth, S.; Dickey, M.; Carron, K. T., Determination of the Distance Dependence and Experimental Effects for Modified Sers Substrates Based on Self-Assembled Monolayers Formed Using Alkanethiols. *The Journal of Physical Chemistry B* **1999**, *103*, 3640-3646.
48. Zhu, Z.; Zhu, T.; Liu, Z., Raman Scattering Enhancement Contributed from Individual Gold Nanoparticles and Interparticle Coupling. *Nanotechnology* **2004**, *15*, 357-364.
49. Kim, K.; Lee, H. S., Effect of Ag and Au Nanoparticles on the Sers of 4-Aminobenzenethiol Assembled on Powdered Copper. *The Journal of Physical Chemistry B* **2005**, *109*, 18929-18934.
50. Hu, X.; Wang, T.; Wang, L.; Dong, S., Surface-Enhanced Raman Scattering of 4-Aminothiophenol Self-Assembled Monolayers in Sandwich Structure with Nanoparticle Shape Dependence: Off-Surface Plasmon Resonance Condition. *The Journal of Physical Chemistry C* **2007**, *111*, 6962-6969.
51. Olson, L. G.; Harris, J. M., Surface-Enhanced Raman Spectroscopy Studies of Surfactant Adsorption to a Hydrophobic Interface. *Applied Spectroscopy* **2008**, *62*, 149-156.
52. Haynes, C. L.; Yonzon, C. R.; Zhang, X.; Van Duyne, R. P., Surface-Enhanced Raman Sensors: Early History and the Development of Sensors for Quantitative Biowarfare Agent and Glucose Detection. *Journal of Raman Spectroscopy* **2005**, *36*, 471-484.
53. Izquierdo-Lorenzo, I.; García-Ramos, J. V.; Sanchez-Cortes, S., Vibrational Characterization and Surface-Enhanced Raman Scattering Detection of Probenecid Doping Drug. *Journal of Raman Spectroscopy* **2013**, *44*, 1422-1427.
54. Foo, K. Y.; Hameed, B. H., Insights into the Modeling of Adsorption Isotherm Systems. *Chemical Engineering Journal* **2010**, *156*, 2-10.
55. Vijayaraghavan, K.; Padmesh, T. V. N.; Palanivelu, K.; Velan, M., Biosorption of Nickel(Ii) Ions onto Sargassum Wightii: Application of Two-Parameter and Three-Parameter Isotherm Models. *Journal of Hazardous Materials* **2006**, *133*, 304-308.

56. Weber, T. W.; Chakravorti, R. K., Pore and Solid Diffusion Models for Fixed-Bed Adsorbers. *AIChE Journal* **1974**, *20*, 228-238.
57. Karpovich, D. S.; Blanchard, G. J., Direct Measurement of the Adsorption Kinetics of Alkanethiolate Self-Assembled Monolayers on a Microcrystalline Gold Surface. *Langmuir* **1994**, *10*, 3315-3322.
58. Andersson, M. P., Density Functional Theory with Modified Dispersion Correction for Metals Applied to Self-Assembled Monolayers of Thiols on Au(111). *Journal of Theoretical Chemistry* **2013**, *2013*, 9.

CHAPTER 6 IMPLICATIONS OF NANOPARTICLE CONCENTRATION, MORPHOLOGY, AND PLASMONIC PROPERTIES ON SERS INTENSITIES USING SILICA MEMBRANE STABILIZED COMPOSITE NANOPARTICLES

6.1 Introduction

Noble metal nanostructures exhibit tunable chemical and physical properties that are composition, shape, size, and surface chemistry dependent.[1] For instance, the optical properties of metal nanostructures exhibit unique extinction (absorption and scattering) spectra which arise from their localized surface plasmon resonance (LSPR). The LSPR occurs when incident electromagnetic radiation induces a collective oscillation of conduction band electrons on the nanoparticle surface.[2] Control over the composition, local dielectric environment, shape, size, and stability of solution-phase nanostructures is vital to their consistent application in various fields like optical sensors, biological diagnostics, and surface enhanced Raman scattering (SERS).[3] Surface-enhanced Raman scattering (SERS), in particular, takes advantage of the LSPR and increases the normal Raman signal of a given analyte by 2 to 9 orders of magnitude, thereby facilitating molecular detection at biologically relevant concentrations.[4] Thus, any changes in the LSPR of a solution-phase nanostructure affect SERS.

For a single SERS substrate, tuning Raman excitation over a range of visible wavelengths is an approach to determine which excitation wavelength generates maximum SERS;[5-7] however, maximizing SERS signals from nanostructures for a specific excitation wavelength is of particular interest for laboratories limited to a single Raman wavelength system or not having access to tunable Raman excitation systems. For

these laboratories, experimental studies that determine optimal excitation wavelength for maximizing SERS is, unfortunately, challenging. To overcome this limitation, tuning LSPR instead to determine which SERS substrate provide maximum SERS at a given excitation wavelength is a viable method. LSPR of solution phase nanostructures can easily be tuned from visible to near-IR by changing composition, shape, size, and surface chemistry.[1, 8] Gold coated silver nanoparticles are optically interesting for SERS because their LSPR properties can be tuned in visible range so that higher SERS enhancement can be achieved by overlapping LSPR with SERS excitation.[9-11]

Herein, implications of nanoparticle core morphology, concentration, and optical properties on SERS are studied. To ensure SERS signal changes observed can be attributed only to core composition, concentration, and LSPR properties, Au nanospheres and Ag@Au nanospheres are encapsulated in etched silica shells that prevent plasmon coupling. SERS signal at a fixed nanoparticle concentration but different nanoparticle core composition is studied using internally etched silica coated Au and Ag@Au nanoparticles. Next, three different internally etched Ag@Au@SiO_2 nanoparticle samples with various core diameter and LSPR wavelength maximum is used to study implication of LSPR properties (extinction at Raman excitation, and wavelength maximum closer to Raman excitation) on SERS. Finally, the contribution of charge transfer resonance on SERS intensities associated with internally etched silica coated Ag@Au nanoparticles is studied as a function of 3 different Raman excitation wavelengths.

6.2 Experimental Materials and Methods

6.2.1 Chemical Reagents

Gold(III) chloride trihydrate, sodium citrate dihydrate, Amberlite MB-150 mixed bed

exchange resin, (3-aminopropyl) trimethoxysilane (APTMS), sodium chloride (NaCl), sodium trisilicate (27%), tetraethyl orthosilicate (TEOS), silver perchlorate, sodium borohydride, and hydroxylamine hydrochloride were purchased from Sigma. Ethanol, ammonium hydroxide (NH_4OH), hydrochloric acid (HCl), and nitric acid (HNO_3) were purchased from Fisher Scientific (Pittsburgh, PA). Ultrapure water (18.2 MΩ cm^{-1}) was obtained from a Barnstead Nanopure System and used for all experiments. All glassware items were cleaned with aqua regia (3:1 HCl/ HNO_3) and rinsed thoroughly with water, and oven (glass) or air (plastic) dried overnight before use.

6.2.2 Gold and Silver@Gold Nanoparticle Synthesis

Gold nanoparticles were synthesized using well-established citrate reduction techniques.[12-15] Silver@Gold nanoparticles were synthesized using seeded growth method previously described in literature.[16-17] Briefly, 100 mL water containing 0.3 mM sodium citrate prepared in nitrogen-purged water stirred on an ice bath in the dark. Freshly prepared sodium borohydride solution in ice cold water was added onto the solution immediately following the preparation (final sodium borohydride concentration = 1 mM). Next, 1 mL of 10 mL of silver perchlorate was added to the solution within 2 minutes, and the resulting silver nanoparticles solution was stirred for 3 minutes. Stirring was stopped, and silver nanoparticles with average diameter ranging from 8 – 11 nm formed within 3 hours. After 3 hours of silver nanoparticle growth, the LSPR of silver nanoparticles was collected by diluting silver nanoparticle in half. Silver nanoparticles synthesized exhibited LSPR wavelength maximum between 393 – 397 nm.

Next, 20 mL of water was added to 25 mL of as-synthesized Ag seed stirred for ~2 minutes (4 °C). 15 mL of both 6.25 mM hydroxylamine hydrochloride and 0.465 mM

gold salt solution were added slowly (3 mL/min) using syringe pump. This Ag@Au nanoparticle solution was stirred for 1 hour to ensure nanoparticle formation and stored at 2 – 4 °C until use. The concentration of synthesized Ag@Au nanoparticle sample was estimated using a standard estimation model for the silver seeds using extinction spectroscopy.[18]

6.2.3 Microporous Silica-Coated Au and Ag@Au Nanoparticles Synthesis

Silica-coated gold ($Au@SiO_2$) nanoparticles were synthesized via a modified Stöber method.[15, 19-22] First, gold nanoparticles were synthesized using well-established citrate reduction techniques[12-15] and coated with varying silica shell thicknesses by modifying the sodium silicate concentration.[15, 21-22] Briefly, 150 mL of the gold nanoparticle stock solution was diluted with 150 mL of water. Amberlite resin was added to the diluted gold nanoparticles to reduce the ionic strength of the solution. The amberlite resin was then removed from the nanoparticle solution by filtration. The pH of the nanoparticle solution was adjusted to 5 using 1 M HCl. Next, the nanoparticle solution was divided into six samples of 50 mL each. The nanoparticle surfaces were made vitreophilic via the addition of 1 mM APTMS to obtain a 75% surface coverage. After 15 minutes, a 2.7 % sodium silicate solution of different concentrations was added to each sample flask to obtain various silica shell thicknesses, and the mixture was stirred for 24 hours. To induce the precipitation of unreacted silica the mixture was added to a final ratio of 1:4.4 water/ethanol. After 6 hours, the silica shells were thickened by adding a 1:1 concentrate ratio of TEOS/1 mM APTMS at a high pH (~11.0). The pH was adjusted with concentrated ammonium hydroxide. After 16 hours of incubation time, the

reaction was stopped and washed three times with ethanol to decrease the solution pH to 7. This was followed by another three washes with water to remove ethanol using centrifugation (30 min, 10 000 rpm).

Silica shells on Ag@Au nanoparticles were also synthesized via a modified Stöber method.[15, 19-22] Briefly, pH and conductivity of 25 mL as-synthesized Ag@Au nanoparticles were adjusted to 5 and ~110 µS/cm using NH_4OH and amberlite resin, respectively. After resin removal via filtration, 129.2 µL of 1 mM APTMS was added drop-wise to the nanoparticle solution (with stirring). After 30 minutes, 201 µL of 2.7 % sodium silicate solution was added slowly to the solution and stirred for 24 hours. The silica shell thickness was further increased by adding ethanol (final ratio of 1 part water to 4.4 parts ethanol). After 6 hours, 20 µL of 1 mM APTMS and 20 µL TEOS were added. The pH was increased to ~11 using concentrated ammonium hydroxide. After 16 hours, the $Ag@Au@SiO_2$ nanoparticles were centrifuged (45 min, 9383×g) three times with ethanol then 3 times with water. $Au@SiO_2$ and $Ag@Au@SiO_2$ nanoparticles were then passed through Sephadex-G50 column to remove nanoparticles that did not contain complete silica shells[23] and stored in ethanol until use.

6.2.4 Internally Etched Silica-Coated Nanoparticle Synthesis

Silica shells were converted into silica membranes via an internal silica etching process induced at basic pH values. Because the $Ag@Au@SiO_2$ was stored in ethanol, the samples were triply centrifuge and redispersed in water to a concentration of 6 nM for $Au@SiO_2$, 3 nM for $Ag@Au@SiO_2$, and 2 nM for $AuNR@SiO_2$ nanoparticles. Concentrated NH_4OH was added to the solution to induce internal etching. The reaction

was quenched by adding 100 mM HNO_3 until the solution pH was ~6. Finally, the nanoparticles were washed 3 times in water and passed through a Sephadex-G50 column to remove defect particles.

6.2.5 Extinction and SERS Spectroscopies

Localized surface plasmon resonance (LSPR) spectra were collected using a 0.67 cm path length disposable Raman cuvette and an ultraviolet-visible (UV-vis) spectrometer (Ocean Optics USB4000). LSPR of Ag nanoparticles were collected using deuterium light source where as other nanoparticle samples were illuminated with halogen lamp. Extinction maximum wavelengths (λ_{max}) were determined from the zero-point crossing of the first derivative of each spectrum using MatLab (MathWorks).

SERS spectra were collected simultaneously to the LSPR measurements at a 90° angle from the UV-vis light sources. SERS measurements were performed using nanoparticles dispersed in 10 mM phosphate buffer (pH 7.4) and p-aminothiophenol. Prior to SERS measurements, samples were mixed and incubated for at least 1 hour. SERS data were collected using Advantage (λ_{ex} = 632.8 nm) and Examiner (λ_{ex} = 785 nm).

6.2.6 Transmission Electron Microscopy (TEM)

TEM was performed using a JEOL JEM-1230 microscope equipped with a Gatan CCD camera. Samples were prepared on 400 mesh copper grids that were coated with a thin film of Formvar and carbon (Ted Pella). The nanoparticle solution was diluted in a 50% water−ethanol mixture. The solution (~10 μL) was pipetted onto a grid and dried. Over 200 nanoparticles were analyzed using Image Pro Analyzer to estimate the average diameter of the nanoparticle or length × width of nanorods.

6.3 Results and Discussion

6.3.1 LSPR Tuning of Silica Coated Nanoparticles

SERS takes advantage of the LSPR and increases the normal Raman signal by 2 to 9 orders of magnitude, thereby, facilitating molecular detection at biologically relevant concentrations.[4, 24-25] Maximizing SERS signals from nanostructures for a specific excitation wavelength is of particular interest because most laboratories could either be

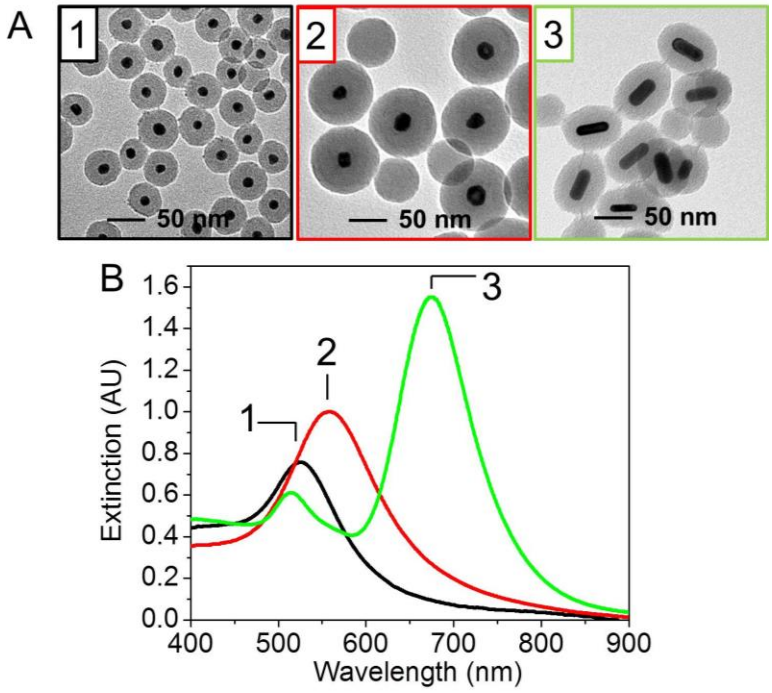

Figure 6.1. Characterization of silica coated Au nanospheres (1), Ag@Au nanospheres (2), and Au nanorods (3) using (A) TEM and (B) LSPR. TEM analysis show that silica is uniformly coated on the surface of nanoparticles. Dimensions of nanoparticles are (1) 45.3 ± 2.7 nm, (2) 87.1. ± 4.7 nm, and (3) 89.2 nm × 64.8 nm. LSPR analysis show tuneable extinction maximum wavelengths (λ_{max}) from Au nanospheres to Au nanorods. Extinction maximum wavelengths (λ_{max}) for silica coated nanoparticles are (1) 525.2 nm; (B) 560.1 nm; and (C) 673.4 nm.

limited to a single Raman wavelength system or not have access to tunable Raman excitation systems. For these laboratories, experimental studies that determines optimal excitation wavelength for maximizing SERS is, unfortunately, challenging. For a single SERS substrate, tuning Raman excitation over a range of visible wavelengths is reported as an approach to determine which excitation wavelength generates maximum SERS.[5-7] To overcome this limitation, tuning LSPR of SERS substrate instead is also a viable method. LSPR of solution phase nanostructures can easily be tuned from visible to near-IR by changing composition, shape, size, and surface chemistry.[1, 8]

Figure 6.1 show tunable property of silica coated nanostructures as the core is changed from gold to silver@gold or the shape is changed from gold nanosphere to gold nanorods. Silica coated gold nanoparticle exhibit LSPR at 525.2 nm compared to silica coated Ag@Au nanoparticle that exhibit LSPR at 560.1 nm. Ag@Au core-shell nanoparticles exhibit plasmon hybridization from both metals resulting in a newer LSPR band occurs at 560.1 nm. In comparison, Au nanorods that are synthesized using directional growth of spherical Au seeds exhibit longitudinal plasmon band centered at 673.4 nm and transverse plasmon band at 514.3 nm associated with the longer and shorter side of the nanorods. Longitudinal plasmon is more sensitive to the nanorod structure and the local dielectric environment than the transverse plasmon;[8, 26-28] therefore, longitudinal plasmon is monitored for Au nanorod samples. LSPR show plasmon tuneablility as nanoparticle core is changed from Au to Ag@Au or Au sphere to Au nanorods. Tuning nanoparticle plasmon is highly desirable for applications such as SERS,[5-7] optical antennas,[29] and sensors.[30-31] TEM images clearly depict structural variations of Au, Ag@Au nanoparticles, and Au nanorods. Silica uniformly coats nanostructures regardless

of variations in core composition or core symmetry. From TEM analysis the total dimension of silica coated nanoparticles are 45.3 ± 2.7 nm, 87.1 ± 4.7 nm, and 89.2 × 64.8 nm, respectively. Some silica spheres without nanoparticle cores are also observed in samples because limitations in sol-gel synthesis allows nucleation and growth of free silica.[15]

6.3.2 Implication of Nanoparticle Core Composition on SERS

Au and Ag nanoparticles are largely employed in SERS because of their LSPR.[3, 32] Both metal nanoparticles have their specific advantages and disadvantages. For example Au nanoparticles are easy to synthesize, possess higher structural homogeneity, and are biocompatible with antibody, antigen, DNA, or RNA functionalization compared to Ag nanoparticles.[17, 33-35] Ag nanoparticles on the other hand exhibit higher enhancement in the visible region[36] than Au nanoparticles but are prone to oxidation. Oxidation of Ag nanoparticles causes toxicity limiting their application in biological systems[37] and decreases SERS.[38] Ag@Au core-shell nanoparticles are ideal because these structures maintain the plasmon enhancement property of Ag core and

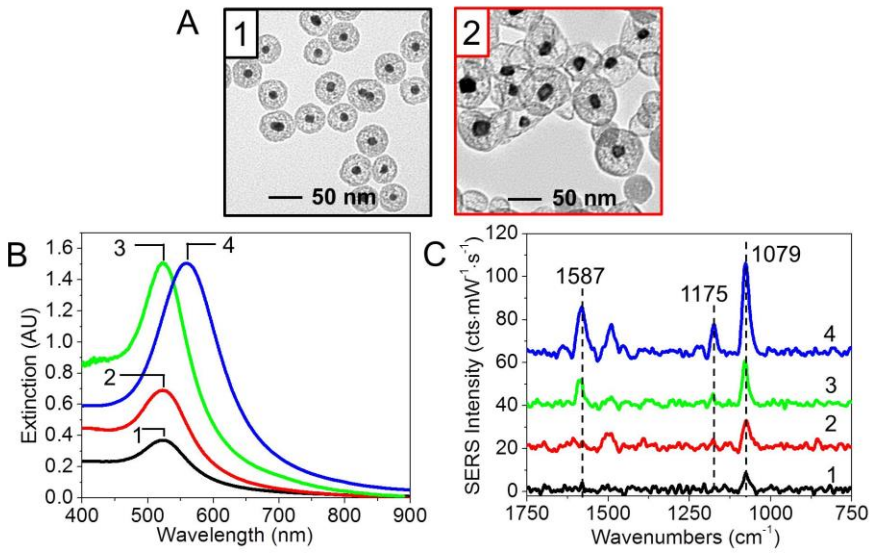

Figure 6.2. (A) TEM images of IE (1) $Au@SiO_2$ and (2) $Ag@Au@SiO_2$ nanoparticles. TEM analysis reveal that the average nanoparticle diameters are: (1) 44.6 ± 3.5 nm and (2) 69.6 ± 3.4 nm, with core diameters of (1) 12.6 ± 1.4 nm and (2) 17.7 ± 4.1 nm for IE $Au@SiO_2$ and $Ag@Au@SiO_2$ nanoparticles; respectively. LSPR (A) and SERS (B) analysis of (1) 2.5, (2) 4.9, and (3) 10.0 nM IE $Au@SiO_2$ nanoparticles; and (4) 2.5 nM IE $Ag@Au@SiO_2$ nanoparticles incubated with p-aminothiophenol monolayer for 1 hour. LSPR shows λ_{max} of (1 – 3) 522.6 and (4) 558.2 nm for IE $Au@SiO_2$ and IE $Ag@Au@SiO_2$ nanoparticles. Extinction at 632.8 nm are: (1) 0.076, (2) 0.15, (3) 0.29, and (4) 0.65 AU. The extinction at 632.8 nm for IE $Ag@Au@SiO_2$ nanoparticles is greater than IE $Au@SiO_2$ nanoparticles in all cases. SERS spectra show CS stretching mode of 4-aminothiophenol at 1079 cm^{-1} indicative of molecule binding to the metal surface through sulfur. IE $Ag@Au@SiO_2$ nanoparticle exhibit higher SERS S/N compared to IE $Au@SiO_2$ nanoparticles for a fixed (1) nanoparticle concentration, (2) total nanoparticle surface area, or (3) extinction at λ_{max}. SERS parameters: λ_{ex} = 632.8 nm, t_{int} = 10 s, and P = 2 mW.

biocompatibility/stability of Au shell.[17] Ag@Au core-shell nanoparticle structure is achieved synthetically by coating Au on Ag core using seed mediated growth process. Based on previous literature, the reduction of Au ions in the presence of Ag cores generally lead to the formation of Ag-rich core and Au-rich shell with some Ag-Au alloy formation.[16, 39-40] Because Ag and Au are miscible in all proportion (lattice constant

4.0862 and 4.0783 °A for Ag and Au, respectively)[40-41] but differ in redox potentials (+1.5 V for Au^0 vs. +0.8 V for Ag^0), studies show that synthetic strategies to generate either Ag-Au alloy or Ag@Au core-shell nanoparticles is not always predictable specially at Au:Ag mole fractions of < 0.4.[16] At Au:Ag mole fractions below 0.4, some degree of alloying occurs in the presence of Ag seed; however, increasing Au:Ag mole fraction above 0.4, Au-rich shell are obtained.[39, 42] This indicates that some degree of alloying can be controlled by the amount of Au precursor added. The dielectric function of the shell gradually approaches that of Au with increasing mole fraction of Au:Ag. The presence of Ag-Au alloy shells on Ag core can be observed as a shoulder between 400 – 500 nm using LSPR spectroscopy.[39] Absence of a notable shoulder below 500 nm in LSPR is attributed to Ag core and Au-rich shell nanoparticles (some degree of Ag-Au alloying is still present). Although rigorous understanding of core composition is important, the main goal here is correlation between IE Ag@Au@SiO_2 nanoparticle plasmonics on SERS.

To test the hypothesis that Ag@Au core provide higher SERS compared to Au, both Ag@Au and Au cores are encapsulated in internally etched silica membranes which prevents plasmon coupling so that any differences in signal enhancement can only be related to the chemical and electromagnetic enhancement mechanisms of isolated cores. Figure 6.2A depicts TEM images of IE Au@SiO_2 and IE Ag@Au@SiO_2 nanoparticles. TEM analysis show internally etched nanoparticles with void spaces that allow molecular diffusion and binding for SERS. Nanoparticles are uniformly coated with silica and no uncoated nanoparticles are present in both samples; so we can hypothesize that SERS signals observed can solely be attributed to plasmonic property of isolated nanoparticles.

The average core diameters are 12.6 ± 1.4 nm and 17.7 ± 4.1 nm for IE Au@SiO_2 and Ag@Au@SiO_2 nanoparticles. In addition, calculated average total diameters are 44.6 ± 3.5 nm and 69.6 ± 3.4 nm; respectively.

LSPR spectra of 2.5, 4.9, 10 nM IE Au@SiO_2 nanoparticles (1 – 3) and 2.5 nM IE Ag@Au@SiO_2 nanoparticles (4) are shown in Figure 6.2B. IE Au@SiO_2 nanoparticle samples are chosen to achieve fixed (1) concentration, (2) total metal surface area, and (3) extinction at λ_{max} compared to IE Ag@Au@SiO_2 nanoparticles. Molar extinction coefficient of 2×10^8 $M^{-1}\cdot cm^{-1}$ and 9.3×10^8 $M^{-1}\cdot cm^{-1}$ are used to calculate concentrations of IE Au@SiO_2 and Ag@Au@SiO_2 nanoparticles. Careful observation of IE Ag@Au@SiO_2 nanoparticle LSPR indicate no distinct shoulder between 400 – 500 nm indicating that shell is mainly composed of Au. Figure 6.2C shows SERS spectra of IE Au@SiO_2 and IE Ag@Au@SiO_2 nanoparticles collected by incubating with p-aminothiophenol monolayer for an hour. SERS spectra show characteristic CS stretching vibration of 4-aminothiophenol at 1079 cm^{-1} indicating that the molecules are adsorbed on to the metal surface through sulfur atom and enhanced by the strong electromagnetic fields near the metal surface.[43-45] CC ring stretching at 1587 cm^{-1} and CH bending at 1175 cm^{-1} are also observed. In addition CC stretching + CH bending mode at 1489 cm^{-1} is also observed in SERS spectrum of IE Ag@Au@SiO_2 nanoparticles. S/N calculated for 1079 cm^{-1} peak are: 15, 23, and 33 for 2.5, 4.9, 10 nM IE Au@SiO_2 nanoparticles compared to 37 for 2.5 nM IE Ag@Au@SiO_2 nanoparticles. It is clearly observed that S/N for IE Ag@Au@SiO_2 nanoparticles is higher in all three cases. Higher signal enhancement for IE Ag@Au@SiO_2 nanoparticles is attributed to strong near field plasmon enhancement compared to IE Au@SiO_2 nanoparticles.

6.3.3 Nanoparticle Concentration and Extinction at Raman Excitation Wavelength Implication on SERS

SERS optimization (i.e. maximum signal) is tremendously important for applications in biosensing, single molecular detection, and integration in nanodevices.[46-48] SERS optimization studies is sometimes challenging because the studies often require detailed correlation between LSPR and SERS. It is also important to control nanoparticle shape and size distributions to minimize inhomogeneous LSPR broadening[46] so that accurate prediction on SERS activity of a particular substrate is possible. SERS optimization studies on lithographically fabricated Ag nanotriangle[5-6] and Au nanorod[46] arrays show the importance of LSPR λ_{max} and Raman excitation wavelength (λ_{ex}) on SERS signal. These studies conclude that SERS signal from nanosubstrate is maximized when (1) LSPR λ_{max} is closer to λ_{ex} and (2) λ_{max} is in-between λ_{ex} and λ_{vib} (i.e. $\lambda_{max} \sim (\lambda_{ex} + \lambda_{vib})/2$). The above correlation between LSPR and SERS is reasonable because at plasmon resonance the interaction between the metal surface and external field is maximized;[49] therefore, it is expected that local electric-fields generated by LSPR and SERS should be maximized as well.

For solution-phase nanoparticles, correlating LSPR properties and SERS is challenging because nanoparticle undergo agglomeration/aggregation upon molecular adsorption. Hotspots in solution-phase nanostructures control the near-field SERS enhancement and the correlation between LSPR λ_{max} and maximum SERS is lost.[49] For example, it has been demonstrated that LSPR λ_{max} of single Ag colloids activated by salt and SERS signal generated are not correlated.[50] Correlating LSPR λ_{max} to maximum SERS of solution-phase nanoparticles with dynamic LSPR properties is difficult.

Internally etched silica coated Ag@Au nanoparticles are ideal to study plasmonic implication on solution-phase SERS because the core plasmonic properties are prevented from EM coupling.

Literature indicates that highest SERS is achieved when LSPR maximum is tuned closer to the excitation wavelength;[5] therefore, it is expected that SERS signal from nanostructures will increase as the LSPR λ_{max} is tuned towards 632.8 nm Raman excitation wavelength. By tuning the LSPR λ_{max} from 538.9 nm to 560.8 nm, the wavelength maximum gets closer to the Raman λ_{ex} which increases extinction at 632.8 nm for IE Ag@Au@SiO_2 nanoparticles. The increase in extinction at 632.8 nm increases energy coupling between LSPR and Raman excitation; thereby, increasing SERS signals.[51-52]

To test this hypothesis three IE Ag@Au@SiO_2 nanoparticle samples with different LSPR λ_{max} and Ag@Au diameters are synthesized. Figure 6.3 shows LSPR and TEM analysis of Ag, Ag@Au, and IE Ag@Au@SiO_2 nanoparticles. Ag nanoparticles exhibit λ_{max} at 394.6 nm with mean diameter of 13.1 ± 5.2 nm. Using same amount of Ag as seeds, various thickness of Au coating is performed by changing Au:Ag mole fraction from 0.74 – 0.85. Increasing Au:Ag mole fraction increases Au thickness on Ag seeds which is consistent with literature.[17, 40] Compared to Ag nanoparticles, Ag@Au nanoparticles exhibit plasmon peaks with λ_{max} that is characteristic of plasmon hybridization between Ag core and Au shell (Figure 6.3B). Increasing Au shell thickness initially shifts λ_{max} at longer wavelengths then blue shifts as Au thickness increases.[53] Coating synthesized Ag@Au nanoparticles with internally etched silica red shifts LSPR λ_{max} by 3.2 – 6.8 nm as the refractive index around metal core increases (Figure 6.3C).[54-

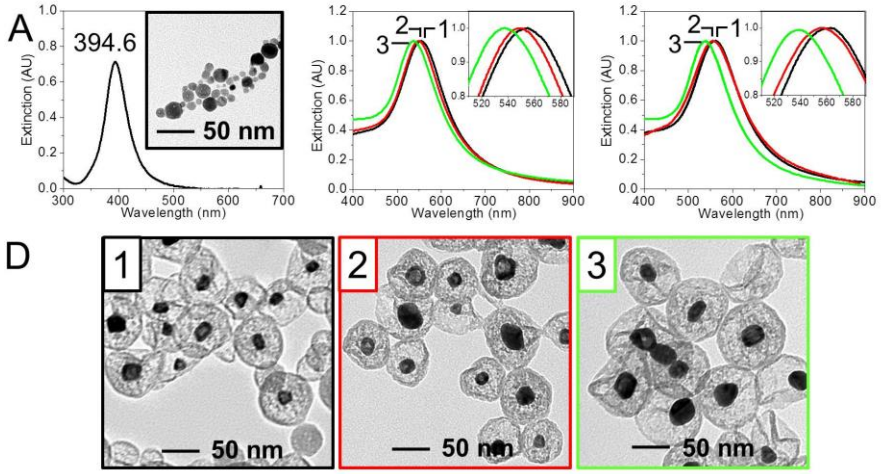

Figure 6.3. LSPR and TEM analysis of IE $Au@SiO_2$ nanoparticles. (A) Extinction spectrum of Ag nanoparticles used in synthesis of IE $Ag@Au@SiO_2$ nanoparticles. Ag nanoparticles show λ_{max} of 394.6 nm with Γ of 46.5 nm. Inset shows TEM image of Ag nanoparticles with average diameter = 13.1 ± 5.2 nm. (B) LSPR spectra of Ag@Au nanoparticles with various shell thicknesses synthesized from same Ag core. λ_{max} values are: (1) 554.1, (2) 549.0, and (3) 535.7 nm. (C) LSPR spectra of IE $Ag@Au@SiO_2$ nanoparticles etched for effective silica refractive index of ~1.38. λ_{max} of IE $Ag@Au@SiO_2$ nanoparticles are: (1) 560.8, (2) 555.8 , and (3) 538.9 nm. Insets in (B) and (C) clearly show differences in λ_{max} values for samples 1 – 3. TEM images of IE $Ag@Au@SiO_2$ nanoparticles with various Au shell thickness. (D) TEM analysis show that the average nanoparticle core diameters are: (1) 17.7 ± 4.1 nm, (2) 21.6 ± 6.7 nm, and (3) 26.0 ± 5.4 nm with total diameters of (1) 69.6 ± 13.4 nm, (2) 67.0 ± 8.3 nm, and (3) 76.9 ± 7.7 nm; respectively.

[55] The silica shell on nanoparticles are internally etched to achieve effective silica refractive index of ~ 1.38 using NH_4OH as described previously.[55-56] TEM images of internally etch $Ag@Au@SiO_2$ nanoparticles show silica membrane coated on all nanoparticles (Figure 6.3D – F). Calculated average core diameters are (1) 17.7 ± 4.1 nm, (2) 21.6 ± 6.7 nm, and (3) 26.0 ± 5.4 nm; with total diameters of (1) 69.6 ± 13.4 nm, (2) 67.0 ± 8.3 nm, and (3) 76.9 ± 7.7 nm for IE $Ag@Au@SiO_2$ nanoparticle samples with LSPR λ_{max} of (1) 560.8, (2) 555.8 , and (3) 538.9 nm; respectively. Few free silica shells

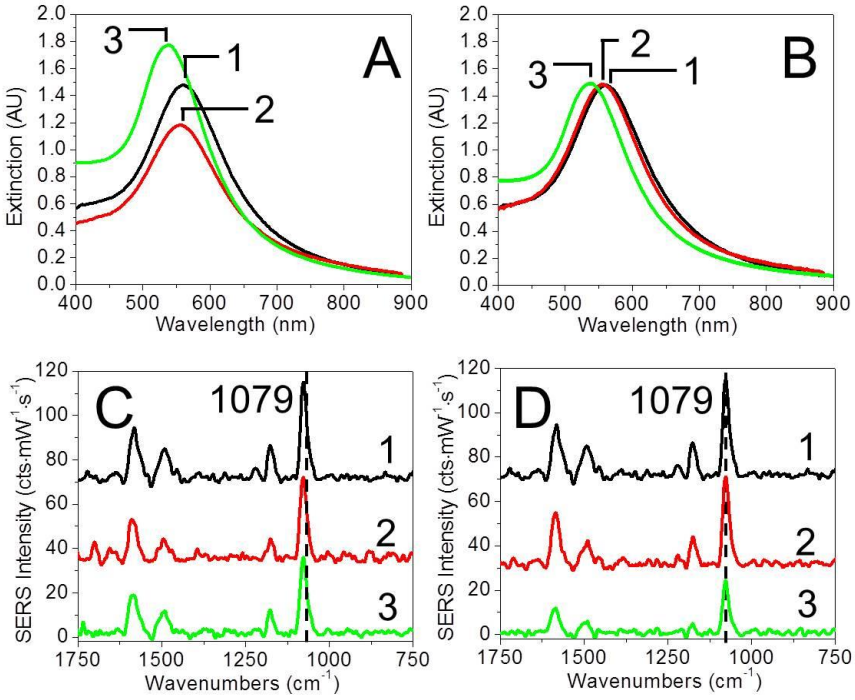

Figure 6.4. LSPR spectra of IE Ag@Au@SiO_2 nanoparticles for a fixed (A) nanoparticle concentration (= 2.5 nM) and (B) nanoparticle extinction (=1.5) at LSPR λ_{max}. λ_{max} values for IE Ag@Au@SiO_2 nanoparticles are: (1) 560.8, (2) 555.8 , and (3) 538.9 nm. Correlated SERS spectra collected by addition of monolayer p-aminothiophenol in IE Ag@Au@SiO_2 nanoparticles with a fixed (C) nanoparticle concentration and (D) nanoparticle extinction at LSPR λ_{max}. SERS parameters: λ_{ex} = 632.8 nm, t_{int} = 10 s, and P = 2 mW.

devoid of metal core also gets synthesized due to inherit limitations in silica sol-gel chemistry.

The extinction coefficients of the 3 different IE Ag@Au@SiO_2 nanoparticles with average diameters of (1) 17.7 ± 4.1 nm, (2) 21.6 ± 6.7 nm, and (3) 26.0 ± 5.4 nm are calculated based on 13.1 nm Ag core and Au:Ag mole fraction used assuming all the silver cores are coated with Au. The estimated extinction coefficients for the 3 samples are 9.3, 7.2, and 11.0 $\times 10^8$ $M^{-1}cm^{-1}$ at λ_{max}, respectively. SERS enhancement associated with IE Ag@Au@SiO_2 nanoparticles are modest (no aggregated hotspots); therefore,

understanding core composition and plasmonic implication on SERS are important because both these parameters influence SERS.[51-52, 57-58] Changing Au:Ag mole fraction or extinction @ Raman λ_{ex}, should allow increase in SERS signals for molecular detection and quantification using IE Ag@Au@SiO_2 nanoparticles.

To compare SERS intensities associated with a monolayer p-aminothiophenol on IE Ag@Au@SiO_2 nanoparticles with three different core diameters, either nanoparticle concentration or extinction at λ_{max} are kept constant. Figure 6.4 A and B show LSPR spectra of 3 different IE Ag@Au@SiO_2 nanoparticle samples where nanoparticle concentration or extinction @ λ_{max} are fixed. Figure 6.4 C and D depict respective SERS spectra for 3 different IE Ag@Au@SiO_2 nanoparticle samples with fixed nanoparticle concentration or extinction @ λ_{max}. Table 6.1 summarizes nanoparticle concentration, extinction @ Raman λ_{ex}, and SERS intensities of CS stretching mode observed by incubating IE Ag@Au@SiO_2 nanoparticle samples with a monolayer p-aminothiophenol for an hour. Table 6.1 shows that error in estimating nanoparticle concentration is 48 – 50% that arises from diameter heterogeneity in both Ag and Ag@Au nanoparticles and assumption that Ag@Au nanoparticles are spherical. If nanoparticle concentration is the sole factor in SERS, then CS stretching mode intensities of monolayer p-aminothiophenol for all 3 IE Ag@Au@SiO_2 nanoparticle samples should be the same. SERS spectral analysis indicate that IE Ag@Au@SiO_2 nanoparticle with core diameter of 17.7 nm exhibit higher SERS intensities compared both 21.6 or 26.0 nm core diameters because the extinction @ Raman λ_{ex} (0.80 AU) is greater than other two nanoparticle samples. This observation supports the argument that increasing extinction @ Raman λ_{ex} increases energy coupling between LSPR and Raman excitation; thereby, increasing SERS. Both

Baron and Zhong groups studied extinction implication by either changing analyte concentration on Ag colloids or changing size of Au nanosphere to tune extinction at Raman λ_{ex} and observed similar results.[52, 58] In contrast both 21.6 nm and 26.0 nm core diameter IE Ag@Au@SiO_2 nanoparticle samples exhibit similar extinction @ Raman λ_{ex} (0.60 – 0.62 AU). It is expected that SERS intensities for CS stretching mode of p-aminothiophenol for both samples at fixed nanoparticle concentrations should be the same assuming extinction at Raman λ_{ex} rule. No significant difference in SERS

Table 6.1. Concentration, extinction @ Raman λ_{ex}, and SERS intensities for CS stretching mode of p-aminothiophenol on IE Ag@Au@SiO_2 nanoparticles with 3 different Ag@Au core diameters.

Ag@Au Diameter (nm)	Concentration (nM)	Extinction @ 632.8 nm (AU)	SERS @ 1079 cm^{-1} ($cts \cdot mW^{-1} \cdot s^{-1}$)	Fixed
(1) 17.7 ± 4.1	2.5 ± 1.2	0.80 ± 0.03	44.2 ± 1.3	Concentration
(2) 21.6 ± 6.7	2.5 ± 1.3	0.60 ± 0.04	38.1 ± 1.4	
(3) 26.0 ± 5.4	2.5 ± 1.3	0.62 ± 0.02	35.4 ± 1.8	
(1) 17.7 ± 4.1	2.5 ± 1.2	0.80 ± 0.03	44.2 ± 1.3	Extinction @ λ_{max}
(2) 21.6 ± 6.7	3.1 ± 1.5	0.74 ± 0.05	40.4 ± 0.9	
(3) 26.0 ± 5.4	2.0 ± 1.0	0.50 ± 0.02	25.1 ± 2.1	

intensities (within standard error) is observed for 21.6 nm and 26.0 nm core diameter IE Ag@Au@SiO_2 nanoparticles at fixed concentrations.

Second, the implication of extinction at λ_{max} for IE Ag@Au@SiO_2 nanoparticles on SERS is studied by fixing extinction of each samples at ~1.5 AU. Appropriate stock concentrations of 3 different IE Ag@Au@SiO_2 samples are diluted in 10 mM phosphate

buffer (pH 7.4) to achieve extinction at λ_{max} ~1.5 AU. As seen in Table 6.1, fixing nanoparticle extinction at λ_{max} changes both nanoparticle concentration and extinction at Raman λ_{ex} for samples (1) – (3); however, we hypothesize that concentration differences of 0.5 nM between IE Ag@Au@SiO_2 nanoparticle samples exhibit minimum change in SERS intensities. As can be observed in Table 6.1 for a fixed extinction at λ_{max}, SERS intensity for IE Ag@Au@SiO_2 nanoparticles with 21.6 nm core diameter (3.1 nM nanoparticle concentration) is 3.8 cts·mW^{-1}·s^{-1} smaller than 17.7 nm core diameter IE Ag@Au@SiO_2 nanoparticles (2.5 nM). The λ_{max} of 17.7 nm core sample is 5.0 nm shifted towards Raman excitation; therefore, the difference in SERS intensities between the two IE Ag@Au@SiO_2 nanoparticle samples is attributed to plasmon coupling at Raman excitation wavelength. SERS intensity for 26.0 nm core diameter IE Ag@Au@SiO_2 nanoparticles (sample 3) with λ_{max} shifted away from Raman excitation and lowest extinction at Raman excitation wavelength possess the smallest SERS intensity compared to the other two samples when extinction is fixed at λ_{max}. These data suggest that SERS intensities for these 3 IE Ag@Au@SiO_2 nanoparticles correlates with extinction at Raman λ_{ex} and minimally with nanoparticle concentration chosen for this study; therefore, tuning λ_{max} towards Raman excitation to achieve greater plasmonic coupling plays significant role in maximizing modest SERS signals associated with IE Ag@Au@SiO_2 nanoparticles.

6.3.4 Charge Transfer Resonance Implication on p-Aminothiophenol SERS

SERS arises from two mechanisms namely (1) chemical and (2) electromagnetic enhancement resulting from adsorbate and nanoparticle interactions.[59-60] The chemical mechanism is a short-range effect (< 2 nm)[61-63] and contribute up to 2 orders of

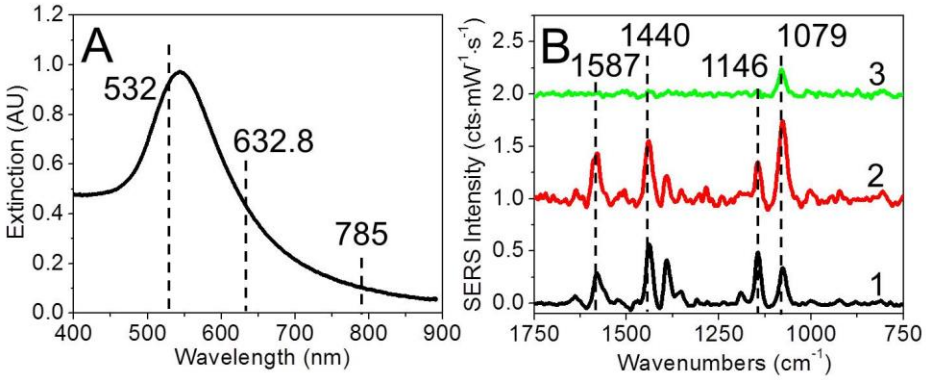

Figure 6.5. (A) LSPR of IE Ag@Au@SiO_2 nanoparticles incubated in 10 µM 4-aminothiophenol for 96 hours. LSPR λ_{max} of the sample is 544.1 nm. Dotted lines represent Raman excitation wavelengths at 532, 632.8, and 785 nm used to generate SERS signals. (B) SERS spectra collected with (1) 532, (2) 632.8, and (3) 785 nm Raman excitation systems. SERS spectra shown are normalized with 1049 cm^{-1} ethanol peak in order to account for differences in detector response. It is observed that 633 nm Raman excitation system provides highest SERS; whereas, 1079 cm^{-1} peak signal is smallest with 785 nm Raman excitation system. SERS parameters: λ_{ex} = 532 nm (LP = 9.1 mW), 632.8 nm (LP = 2 mW), 785 nm (LP = 60 mW), and t_{int} = 10 s.

magnitude signal enhancement.[24, 64] In contrast electromagnetic enhancement is long range effect and can contribute up to 9 orders of signal enhancement.[63, 65] Chemical enhancement contribute less to the overall SERS enhancement; however, chemical enhancement significantly alters SERS spectral pattern in terms of vibrational peak shifts and relative peak intensities. Understanding the implication of chemical enhancement on

SERS is important to deduce vibrational modes that are selectively enhanced so that quantitative and reproducible SERS is achieived. To study chemical enhancement effect on SERS of a single IE Ag@Au@SiO_2 nanoparticle sample, 3 different Raman excitation wavelengths are employed.

Figure 6.5 shows LSPR and SERS spectra of IE Ag@Au@SiO_2 nanoparticles after 96 hour incubation with a monolayer concentration of p-aminothiophenol. LSPR exhibit λ_{max} of 544.1 nm and dotted lines represent three Raman excitation wavelengths (λ_{ex}) at 532, 632.8, and 785 nm in the visible spectrum. Nanoparticle λ_{max} is closest to 532 nm Raman excitation while further away from 785 nm excitation. SERS spectra show various enhancement of p-aminothiophenol vibrational modes collected using 3 different Raman excitation sources. SERS spectra exhibit strong CS stretching mode at 1079 cm^{-1} in all cases as expected for the vibrational mode that is closest to the metal surface. In addition, SERS spectra collected from 532 and 632.8 nm excitation also exhibit strong CC stretch at 1587, combination CC stretch + CH bend at 1440 and 1391, and CH bend at 1146 cm^{-1}; respectively. SERS spectra are normalized using 1049 cm^{-1} ethanol peak to account for differences in detector sensitivities. For CS stretching mode at 1079 cm^{-1}, calculated λ_{vib} using 532, 632.8, and 785 nm Raman excitation are 564, 679, and 857 nm; respectively. Figure 6.5B show that SERS signal for CS stretch is highest for 632.8 nm Raman excitation; however, SERS signal for CC stretch + CH bending (1440 cm^{-1}) is greater for 532 nm Raman excitation. Clearly, relative SERS intensities for various p-aminothiophenol vibrational modes changes as a function of Raman excitation wavelengths. These spectral variations especially for b_2 modes that exhibit changes in relative intensities compared to CS stretch (a_1) are attributed to

chemical enhancement arising from molecule-metal interactions.[66] Charge transfer resonance (a form of chemical enhancement) is associated with the excited state of the molecule-metal system and the transfer of charge between the molecule and the metal surface allowing chemical SERS.[66-68] Figure 6.6 shows energy level diagram of metal and

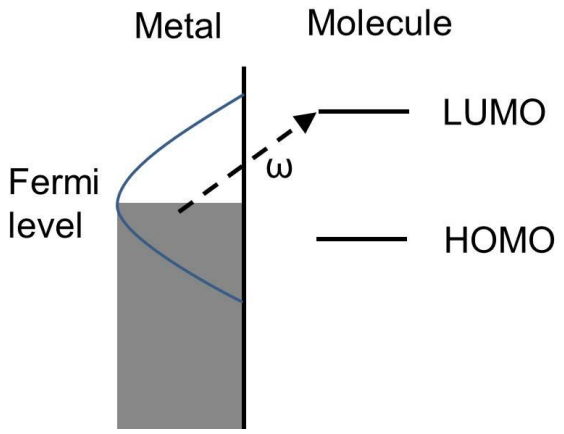

Figure 6.6. Diagram of charge transfer resonance mechanism in SERS. The charge transfer occurs from metal energy state closer to the Fermi level to LUMO of p-aminothiophenol.

molecule system. In charge transfer resonance SERS of p-aminothiophenol, the charge transfer transition occurs from metal states near the Fermi level to the LUMO state of p-aminothiophenol.[69] Resonance of excitation wavelength with the charge transfer transition generates signal enhancement through chemical mechanism.

As metal-molecule charge transfer resonance occur in p-aminothiophenol adsorbed on to Ag@Au surface, vibrational modes of b_2 symmetry such as 1146 cm^{-1},

Table 6.2. Frequencies (cm^{-1}) and relative SERS intensities of b_2 vibrational modes for p-aminothiophenol on IE $Ag@Au@SiO_2$ nanoparticles.

Vibrational modes (b_2)	SERS on IE $Ag@Au@SiO_2$ (cm^{-1})	Relative intensity vs. CS stretch (a_1) mode at 1079 cm^{-1}		
		785 nm	632.8 nm	532 nm
CC stretch + CH bend	1440 cm^{-1}	0.27	0.77	1.61
CC stretch + CH bend	1391 cm^{-1}	0.13	0.36	1.18
CH bend	1146 cm^{-1}	0.25	0.53	1.38

1391 cm^{-1}, and 1440 cm^{-1} are strongly influenced by charge transfer compared to a_1 symmetry modes such as 1079 cm^{-1}.[69-71] Summary of relative SERS intensities of b_2 modes compared to CS stretch (a_1) is included in Table 6.2. It is clear from the table that relative SERS intensities of b_2 modes changes as a function of excitation wavelength. Specifically, increase in relative intensity of b_2 more compared to CS stretch (a_1) mode occurs as the excitation wavelength decreases from 785 to 532 nm. This observation indicates that charge transfer resonance effect is favored at lower excitation wavelengths. Yoon and coworkers argued that selective enhancement of only b_2 symmetry modes for p-aminothiophenol is not a consequence of molecular orientation alone and that the SERS signals for b_2 modes increases after 10 hours and maximizes after 100 hours of p-aminothiophenol incubation on aggregated Au nanoparticles.[70] Changes in SERS signals of b_2 symmetry in Figure 6.5; therefore, is attributed to charge transfer[69-71] than molecular orientation changes. Density functional theory calculations of p-aminothiophenol bound

to Au through thiol end show the energy gap between the HOMO and LUMO of molecule-metal system to be 2.368 eV (524 nm) compared to 5.334 eV (232 nm) for free p-aminothiophenol.[70] This is consistent with our observation that SERS signal for b2 vibrational modes are higher using 532 than 632.8 nm Raman excitation wavelengths. Raman excitation wavelength of 785 nm is far from being in resonance with HOMO-LUMO gap of molecule-metal system for IE Ag@Au@SiO_2 nanoparticles; therefore, no selective enhancement of b_2 vibrational modes is observed consistent with work done by Dorpe and coworkers on Au nanorings.[72]

6.3.5 Conclusion

In conclusion, the implication of nanoparticle core morphology, and nanoparticle LSPR wavelength maximum on SERS were studied using internally etched silica coated gold nanospheres and silver@gold nanospheres. Optical properties of nanostructures were tuned in visible wavelength range by changing the core composition to Au or Ag coated with various Au thicknesses. Higher SERS enhancement was observed for internally etched silica coated Ag@Au nanospheres compared to internally etched silica coated Au nanospheres because of higher plasmon enhancement effect of Ag@Au core. It was found that higher SERS signal was obtained for IE Ag@Au@SiO_2 nanoparticles with thinnest gold thickness that exhibited LSPR maximum shifted towards Raman excitation so that better plasmon coupling at Raman excitation wavelength occured. In addition, implication of charge transfer resonance on variations in SERS spectra were also studied using Raman excitation wavelengths at 532, 632.8, and 785 nm. It was observed that selective b_2 vibrational modes associated with p-aminothiophenol were selectively enhanced as the Raman excitation wavelength decreased to 532 nm and was

consistent with literature. Core morphologies, optical properties, and charge transfer resonance implications on SERS spectral changes can be used to improve modest SERS intensities associated with solution-phase IE Ag@Au@SiO_2 nanoparticles which is important for direct, quantitative, and reproducible SERS.

1. Claridge, S. A. L., H.W.; Basu,S.R.; Fr?het,J.M.J.; Alivisatos,A.P, Isolation of Discrete Nanoparticle-DNA Conjugates for Plasmonic Applications. *Nano Lett.* **2008**, *8*, 1202-1206.
2. Haes, A. J.; Haynes, C. L.; McFarland, A. D.; Schatz, G. C.; Van Duyne, R. P.; Zou, S., Plasmonic Materials for Surface-Enhanced Sensing and Spectroscopy. *MRS Bulletin* **2005**, *30*, 368-375.
3. Pierre, M. C. S.; Mackie, P. M.; Roca, M.; Haes, A. J., Correlating Molecular Surface Coverage and Solution-Phase Nanoparticle Concentration to Surface-Enhanced Raman Scattering Intensities. *The Journal of Physical Chemistry C* **2011**, *115*, 18511–18517.
4. Alvarez-Puebla, R. A.; Arceo, E.; Goulet, P. J. G.; Garrido, J. J.; Aroca, R. F., Role of Nanoparticle Surface Charge in Surface-Enhanced Raman Scattering. *J. Phys. Chem. B* **2005**, *109*, 3787-3792.
5. Haynes, C. L.; Van Duyne, R. P., Plasmon-Sampled Surface-Enhanced Raman Excitation Spectroscopy. *J. Phys. Chem. B* **2003**, *107*, 7426-7433.
6. McFarland, A. D.; Young, M. A.; Dieringer, J. A.; VanDuyne, R. P., Wavelength-Scanned Surface-Enhanced Raman Excitation Spectroscopy. *J. Phys. Chem. B* **2005**, *109*, 11279-11285.
7. Kwon, Y.-H.; Ossig, R.; Hubenthal, F.; Kronfeldt, H.-D., Influence of Surface Plasmon Resonance Wavelength on Sers Activity of Naturally Grown Silver Nanoparticle Ensemble. *J. Raman Spect.* **2012**, *43*, 1385-1391.
8. Orendorff, C. J.; Murphy, C. J., Quantitation of Metal Content in the Silver-Assisted Growth of Gold Nanorods. *J. Phys. Chem. B* **2006**, *110*, 3990 - 3994.
9. Bright, R. M.; Musick, M. D.; Natan, M. J., Preparation and Characterization of Ag Colloid Monolayers. *Langmuir* **1998**, *14*, 5695-5701.
10. Freeman, R. G., et al., Self-Assembled Metal Colloid Monolayers: An Approach to Sers Substrates. *Science* **1995**, *267*, 1629-1632.
11. Orendorff, C. J.; Gearheart, L.; Jana, N. R.; Murphy, C. J., Aspect Ratio Dependence on Surface Enhanced Raman Scattering Using Silver and Gold Nanorod Substrates. *Phys. Chem. Chem. Phys.* **2006**, *8*, 165-170.
12. Okada, N.; Hamanaka, Y.; Nakamura, A.; Pastoriza-Santos, I.; Liz-Marzan, L. M., Linear and Nonlinear Optical Response of Silver Nanoprisms: Local Electric Fields of Dipole and Quadrupole Plasmon Resonances. *J. Phys. Chem.* **2004**, *108*, 8751-8755.
13. Pierre, M. C. S.; Mackie, P. M.; Roca, M.; Haes, A. J., Correlating Molecular Surface Coverage and Solution-Phase Nanoparticle Concentration to Surface-Enhanced Raman Scattering Intensities. *J. Phys. Chem. C* **2011**, *115*, 18511-18517.
14. Grabar, K. C.; Freeman, R. G.; Hommer, M. B.; Natan, M. J., Preparation and Characterization of Au Colloid Monolayers. *Anal. Chem.* **1995**, *67*, 735-43.
15. Roca, M.; Haes, A. J., Silica-Void-Gold Nanoparticles: Temporally Stable Surface-Enhanced Raman Scattering Substrates. *J. Am. Chem. Soc.* **2008**, *130*, 14273-14279.

16. Srnova-Sloufova, I.; Vlckova, B.; Bastl, Z.; Hasslett, T. L., Bimetallic (Ag)Au Nanoparticles Prepared by the Seed Growth Method: Two-Dimensional Assembling, Characterization by Energy Dispersive X-Ray Analysis, X-Ray Photoelectron Spectroscopy, and Surface Enhanced Raman Spectroscopy, and Proposed Mechanism of Growth. *Langmuir* **2004**, *20*, 3407-3415.
17. Cui, Y.; Ren, B.; Yao, J.-L.; Gu, R.-A.; Tian, Z.-Q., Synthesis of Agcoreaushell Bimetallic Nanoparticles for Immunoassay Based on Surface-Enhanced Raman Spectroscopy. *The Journal of Physical Chemistry B* **2006**, *110*, 4002-4006.
18. Paramelle, D.; Sadovoy, A.; Gorelik, S.; Free, P.; Hobley, J.; Fernig, D. G., A Rapid Method to Estimate the Concentration of Citrate Capped Silver Nanoparticles from Uv-Visible Light Spectra. *Analyst* **2014**, *139*, 4855-4861.
19. Stober, W.; Fink, A.; Bohn, E., Controlled Growth of Monodisperse Silica Spheres in the Micron Size Range. *J. Coll. Interface Sci.* **1968**, *26*, 62-69.
20. Liz-Marzán, L. M.; Giersig, M.; Mulvaney, P., Homogeneous Silica Coating of Vitreophobic Colloids. *Chemical Communications* **1996**, 731-732.
21. Liz-Marzan, L. M.; Giersig, M.; Mulvaney, P., Synthesis of Nanosized Gold-Silica Core-Shell Particles. *Langmuir* **1996**, *12*, 4329-4335.
22. Grzelczak, M.; Correa-Duarte, M. A.; Liz-Marzan, L. M., Carbon Nanotubes Encapsulated in Wormlike Hollow Silica Shells. *Small* **2006**, *2*, 1174-1177.
23. Pierre, M. C. S.; Haes Amanda, J., Purification Implications on Sers Activity of Silica Coated Gold Nanospheres. *Anal Chem* **2012**, *84*, 7906-7911.
24. Jeanmaire, D. L.; Van Duyne, R. P., Surface Raman Spectroelectrochemistry. Part I. Heterocyclic, Aromatic, and Aliphatic Amines Adsorbed on the Anodized Silver Electrode. *J. Electroanal. Chem. & Interfac. Electrochem.* **1977**, *84*, 1-20.
25. Fang, P.; Li, J. F.; Yang, Z.; Li, L. M.; Ren, B.; Tian, Z., Optimization of Sers Activities of Gold Nanoparticles
and Gold-Core–Palladium-Shell Nanoparticles
by Controlling Size and Shell Thickness. *J. Raman Spect.* **2008**, *39*, 1679-1687.
26. Sharma, V.; Park, K.; Srinivasarao, M., Colloidal Dispersion of Gold Nanorods: Historical Background, Optical Properties, Seed-Mediated Synthesis, Shape Separation and Self-Assembly. *Mater. Sci. Eng. Rep.* **2009**, *R65*, 1-38.
27. Wijaya, A.; Hamad-Schifferli, K., Ligand Customization and DNA Functionalization of Gold Nanorods Via Round-Trip Phase Transfer Ligand Exchange. *Langmuir* **2008**, *24*, 9966-9969.
28. Gou, L.; Murphy, C. J., Fine-Tuning the Shape of Gold Nanorods. *Chem. Mater.* **2005**, *17*, 3668-3672.
29. Alu, A.; Engheta, N., Tuning the Scattering Response of Optical Nanoantennas with Nanocircuit Loads. *Nat Photon* **2008**, *2*, 307-310.
30. Lee, K.-S.; El-Sayed, M. A., Gold and Silver Nanoparticles in Sensing and Imaging: Sensitivity of Plasmon Response to Size, Shape, and Metal Composition. *The Journal of Physical Chemistry B* **2006**, *110*, 19220-19225.
31. Mayer, K. M.; Hafner, J. H., Localized Surface Plasmon Resonance Sensors. *Chemical Reviews* **2011**, *111*, 3828-3857.
32. Sánchez-Cortés, S.; García-Ramos, J. V.; Morcillo, G., Morphological Study of Metal Colloids Employed as Substrate in the Sers Spectroscopy. *J. Coll. Interface Sci.* **1994**, *167*, 428-436.
33. Mirkin, C. A.; Letsinger, R. L.; Mucic, R. C.; Storhoff, J. J., A DNA-Based Method for Rationally Assembling Nanoparticles into Macroscopic Materials. *Nature* **1996**, *382*, 607- 609.
34. Sutherland, W. S.; Winefordner, J. D., Colloid Filtration: A Novel Substrate Preparation Method for Surface-Enhanced Raman Spectroscopy. *J. Coll. Interface Sci.* **1992**, *148*, 129-141.
35. Mann, S.; Shenton, W.; Li, M.; Connolly, S.; Fitzmaurice, D., Biologically Programmed Nanoparticle Assembly. *Adv. Mat.* **2000**, *12*, 147-150.

36. Laserna, J. J., Combining Fingerprinting Capability with Trace Analytical Detection: Surface-Enhanced Raman Spectrometry. *Anal. Chim. Acta* **1993**, *283*, 607-622.
37. Bright, R. M.; Walter, D. G.; Musick, M. D.; Jackson, M. A.; Allison, K. J.; Natan, M. J., Chemical and Electrochemical Ag Deposition onto Preformed Au Colloid Monolayers: Approaches to Uniformly-Sized Surface Features with Ag-Like Optical Properties. *Langmuir* **1996**, *12*, 810-817.
38. Han, Y.; Lupitskyy, R.; Chou, T.-M.; Stafford, C. M.; Du, H.; Sukhishvili, S., Effect of Oxidation on Surface-Enhanced Raman Scattering Activity of Silver Nanoparticles: A Quantitative Correlation. *Anal. Chem.* **2011**, *83*, 5873-5880.
39. Boote, B.; Byun, H.; Kim, J.-H., One-Pot Synthesis of Various Ag–Au Bimetallic Nanoparticles with Tunable Absorption Properties at Room Temperature. *Gold Bulletin* **2013**, *46*, 185-193.
40. Srnová-Šloufová, I.; Lednický, F.; Gemperle, A.; Gemperlová, J., Core−Shell (Ag)Au Bimetallic Nanoparticles: Analysis of Transmission Electron Microscopy Images. *Langmuir* **2000**, *16*, 9928-9935.
41. Mulvaney, P.; Giersig, M.; Henglein, A., Electrochemistry of Multilayer Colloids: Preparation and Absorption Spectrum of Gold-Coated Silver Particles. *The Journal of Physical Chemistry* **1993**, *97*, 7061-7064.
42. Moskovits, M.; Srnová-Šloufová, I.; Vlčková, B., Bimetallic Ag–Au Nanoparticles: Extracting Meaningful Optical Constants from the Surface-Plasmon Extinction Spectrum. *The Journal of Chemical Physics* **2002**, *116*, 10435-10446.
43. Zhu, Z.; Zhu, T.; Liu, Z., Raman Scattering Enhancement Contributed from Individual Gold Nanoparticles and Interparticle Coupling. *Nanotech.* **2004**, *15*, 357-364.
44. Kim, K.; Lee, H. S., Effect of Ag and Au Nanoparticles on the Sers of 4-Aminobenzenethiol Assembled on Powdered Copper. *The Journal of Physical Chemistry B* **2005**, *109*, 18929-18934.
45. Hu, X.; Wang, T.; Wang, L.; Dong, S., Surface-Enhanced Raman Scattering of 4-Aminothiophenol Self-Assembled Monolayers in Sandwich Structure with Nanoparticle Shape Dependence: Off-Surface Plasmon Resonance Condition. *The Journal of Physical Chemistry C* **2007**, *111*, 6962-6969.
46. Félidj, N.; Aubard, J.; Lévi, G.; Krenn, J. R.; Hohenau, A.; Schider, G.; Leitner, A.; Aussenegg, F. R., Optimized Surface-Enhanced Raman Scattering on Gold Nanoparticle Arrays. *Appl. Phys. Lett.* **2003**, *82*, 3095-3097.
47. Haes, A. J.; Van Duyne, R. P., A Nanoscale Optical Biosensor: Sensitivity and Selectivity of an Approach Based on the Localized Surface Plasmon Resonance Spectroscopy of Triangular Silver Nanoparticles. *J. Am. Chem. Soc.* **2002**, *124*, 10596 - 10604.
48. Kneipp, K.; Wang, Y.; Kneipp, H.; Perelman, L. T.; Itzkan, I.; Dasari, R. R.; Feld, M. S., Single Molecule Detection Using Surface-Enhanced Raman Scattering (Sers). *Phys. Rev. Lett.* **1997**, *78*, 1667-1670.
49. Doherty, M. D.; Murphy, A.; Pollard, R. J.; Dawson, P., Surface-Enhanced Raman Scattering from Metallic Nanostructures: Bridging the Gap between the near-Field and Far-Field Responses. *Physical Review X* **2013**, *3*, 011001.
50. Michaels, A. M.; Nirmal, M.; Brus, L. E., Surface Enhanced Raman Spectroscopy of Individual Rhodamine 6g Molecules on Large Ag Nanocrystals. *J. Am. Chem. Soc.* **1999**, *121*, 9932-9939.
51. Sow, I.; Grand, J.; Lévi, G.; Aubard, J.; Félidj, N.; Tinguely, J. C.; Hohenau, A.; Krenn, J. R., Revisiting Surface-Enhanced Raman Scattering on Realistic Lithographic Gold Nanostripes. *The Journal of Physical Chemistry C* **2013**, *117*, 25650-25658.
52. Njoki, P. N.; Lim, I. I. S.; Mott, D.; Park, H.-Y.; Khan, B.; Mishra, S.; Sujakumar, R.; Luo, J.; Zhong, C.-J., Size Correlation of Optical and Spectroscopic Properties for Gold Nanoparticles. *The Journal of Physical Chemistry C* **2007**, *111*, 14664-14669.

53. Yang, Y.; Shi, J.; Kawamura, G.; Nogami, M., Preparation of Au–Ag, Ag–Au Core–Shell Bimetallic Nanoparticles for Surface-Enhanced Raman Scattering. *Scripta Materialia* **2008**, *58*, 862-865.
54. Volkert, A. A.; Pierre, M. C. S.; Shrestha, B.; Haes, A. J., Implications of Sample Aging on the Formation of Internally Etched Silica Coated Gold Nanoparticles. *RSC Advances* **2015**, *5*, 3774-3780.
55. Roca, M.; Haes, A. J., Silica-Void-Gold Nanoparticles: Temporally Stable Surf Ace-Enhanced Raman Scattering Substrates. *J. Am. Chem. Soc.* **2008**, *130*, 14273-14279.
56. Volkert, A. A.; Subramaniam, V.; Haes, A. J., Implications of Citrate Concentration During the Seeded Growth Synthesis of Gold Nanoparticles. *Chem. Commun.* **2011**, *47*, 478-480.
57. Hong, S.; Li, X., Optimal Size of Gold Nanoparticles for Surface-Enhanced Raman Spectroscopy under Different Conditions. *Journal of Nanomaterials* **2013**, *2013*, 9.
58. Lecomte, S.; Matejka, P.; Baron, M. H., Correlation between Surface Enhanced Raman Scattering and Absorbance Changes in Silver Colloids. Evidence for the Chemical Enhancement Mechanism. *Langmuir* **1998**, *14*, 4373-4377.
59. Jensen, L.; Aikens, C. M.; Schatz, G. C., Electronic Structure Methods for Studying Surface-Enhanced Raman Scattering. *Chem. Soc. Rev.* **2008**, *37*, 1061-1073.
60. McCreery, R. L., *Raman Spectroscopy for Chemical Analysis*, 1 ed.; John Wiley & Sons, Inc.: New York, 2000; Vol. 157, p 420.
61. Caldwell, W. B.; Chen, K.; Herr, B. R.; Mirkin, C. A.; Hulteen, J. C.; Van Duyne, R. P., Self-Assembled Monolayers of Ferrocenylazobenzenes on Au(111)/Mica Films: Surface-Enhanced Raman Scattering Response Vs Surface Morphology. *Langmuir* **1994**, *10*, 4109-15.
62. Dick, L. A.; McFarland, A. D.; Haynes, C. L.; Van Duyne, R. P., Metal Film over Nanosphere (Mfon) Electrodes for Surface-Enhanced Raman Spectroscopy (Sers): Improvements in Surface Nanostructure Stability and Suppression of Irreversible Loss. *J. Phys. Chem. B* **2002**, *106*, 853-860.
63. Harpster, M. H., et al., Sers Detection of Indirect Viral DNA Capture Using Colloidal Gold and Methylene Blue as a Raman Label. *Biosens. Bioelectron.* **2009**, *25*, 674-681.
64. Dick, L. A.; McFarland, A. D.; Haynes, C. L.; Van Duyne, R. P., Metal Film over Nanosphere (Mfon) Electrodes for Surface-Enhanced Raman Spectroscopy (Sers): Improvements in Surface Nanostructure Stability and Suppression of Irreversible Loss. *J. Phys. Chem. B* **2002**, *106*, 853-860.
65. McMahon, J. A.; Wang, Y. M.; Sherry, L. J.; Van Duyne, R. P.; Marks, L. D.; Gray, S. K.; Schatz, G. C., Correlating the Structure, Optical Spectra, and Electrodynamics of Single Silver Nanocubes. *J. Phys. Chem. C* **2009**, *113*, 2731-2735.
66. Huang, Y.-F.; Wu, D.-Y.; Zhu, H.-P.; Zhao, L.-B.; Liu, G.-K.; Ren, B.; Tian, Z.-Q., Surface-Enhanced Raman Spectroscopic Study of P-Aminothiophenol. *Phys. Chem. Chem. Phys.* **2012**, *14*, 8485-8497.
67. Lombardi, J. R.; Birke, R. L.; Sanchez, L. A.; Bernard, I.; Sun, S. C., The Effect of Molecular Structure on Voltage Induced Shifts of Charge Transfer Excitation in Surface Enhanced Raman Scattering. *Chem. Phys. Lett.* **1984**, *104*, 240-247.
68. Furtak, T. E.; Macomber, S. H., Voltage-Induced Shifting of Charge-Transfer Excitations and Their Role in Surface-Enhanced Raman Scattering. *Chem. Phys. Lett.* **1983**, *95*, 328-332.
69. Osawa, M.; Matsuda, N.; Yoshii, K.; Uchida, I., Charge Transfer Resonance Raman Process in Surface-Enhanced Raman Scattering from P-Aminothiophenol Adsorbed on Silver: Herzberg-Teller Contribution. *The Journal of Physical Chemistry* **1994**, *98*, 12702-12707.

70. Yoon, J. H.; Park, J. S.; Yoon, S., Time-Dependent and Symmetry-Selective Charge-Transfer Contribution to Sers in Gold Nanoparticle Aggregates. *Langmuir* **2009**, *25*, 12475-12480.
71. Kim, K.; Shin, D.; Lee, H. B.; Shin, K. S., Surface-Enhanced Raman Scattering of 4-Aminobenzenethiol on Gold: The Concept of Threshold Energy in Charge Transfer Enhancement. *Chemical Communications* **2011**, *47*, 2020-2022.
72. Ye, J.; Hutchison, J. A.; Uji-i, H.; Hofkens, J.; Lagae, L.; Maes, G.; Borghs, G.; Van Dorpe, P., Excitation Wavelength Dependent Surface Enhanced Raman Scattering of 4-Aminothiophenol on Gold Nanorings. *Nanoscale* **2012**, *4*, 1606-1611.

CHAPTER 7 CONCLUSION AND FUTURE DIRECTIONS

7.1 Conclusion

In conclusion, this thesis presents synthesis, characterization and purification of noble metal nanoparticles encapsulated in silica shells for direct and quantitative SERS detection. The results obtained by studying the implication of nanomaterial quality control and mass transport through internally etched silica is important in future to understand how selective transport of molecule by changing solution conditions such as ionic strength, pH and polarity can be achieved to detect specific molecules in real environmental and biological samples using SERS.

Chapter 1 reviews the mechanism and implication of LSPR and SERS on molecule detection. In addition, an overview of existing SERS substrates, their application, and limitations including challenges associated with using solution-phase nanoparticles and approaches for overcoming those challenges are presented. Solution-phase nanoparticles are ideal SERS substrate because they are easy to synthesize and can be scaled up for production at small costs compared to nanostructures prepared from lithographic methods. However, solution-phase nanoparticles exhibit large surface energy which results in plasmon coupling upon the addition of analyte and limit their application in quantitative detection.

Because nanoparticle optical property has a huge implication on structure-function relationship, purification of solution-phase nanoparticles is important to improve nanoparticle homogeneity for their application in SERS. Chapter 2 presents the use of Sephacryl size exclusion chromatography in nanoparticle separation. Nanoparticle optical

property was monitored as silica coated gold nanoparticles passed through the SEC column and LSPR models were used to study effect of electromagnetic coupling and silica thickness on observed LSPR. Silica coated Au nanospheres with 27 and 54 average diameters were separated using surfactant-free SEC.

Chapter 3 examines molecular transport of 2-naphthalenethiol, benzenethiol, 4-mercaptobenzoic acid, and p-aminothiophenol molecules across silica shell as a function of solution ionic strength, pH, and polarity. SERS signals as a function of time for various solution conditions were fitted with time-dependent first order Langmuir isotherms to generate rate constants. Rate constants were compared to identify solution conditions (ionic strength, pH, and polarity) that provided highest rate constant and saturated SERS signals. The results obtained in chapter 3 indicate that all three solution parameters such as ionic strength, pH, and polarity are important for molecular transport and SERS.

In chapter 4, important implication of silica effective refractive index on 3D SERS-active volume for silver@gold nanoparticles were studied. Using nanoparticle optical parameters, internally etched nanoparticles with consistent effective silica refractive index were synthesized to study implications of silica refractive index on SERS signals and reproducibility. In addition, implications of molecular and nanoparticle concentrations on SERS signal for a fixed effective silica refractive index were studied using p-aminothiophenol.

Molecular adsorption on silver@gold core was studied using Langmuir adsorption isotherms in chapter 5. Wavelength shifts in the LSPR as 2-naphthalenethiol,

benzenethiol, 4-mercaptobenzoic acid, and p-aminothiphenol adsorbed on to the silver@gold metal surface were related to molecular tilt angles. Next, implications of molecular tilt angles and symmetry rules on SERS intensities of vibration modes were evaluated. Finally, concentration dependent SERS signals were modeled using the Langmuir adsorption model to generate equilibrium constants and the free energy associated with the molecular adsorption. These studies suggested that the SERS intensities observed for these thiolated ligands are highly sensitive to vibrational mode symmetry and their tilt angle relative to the nanoparticle surface.

Finally, chapter 6 studied the implication of nanoparticle core morphology (gold vs. silver@gold) and plasmonic properties on SERS. Optical properties of nanostructures were tuned by changing the core composition (Au vs. Ag@Au nanospheres or Au thickness on fixed Ag core). Higher SERS enhancement was observed for internally etched silica coated Ag@Au nanospheres compared to internally etched silica coated Au nanospheres because of higher plasmonic enhancement from Ag@Au core. In addition it was found that higher SERS signal are obtained for IE Ag@Au@SiO_2 nanoparticles with LSPR shifted towards Raman excitation and/or higher extinction at Raman excitation. Finally, the implication of charge transfer resonance on SERS was studies using 532, 632.8, and 785 nm Raman excitation wavelengths.

7.2 Future Directions

In closing, application of solution-phase silica encapsulated nanoparticles for direct and quantitative SERS detection will increase in the future as a result of improvements in nanoparticle quality control, rigorous refractive index modeling for effective silica refractive index, and through investigation of parameters such as ionic

strength, pH, polarity, nanoparticle concentration, and nanoparticle core morphology on SERS. Future applications for selective detection of molecules in complex biological and environmental samples require solution-phase SERS substrate to be robust in strong ionic strength, pH, and polarity while allowing mass transport of specific molecules to the metal core.

Present work suggests that surfactant-free SEC can be used to separate solution-phase nanoparticles based on size which is important for nanoparticle purification in order to achieve predictable structure-function relationship for SERS. At present, separation of Au nanoparticles through SEC columns using surfactant such as SDS and CTAB are reported; however, surfactants bind irreversibly to nanoparticles and can make surface useless for SERS applications. Silica coating maintains nanoparticle plasmonic properties during SEC and can be etched to free metal surface for SERS application; however, further work is required at improving peak symmetry, fractionation, and separation resolution of silica coated nanoparticles through surfactant-free SEC. In future surfactant-free SEC with optimized fractionation can be applied to purify nanorods, nanocubes, and nanostars with higher shape and size heterogeneity from bottom- up synthetic methods.

Silica coated nanoparticles are ideal in studying structure-function relationship associated with solution-phase nanoparticles because silica maintains nanoparticle optical stability through electrostatic and steric mechanisms; therefore, any changes in SERS signals can directly be related to molecular concentration in SERS-active volume near the metal core, molecular orientation, and/or molecular symmetry rules. This is particularly interesting because aggregation in solution-phase nanoparticles affects the ability to

directly correlate molecular concentration, orientation, and symmetry rules on SERS so that most studies are done on nanoparticle substrates. In addition effective refractive index of internally etched silica encapsulated nanoparticles can by rigorously monitored using refractive index modeling to achieve consistent SERS which is lacking for solution-phase nanoparticles at the moment. The ability to perform direct and quantitative SERS detection using cost effective and easy to synthesize solution phase nanoparticles will be a great asset to biomedical and environmental research as well as industrial applications where reproducible and reliable SERS assays are required. For example, solution-phase nanoparticles with plasmonic feature in visible – nearIR encapsulated within porous silica shell could be used as contrast agents to give *in vivo* information about targeted tissue without nanoparticles undergoing aggregation at harsh biological environment.

In addition, selective transport of molecules through silica shell could be achieved by changing solution parameters such as ionic strength, pH, and polarity that influence molecular transport and kinetic rate constant. Changing these solution parameters will allow variation in transport rates so that selective molecular transport is favored-an important requirement for direct detection and quantification of targeted molecule in biological and environmental samples with minimum or no need for sample preparation/purification step. Direct detection is possible using SERS that allow molecular identification using unique vibrational modes while porous silica act as a molecular sieve allowing transport of molecules that are smaller than the silica pore size; thereby, reducing most of the biological and environmental matrix effect.

Moreover, chromatographic decision trees used in analytical separations for optimizing separation parameters can be used to select solution parameters such as ionic

strength, pH, and polarity that to promotes selective transport of a targeted molecule through porous silica shells. Study of these solution parameters in molecular transport of similar molecules such as 2-naphthalenethiol, benzenethiol, 4-mercaptobenzoic acid, and p-aminothiophenol but different functional group or size is done in this work. The initial study revealed that molecular transport and rate constants depended on molecular charge, interaction with silica, partitioning, and possibly di-thiol formation; however, rigorous guided investigations using chromatographic decision tree to carefully select solution parameters that will allow selective molecular transport is required in further work. Particularly, designing experimental conditions to differentiate contributions of electrostatic interactions, partitioning, and/or di-thiol formation on transport mechanism for the above molecules is important. These studies will lay a foundation for application of internally etched silica coated nanoparticles for selective molecular detection in real samples with minimum or no preparation/purification in the near future.

In addition the current study is limited to understanding molecule-specific adsorption on Ag@Au core. Information about the molecular orientation, symmetry rules and Gibbs free energy of adsorption obtained using internally etched silica coated Ag@Au nanoparticles can easily be applied to study other molecular adsorption including drug and drug metabolites. Because SERS vibrational mode intensities for any molecule depends on molecular symmetry and orientation, understanding SERS spectral changes associated with metal-molecule interactions are important for developing quantitative and reproducible SERS analysis.

One of the limitations in using internally etched silica coated Ag@Au nanoparticles is the modest SERS signals associated with electromagnetically isolated

Ag@Au core by porous silica. Contribution of both chemical and electromagnetic enhancement with optically isolated metal core is smaller compared to solution-phase nanoparticles that are allowed to electromagnetically couple for hot spots. Because quantitative and reproducible SERS analysis is the primary application of internally etched silica coated nanoparticles; one of the method that can be used to increase SERS signals is to change the metal core. It is expected that using asymmetric core structures such as nanorods and nanostars as an alternative will greatly increase SERS because of higher electromagnetic field enhancements associated with these asymmetric metal cores so that SERS limit of detection can be improved for trace analysis which at present is possible using substrate or aggregated nanostructures.

With these applications in mind, attempts will be made in the future to incorporate silica coated solution-phase nanoparticles as chromatographic SERS-active substrates that could be used for direct and multiplexed detection of drugs, disease biomarkers, and pollutants in complex biological and environmental matrices such as blood, saliva, soil, and ground water. Use of silica encapsulated nanoparticles packed in thin capillary tubes with automated flow-through devices is expected to decrease required sample volume, allow real-time multiplex detection using SERS, increase substrate reusability, and minimize labor for reproducible and cost-effective detection and quantification using SERS detection platforms.